ANALYSIS OF FLEXURE PIVOT TILTING PAD GAS BEARINGS WITH DIFFERENT DAMPER CONFIGURATIONS

A Thesis

by

AARON MICHAEL RIMPEL

Submitted to the Office of Graduate Studies of
Texas A&M University
in partial fulfillment of the requirements for the degree of

MASTER OF SCIENCE

August 2008

Major Subject: Mechanical Engineering

ANALYSIS OF FLEXURE PIVOT TILTING PAD GAS BEARINGS WITH DIFFERENT DAMPER CONFIGURATIONS

A Thesis

by

AARON MICHAEL RIMPEL

Submitted to the Office of Graduate Studies of
Texas A&M University
in partial fulfillment of the requirements for the degree of

MASTER OF SCIENCE

Approved by:

Chair of Committee,	Daejong Kim
Committee Members,	Alan Palazzolo
	Hae-Kwon Jeong
Head of Department,	Dennis O'Neal

August 2008

Major Subject: Mechanical Engineering

ABSTRACT

Analysis of Flexure Pivot Tilting Pad Gas Bearings with Different Damper Configurations. (August 2008)

Aaron Michael Rimpel, B.S., Western Michigan University

Chair of Advisory Committee: Dr. Daejong Kim

Hydrodynamic flexure pivot tilting pad gas bearings (FPTPGBs) can enable successful operation of oil-free microturbomachinery. This work presents the experimental and analytical study of such bearings with different damper configurations. A test rig was constructed that could safely operate a ~28.6 mm, 0.8 kg rotor beyond 120 krpm. A time domain orbit simulation, which integrates nonlinear equations of motion for the rotor-bearing elements, was implemented as the primary analysis tool to predict rotor-bearing responses to imbalance, the presence and location of critical speeds, etc. Complementary analyses were also performed with a model that uses linear bearing impedance coefficients to predict system natural frequencies.

Imbalance response testing verified that the rotor-bearing system behaved linearly in the region above the critical speed, and orbit simulations predicted the response to a calibrated imbalance with notable agreement. Viscoelastic dampers added behind the FPTPGB pads delayed the onset of subsynchronous vibrations (from 43 krpm without damper to above 50 krpm with damper) of the system with bearing clearance increased by shims. Midrange subsynchronous vibrations initiated at ~20 krpm were

eventually suppressed by ~25 krpm due to the stabilizing effect of rotor centrifugal growth. The viscoelastic dampers had a negligible effect on suppressing these midrange subsynchronous vibrations in experiments, but this was not demonstrated in simulations, presumably due to much lower stiffness contribution of the damper at lower frequencies. The ideal, perfectly aligned models in the simulations were able to tolerate shims up to only 10% of nominal clearance, but the test rig exhibited surprising stability with shims as much as 200% of nominal clearance; this increase may be caused by imposed eccentricities due to misalignments in the test rig.

FPTPGBs supported by compliant bump foils can have the ability to tolerate rotor misalignments and shock loading like foil gas bearings. Simulation studies on imbalance response characteristics for several bearing shell mass and support stiffness configurations present initial design guidelines for the application. Namely, results showed that FPTPGBs favored large bearing shell mass and large support stiffness, while FPTPGBs with radial compliance favored small bearing shell mass with large support stiffness.

DEDICATION

To my family

ACKNOWLEDGEMENTS

I sincerely thank my committee chair, Dr. Daejong Kim, for his confidence and support throughout the course of this research, and certainly for his patience and concern. I would also like to thank Dr. Alan Palazzolo and Dr. Hae-Kwon Jeong for serving as committee members. I thank my colleagues at the Texas A&M University (TAMU) Turbomachinery Laboratory, Manish Kumar, Jared Goldsmith, and Andron Creary, whose friendship, camaraderie, and peer council were much appreciated. Thanks also goes to Mr. Eddy Denk for his advice and technical support during the construction of my test rig. I would like to acknowledge the financial support provided to me by the TAMU Department of Mechanical Engineering, the Texas Engineering Experiment Station, and by the TAMU Turbomachinery Research Consortium.

I would like to thank the members at Beautiful Savior Lutheran Church, College Station, TX, for their friendship; I would like to especially thank Pastor Caleb Schoeneck and his family for being like a family to me and a great blessing in my life. Finally, all I have accomplished could not have happened except for the grace of God, and for the never-ending support and love of my family. All those who have supported me and the pursuit of my goals cannot be thanked enough.

NOMENCLATURE

Symbol	
c_{BS}, c_{δ}	Viscous damping coefficients for bearing shell support and damper behind pads
C	Nominal bearing clearance
C_{SB}	Set bore clearance
d	Vertical spacing between upper and lower bearing halves, i.e. shim thickness
D	Journal/rotor diameter ($D = 2R$)
$e_{\tilde{X}}, e_{\tilde{Y}}$	Eccentricities of rotor within bearing; absolute rotor displacement minus bearing shell displacement
E	Young's modulus
f	Linear frequency, i.e. cycles per second
$F_{\tilde{X}}, F_{\tilde{Y}}$	Bearing reaction forces on rotor due to fluid film pressure
$F_{\tilde{X},\text{ext}}, F_{\tilde{Y},\text{ext}}$	External loads on rotor
$F_{p,\text{normal}}, F_{p,\text{trans}}$	Normal and transverse forces exerted on pads due to fluid film
$F_{p,\text{hold}}$	Transverse holding force of bearing shell on pads due to rigid connection
g	Gravitational constant
h	Local fluid film thickness
H	Non-dimensional local fluid film thickness ($H = h/C$)
i	Imaginary unit ($i = \sqrt{-1}$)
i_p	Tilting moment inertia of pads

$[I]$	Identity matrix
k_{modal}	Real part of eigenvalue for rotor-bearing system linear model
k_{BS}, k_{δ}	Stiffness coefficients for bearing shell support and pad radial direction
k_{ϕ}	Stiffness coefficient for pad tilting direction
L	Length of bearing in axial direction
m_{BS}, m_R, m_p	Masses of bearing shell, rotor, and pads
M_p	Moment exerted on pad due to fluid film pressure
$[M]$	Mass matrix (defined in context)
p	Pressure
p_a	Atmospheric pressure
P	Non-dimensional pressure ($P = p / p_a$)
r_p	Preload radius
r_g	Radial growth of rotor
R	Outer radius of rotor
R_i	Inner radius of rotor
R_p	Dimensionless preload ($R_p = r_p / C$)
t	Time
u_{im}	Imbalance radius
$(\tilde{x}, \tilde{y})$	Displacements in mathematical model coordinates
$(\tilde{X}, \tilde{Y}, \tilde{Z})$	Orthogonal coordinate axes in mathematical model

(X, Y, Z)	Orthogonal coordinate axes in experimental test rig
z	Axial coordinate in bearing or impedance coefficient
Z	Non-dimensional axial coordinate ($Z = z / R$)
$[Z]$ or $[z]$	Impedance matrix (defined in context)

Greek:

δ	Radial pad deflection
$\varepsilon_{\tilde{X}}, \varepsilon_{\tilde{Y}}$	Non-dimensional eccentricities of rotor within bearing ($\varepsilon = e / C$)
ϕ	Pad tilting angle or phase angle (defined in context)
Φ	Scaled, non-dimensional pad tilting angle ($\Phi = R\phi / C$)
η	Structural loss coefficient
λ_K	Eigenvalue for rotor-bearing system linear model
Λ	Bearing number ($\Lambda = (6\mu\omega / p_a)(R / C)^2$)
μ	Viscosity of fluid film
ν	Poisson's ratio or excitation frequency ratio ($\nu = \Omega / \omega$)
θ	Angular coordinate
θ_p	Angular position of pad
ρ	Density
σ	Squeeze number ($\sigma = 2\Lambda$ or $\sigma = 2\Lambda\nu$, defined in context)
τ	Non-dimensional time ($\tau = \omega t$ or $\tau = \Omega t = \nu\omega t$, defined in context) or time constant of exponential rotor-speed decrement
ω	Rotor spin speed or rotational frequency (i.e. $\omega = 2\pi f$)

Ω	Excitation frequency, i.e. rotor precession frequency
ψ	Phase lag angle of response
$\{\psi_K\}$	Eigenvector for rotor-bearing system linear model
Ψ	Non-dimensional pad deflection ($\Psi = \delta / C$)
$\zeta_{X,Y}$	Orientation angles from tachometer to vibration sensors

Acronym

DAQ	Data acquisition
FFT	Fast Fourier Transform
FPTPB	Flexure pivot tilting pad bearing – oil lubricated
FPTPGB	Flexure pivot tilting pad gas bearing
FPTPGB-C	Flexure pivot tilting pad gas bearing with pad radial compliance mechanism
MTM	Microturbomachinery or microturbomachines
SFD	Squeeze film damper
TAMU	Texas A&M University
VI	Virtual instrument
WFR	Whirl frequency ratio

TABLE OF CONTENTS

Page

ABSTRACT iii

DEDICATION v

ACKNOWLEDGEMENTS vi

NOMENCLATURE vii

TABLE OF CONTENTS xi

LIST OF FIGURES xiv

LIST OF TABLES xxiii

CHAPTER I INTRODUCTION 1

CHAPTER II LITERATURE REVIEW 6

CHAPTER III RESEARCH OBJECTIVE 13

Background – Previous Work 13
Problem Description / Activities of Present Work 14

CHAPTER IV GEOMETRY, PARAMETERS, AND CONFIGURATIONS OF FLEXURE PIVOT TILTING PAD BEARINGS 17

CHAPTER V NUMERICAL MODELING METHODOLOGY 21

Orbit Simulation 21
Perturbation Method Simulation 26

CHAPTER VI EXPERIMENTAL FACILITY 32

Overview of Test Rig Layout 32
Test Bearings 36
Instrumentation and Data Acquisition 39

CHAPTER VII EXPERIMENTAL STUDIES: TEST RIG PERFORMANCE AND EFFECT OF BEHIND-PAD DAMPER ON STABILITY 41

Page

Initial Test Rig Evaluation with Setup #1 42
Description of Rotor-Bearing Failure and Refurbishments 51
Calibrated Imbalance Response Testing with Setup #2 53
Testing with Dampers Behind Pad Radial Compliance Structure with Setup #2 62
Experimental analysis 62
Simulation analysis 69
Discussion and concluding remarks 73
Closure on Experimental Studies 76

CHAPTER VIII SIMULATION STUDY OF FPTPGBs AND FPTPGB-Cs WITH A CORRUGATED BUMP FOIL SUPPORT 78

Bearings without Radial Compliance 80
Description of linear analysis method 83
Discussion on first critical speed due to rotor natural frequency 88
Discussion on higher critical speeds 90
Concluding remarks 93
Bearings with Radial Compliance 94
The Effect of Rotor Growth and Radial Compliance on Pad Preload 102
Closure on Simulation Studies 105

CHAPTER IX SUMMARY AND CONCLUSIONS 108

REFERENCES 111

APPENDIX A A MANUAL FOR THE SETUP AND OPERATION OF THE FLEXURE PIVOT TILTING PAD GAS BEARING TEST RIG 115

Bearing Setup and Alignment 115
Turbine Shroud and Thrust Bearing Alignment 117
Instrumentation Specifications 121
Data Acquisition System Connections and Settings 123
Eddy Current Proximity Probe Calibration Procedure and Results 137

APPENDIX B TEST BEARING PARAMETER IDENTIFICATION 146

Pad Radial and Tilting Stiffness Calculations 146
Estimation of Bearing Clearances 150

Page

APPENDIX C STUDY ON THE ACCURACY OF DIGITAL BANDPASS FILTERING USED TO DETERMINE SYNCHRONOUS RESPONSE 156

APPENDIX D CORRELATION OF DIFFERENT PHASE ANGLE DEFINITIONS 162

VITA 166

LIST OF FIGURES

Page

Figure I-1: Tilting pad bearing technology – different tilting pad types: (a) spherical seat and (b) rocker-types (images from [13]), (c) picture of manufactured FPTPGB-C, (d) magnified view of wire-EDM structure. 2

Figure I-2: Foil gas bearing – top foil supported by compliant bump foil accommodates rotor growth and misalignments....3

Figure I-3: Integrated flexure pivot tilting pad bearing and squeeze film damper (image from [10]). Bearing shown uses oil lubricant and requires end seals; inset image is magnification of flexure pivot pads and centering spring structure created by wire-EDM. 4

Figure I-4: FPTPGB-C supported by bump foil elastic structure. 5

Figure IV-1: General configuration of FPTPGB-C with elastic bearing shell support. 19

Figure IV-2: FPTPGB-C geometry. 20

Figure VI-1: Test rig rotor with impulse turbines. 34

Figure VI-2: Flexure pivot tilting pad gas bearing test rig – (a) bearing / sensor placement; (b) full assembly. 35

Figure VI-3: End view of turbine shroud and thrust nozzle assembly – (a) offset pressurized air inlets create circular flow for driving impulse turbines; (b) magnified view shows face of thrust nozzle with circular array of air supply orifices (4 x 0.5 mm diameter). 36

Figure VII-1: Synchronous response Bode plots for test rig Setup #1 for (a) “Front” and (b) “Rear” probe stations. Hydrodynamic stability shown above 112 krpm. 44

Page

Figure VII-2: Predicted synchronous response (filtered out subsynchronous for unstable cases) for rotor-bearing system with 700 mg-mm imbalance and nominal clearances of 31-34 microns. Results compared with major amplitude from "Rear" probe station for test rig Setup #1. 46

Figure VII-3: Cascade plot of predicted response for 33 micron nominal clearance using orbit simulation. Stability is shown through 140 krpm even though subsynchronous rotor whirl is present from 40-80 krpm. 46

Figure VII-4: Predicted synchronous and subsynchronous responses for 33 micron nominal clearance and model comparing effect of centrifugal rotor growth. Rotor centrifugal growth stabilizes subsynchronous vibrations by increasing effective preload. 47

Figure VII-5: Cascade plot for test rig Setup #1 – Response for "Rear Vertical" probe. Stability of the rotor-bearing system demonstrated beyond 112 krpm with no subsynchronous vibrations in range....49

Figure VII-6: Cascade plot for test rig Setup #1 – Response for "Rear Vertical" probe. Stability of the rotor-bearing system demonstrated beyond 120 krpm with no subsynchronous vibrations in range....50

Figure VII-7: Damaged rotor and bearing after seizure occurred while running at 120+ krpm for extended period. (a) Localized heating and micro-welding on circumference of rotor within "Front" bearing (inset shows magnified view of damaged region). (b) Undamaged rotor within "Rear" bearing. (c) Close-up of damage to "Front" bearing (arrow indicates rotor spin direction). (d) Side-by-side comparison of "Front" and "Rear" bearings to show condition after rotor-bearing system failure. 52

Figure VII-8: Rotor after polishing to repair damaged surface. (a) "Front" end of rotor with remnant of deep grooves (~ 1 mil). (b) Before and after comparison of damaged region on rotor surface. 53

Page

Figure VII-9: Synchronous response Bode plots for test rig Setup #2 for (a) "Front" and (b) "Rear" probe stations. Baseline response without added imbalance. 55

Figure VII-10: Synchronous response Bode plots for test rig Setup #2 for (a) "Front" and (b) "Rear" probe stations. In-phase imbalance of 288 mg-mm added to each end of rotor....56

Figure VII-11: Imbalance response (baseline subtracted) for 288 mg-mm imbalance applied in phase at each end of rotor. Thick lines represent predictions for nominal clearances of 31 and 32 microns....59

Figure VII-12: Response amplitudes normalized by amplitude for 288 mg-mm vs. added imbalance normalized by 288 mg-mm. Solid line represents 1:1 and dashed line represents +5%....61

Figure VII-13: Adding shims between upper and lower bearing halves to increase vertical clearance and induce instability below 60-70 krpm, and adding dampers to enhance stability.....63

Figure VII-14: Synchronous-filtered response Bode plots for test rig Setup #2 with 3 mil shim and no damper for (a) "Front" and (b) "Rear" probe stations. Subsynchronous vibrations occurred from approx. 20-25 krpm and above 43 krpm. 65

Figure VII-15: Synchronous response Bode plots for test rig Setup #2 with 3 mil shim and with added damper for (a) "Front" and (b) "Rear" probe stations. Subsynchronous vibrations occurred from approx. 21-26 krpm and above 50 krpm. 66

Figure VII-16: Cascade plot for test rig Setup #2 with 3 mil shim and no damper – Response for "Rear Vertical" probe. 67

Figure VII-17: Cascade plot for test rig Setup #2 with 3 mil shim and with damper – Response for "Rear Vertical" probe. 68

Figure VII-18: Comparison of subsynchronous responses for Setup #2 with 3 mil shim with and without damper for "Rear Vertical" probe. Damper has little effect on subsynchronous vibrations that occur at the middle of the speed ranges, but damper increases maximum operating speed by 16%. 69

Page

Figure VII-19: Predicted vertical responses for rotor-bearing system with split offset (0.25 mil) in bearing – nominal clearance 30 micron. Dampers added to suppress subsynchronous vibrations.....71

Figure VII-20: Predicted vertical responses for rotor-bearing system with split offset (0.25 mil) in bearing – nominal clearance 30 micron. Dampers added ignoring stiffness contribution.....72

Figure VII-21: Predicted vertical responses for rotor-bearing system with split offset (0.125 mil) in bearing – nominal clearance 32 micron. 72

Figure VII-22: Coast down speed vs. time for test rig Setup #2 and 3 mil shim. Filled-in symbols represent data points used for curve fit. 75

Figure VII-23: Summary of exponential time constant vs. shim thickness for coast down tests with test rig Setup #2. Increasing shim thickness linearly increases the exponential time constant due to reduced friction drag of the air film. 75

Figure VIII-1: Synchronous imbalance responses – bearings without radial compliance. Rotor response (solid line) and bearing shell response (dotted line). Fixed bearing shell support stiffness (1e7 N/m) and varying bearing shell mass (0.1, 0.2, and 0.3 kg). Inset shows zoomed region by middle critical speeds.....81

Figure VIII-2: Synchronous imbalance responses – bearings without radial compliance. Rotor response (solid line) and bearing shell response (dotted line). Fixed bearing shell mass (0.2 kg) and varying bearing shell support stiffness (0.5e7, 1e7, and 5e7 N/m). Inset shows zoomed region by middle critical speeds.....81

Figure VIII-3: Cascade plot of rotor vibrations for simulated case of bearings without radial compliance, bearing shell mass of 0.1 kg, and bearing shell support stiffness of 1e7 N/m. System excited by supersynchronous natural frequency associated with critical speed at ~100 krpm.....82

Page

Figure VIII-4: Plots of $f_K(\nu)$ vs. frequency ratio to determine zero-crossing points. Cases shown for bearing without radial compliance; 0.2 kg and 5e7 N/m bearing shell mass and support stiffness; and selected rotor speeds of (a) 10 krpm, (b) 40 krpm, (c) 70 krpm, and (d) 100 krpm. 86

Figure VIII-5: Predicted natural frequencies for bearing without radial compliance and fixed bearing support stiffness (1e7 N/m); comparisons with different bearing shell masses (0.1, 0.2, and 0.3 kg). 87

Figure VIII-6: Predicted natural frequencies for bearing without radial compliance and fixed bearing shell mass (0.2 kg); comparisons with different bearing shell masses (5e6, 1e7, and 5e7 N/m)....87

Figure VIII-7: Trends of natural frequencies for a simple 2-mass system. Mass-1 and stiffness-1 are analogous to the bearing shell mass and support stiffness. Mass-2 and stiffness-2 are analogous to the rotor mass and gas film stiffness. Analogous comparisons show effects of increasing (a) bearing shell mass, (b) bearing shell support stiffness, and (c) gas film stiffness. 89

Figure VIII-8: Effect of increasing bearing shell mass on multiple crossing points for natural frequency contours. 92

Figure VIII-9: Synchronous imbalance responses – bearings with radial compliance. Rotor response (solid line) and bearing shell response (dotted line). Fixed damper stiffness (1e7 N/m) and varying bearing shell mass (0.1, 0.2, and 0.3 kg)....96

Figure VIII-10: Synchronous imbalance responses – bearings with radial compliance. Rotor response (solid line) and bearing shell response (dotted line). Fixed bearing shell mass (0.2 kg) and varying damper stiffness (0.5e7, 1e7, and 5e7 N/m). 96

Figure VIII-11: Cascade plot of rotor vibrations for simulated case of bearings with radial compliance, bearing shell mass of 0.3 kg, and bearing shell support stiffness of 1e7 N/m. System excited by subsynchronous natural frequencies of rotor and bearing shell which are suppressed after 140 krpm. 97

Page

Figure VIII-12: Predicted natural frequencies for bearing with radial compliance and fixed bearing support stiffness (1e7 N/m); comparisons with different bearing shell masses (0.1, 0.2, and 0.3 kg). 98

Figure VIII-13: Predicted natural frequencies for bearing with radial compliance and fixed bearing shell mass (0.2 kg); comparisons with different bearing shell masses (5e6, 1e7, and 5e7 N/m)....99

Figure VIII-14: Plots of $f_K(\nu)$ vs. frequency ratio for 0.1 kg and 1e7 N/m bearing shell mass and support stiffness at 130-150 krpm. Inflection in contour causes abrupt change in the zero-crossing frequency ratio. 99

Figure VIII-15: Rotor growth increases the converging wedge effect for a bearing without radial compliance. Pad with radial compliance allows more rotor growth, but eventually leads to a loss of converging wedge. 103

Figure VIII-16: Synchronous direct stiffness coefficients for various cases of bearings described in Table VIII-1. (a) Rotor growth significantly increases direct stiffness of bearing without radial compliance. (b) Radial compliance reduces the direct stiffness of the bearing and extends maximum operating speed. 104

Figure VIII-17: Rotor growth and mean pad deflection vs. rotor speed for bearing with radial compliance described in Table VIII-1. Radial compliance allows rotor growth to exceed original set bore clearance, but mean pad deflection must be smaller than original preload radius to maintain converging wedge effect. 104

Figure VIII-18: Mean film thickness values vs. rotor speed for bearing with radial compliance described in Table VIII-1. Mean pad tilt angle increases initially to grow local film thickness at leading edge of pad, but it rotor growth causes pad angle to neutralize. Eventually film thickness reduction ratio drops to near unity, indicating loss of preload. 105

Page

Figure A-1: Rotor-bearing relative alignment – (a) rotor wrapped with shims within bearings to consume set bore clearance; (b) end view of aligned bearing at "Front" of rotor; (c) magnification of end view showing the shim between the rotor and the bearing pad. 117

Figure A-2: Turbine shroud and thrust nozzle assembly adjustments. 120

Figure A-3: Data acquisition schematic – numbers refer to Table A-1. 121

Figure A-4: Oscillator demodulator wiring schematic. 124

Figure A-5: DC regulated power supply (BK Precision Model 1627A); connection diagram for supplying -24 Vdc to oscillator demodulators. 124

Figure A-6: *LabVIEW* VI front panel. 134

Figure A-7: Flow diagram for automated data processing program. 136

Figure A-8: Proximity transducer system calibration schematic. Numbers refer to components in Figure A-3 and Table A-1. 140

Figure A-9: Proximity probe output voltage vs. probe gap (CAL-1). 143

Figure A-10: Proximity probe output voltage vs. probe gap (CAL-2). 144

Figure B-1: Tilting pad simplified degrees of freedom. Numbers indicate the respective locations of the accelerometer for measuring radial, axial pitching, and tilting motion natural frequencies. 147

Figure B-2: Normalized FFT amplitudes of accelerometer signals measuring exited modes of pad vibration for (a) lower and (b) upper pads. From highest to lowest frequency: Radial, axial pitching, and tilting motion. 148

Figure B-3: Schematic for bearing set bore measurement locations. 153

Page

Figure B-4: Measured set bore diameters (A and B) and rotor journal diameters for Setup #1 and Setup #2 (D-1 and D-2, respectively) plotted vs. axial position of bearings – (a) Bearing 1; (b) Bearing 2; (c) Bearing 3. Error bars on individual set bore measurements represent two standard deviations from measurements. Phantom lines represent final estimated set bore clearance (center line) and estimated deviation representing the level of uncertainty in the values (upper/lower lines). 155

Figure C-1: Measured amplitudes (top) and phase angles (bottom and inset) vs. synchronous frequency for multiple synchronous component amplitudes (Test 1). 158

Figure C-2: Normalized average error of amplitude and phase angle for Test 1. Percent error of amplitudes (a) is presented and compared with 5% error, and phase angle error (b) is presented and compared with a 3 degree error. Error bars in both cases represent two standard deviations of the data at a given frequency. 159

Figure C-3: Measured amplitudes (top) and phase angles (bottom) vs. synchronous frequency for multiple synchronous component phase angles (Test 2). 160

Figure C-4: Normalized average error of amplitude and phase angle for Test 2. Percent error of amplitudes (a) is presented and compared with 5% error, and phase angle error (b) is presented and compared with a 3 degree error. Error bars in both cases represent two standard deviations of the data at a given frequency. 161

Figure D-1: Different phase angle definitions – (a) phase lag of measured response from trigger signal; (b) phase lag of rotor position vector from location of imbalance. 163

Figure D-2: Orientation of keyphasor/tachometer sensor for relating phase angle definitions. 164

Page

Figure D-3: Measured phase lag angles for response lag angles of 0, 90, and 180˚. Key: solid circles represent rotor positions at peak X & Y response amplitudes, the dot on the solid circle is the location of the imbalance and keyphasor/tachometer target, and the dashed circle is rotor position when tachometer target is viewed by the keyphasor/tachometer sensor (block arrow) 164

LIST OF TABLES

Page

Table VI-1: Test rig rotor properties. 34

Table VI-2: Key to labeling in Figure VI-2. 34

Table VI-3: Summary of rotor-bearing clearance estimation based on 15 micron preload radius – measurement data and estimation of variance presented in Appendix B. Units are inches unless otherwise noted. 37

Table VI-4: Additional pad-related test bearing parameters. 38

Table VII-1: Measured amplitude and phase angle data for test rig Setup #2 with baseline imbalance. Only speeds used for baseline subtraction presented. 57

Table VII-2: Measured amplitude and phase angle data for test rig Setup #2 with 288 mg-mm added imbalance. Only speeds used for baseline subtraction presented. 58

Table VII-3: Measured amplitude and phase angle data for test rig Setup #2 at ~70 krpm for different cases of added imbalance. Amplitudes in microns and phase angles in degrees. 60

Table VII-4: Amplitude and phase angle data for baseline subtraction of data in Table VII-3. Amplitudes in microns and phase angles in degrees. Phase angles compensated for position of the vibration sensors with respect to the tachometer as explained in Appendix D. 61

Table VII-5: Properties of dampers used in orbit simulations. 71

Table VIII-1: Rotor-bearing system parameters. 79

Table A-1: Data acquisition components. 122

Table A-2: Amplifier front panel settings. 126

Table A-3: PCI board connections. 127

Page

Table A-4: Format of saved data for *TSIG_data_####.txt*.....135

Table A-5: Format of saved data for *FFT_data_####.txt.* 135

Table A-6: Calibration data for passing proximity probes (CAL-1).....141

Table A-7: Calibration data for failing proximity probes (CAL-1). 142

Table A-8: Least-squares curve fit parameters for linear regions (CAL-1). 143

Table A-9: Summary of proximity probe calibration (CAL-1).....143

Table A-10: Calibration data for passing proximity probes (CAL-2).....144

Table A-11: Least-squares curve fit parameters for linear regions (CAL-2). 145

Table A-12: Summary and comparison of proximity probe calibrations.....145

Table B-1: Calculated/measured pad radial and tilting stiffness values. 149

Table B-2: Bearing measurement data and nominal clearance estimation. Units are inches unless otherwise noted. 154

Table C-1: Prescribed components of combined test signal used for digital bandpass filtering algorithm performance evaluation. 157

Table D-1: Response lag angles (in degrees) calculated from measured phase lag angles and Equations (D-1) and (D-2). 165

CHAPTER I

INTRODUCTION

Microturbomachinery (MTM) using oil-free bearings typically have power outputs less than 1 MW, typically on the order less than 200-300 kW [1-3]. Various applications in oil-free MTM include turbochargers, turbo blowers, turbo compressors, micro-gas turbines, auxiliary power units, etc., that have uses for automotive, aerospace, and fuel cell industries, to name a few [1-4]. Oil-free lubrication is cleaner (i.e. less pollution; more environment-friendly), more efficient due to lower drag torque, and requires lower maintenance than traditional oil lubrication; however, drawbacks include smaller load capacity, low damping, and tighter manufacturing tolerances [5, 6].

One type of oil-free bearing is the tilting pad gas bearing. Tilting pad bearing technology itself has been favored for decades due to the inherent stability feature of self-adjusting pads which are allowed to follow rotor motions, resulting in low cross-coupled stiffness [7]. In fact, for negligible pad mass and inertia, and with no pivot rotational stiffness or damping, cross-coupled bearing forces become identically zero [8]. Conventional tilting pad bearings may use spherical seat or rocker-type pivots, while flexure pivots are especially suited for gas bearings (Figure I-1). Flexure pivot tilting pad gas bearings (FPTPGBs) manufactured by wire-EDM do not have assembly tolerance stack-up or pivot wear due to relative motion between separate parts [9, 10].

This thesis follows the style of ASME Journal of Tribology.

A technical challenge with oil-free MTM is the high-speed operation required to generate meaningful power and efficiency, which forces the designer to consider radial growth of the rotor due to centrifugal stresses and noticeable temperature increases from ambient conditions. The rotor centrifugal and thermal growth may be as much or larger than the bearing clearance at operating conditions [11, 12], therefore a compliant bearing structure is required to prevent clearances from being consumed. FPTPGBs with a pad radial compliance mechanism (FPTPGB-Cs), also made by wire-EDM, have been developed [10] to allow bearing pads to deflect in the radial direction (Figure I-1(d)).

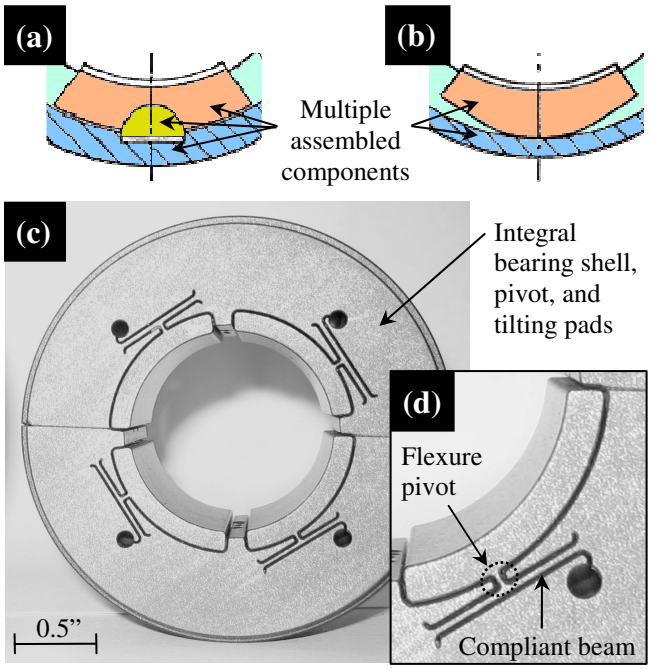

Figure I-1: **Tilting pad bearing technology – different tilting pad types: (a) spherical seat and (b) rocker-types (images from [13]), (c) picture of manufactured FPTPGB-C, (d) magnified view of wire-EDM structure.**

As mentioned above, gas lubrication is known to have low damping and requires tight tolerances for adequate pressure generation. It is presumed that the latter fact may effectively limit the usefulness of FPTPGBs and FPTPGB-Cs to only very well aligned systems with rigid rotors (i.e. operation below bending critical speeds). Foil gas bearings, another type of oil-free bearing (Figure I-2), utilize an elastic structure that supports the top foil (actual bearing surface) which may comply to rotor misalignments and also provide dry friction (Coulomb) damping to the rotor-bearing system, tolerate rotor growth, and absorb external shock loads [11, 14-21].

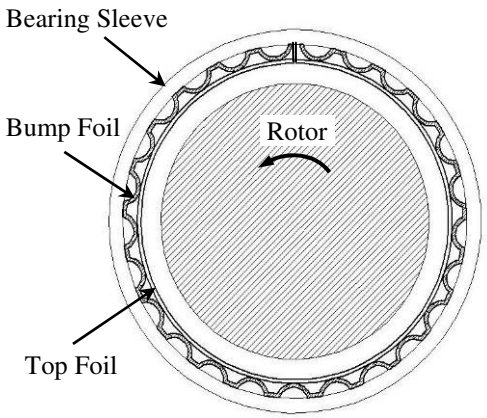

Figure I-2: **Foil gas bearing – top foil supported by compliant bump foil accommodates rotor growth and misalignments.**

Another technology, squeeze film dampers (SFD) for oil lubricated and rolling-element lubricated systems, is well-established and has been used as frequently as a retro-fit stabilizing mechanism for unstable machinery. SFDs have also been used as a means to add damping to systems with negligible inherent damping in order to reduce vibration response amplitudes and increase the ability to handle large imbalances (e.g.

blade loss in a jet engine) [7]. Essentially, a bearing is supported mechanically by an elastic structure (e.g. centering springs and O-rings), and motions of the bearing are damped by squeezing a fluid film that exists around the bearing. A recent form of this technology is the integral SFD, which is a single structure that incorporates both the bearing and the centering spring (Figure I-3).

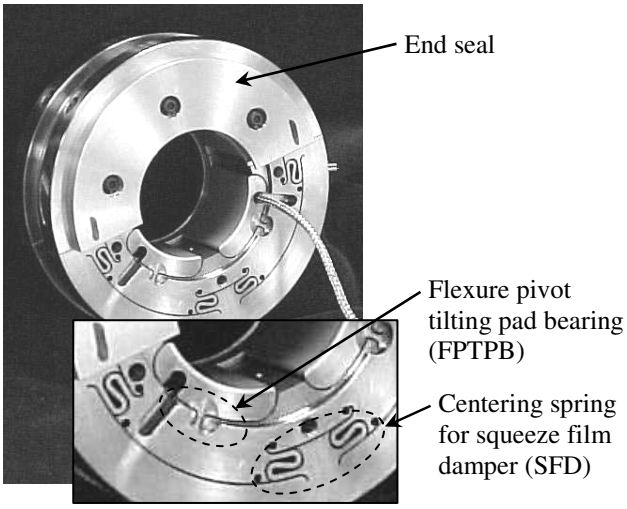

Figure I-3: **Integrated flexure pivot tilting pad bearing and squeeze film damper (image from [10]). Bearing shown uses oil lubricant and requires end seals; inset image is magnification of flexure pivot pads and centering spring structure created by wire-EDM.**

An application of FPTPGBs and FPTPGB-Cs that, to the author's knowledge, has not been investigated incorporates the idea of both foil gas bearings and SFDs as shown in Figure I-4. Here, a FPTPGB-C is supported by a bump foil in a manner that resembles a centering spring of a SFD. No oil exists in the gap between the bearing shell and the rigid structure to perform like a traditional SFD; however, like a foil gas bearing, the bump foil may provide damping in the form of dry friction. This setup

could incorporate the positive features of tilting pad gas bearings and foil gas bearings, including high stability due to low cross-coupled stiffness, tolerance to rotor misalignments, improved ability to absorb external shock loads, and the ability to increase system damping.

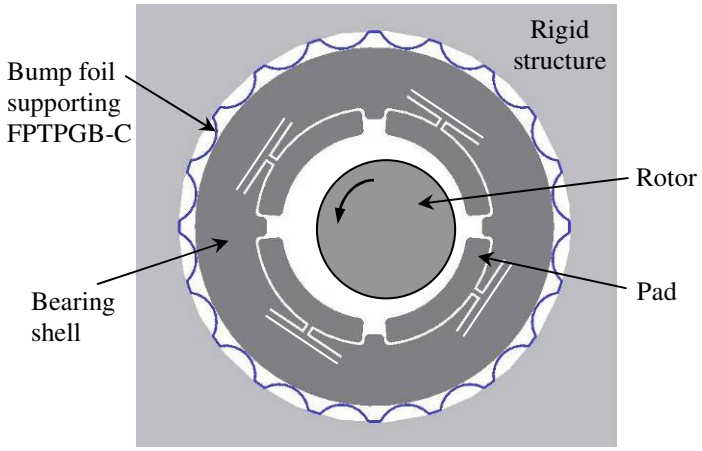

Figure I-4: FPTPGB-C supported by bump foil elastic structure.

CHAPTER II

LITERATURE REVIEW

This chapter presents a survey of technical papers that served as bases for understanding gas bearing technology, specifically the characteristics of tilting pad gas bearings, and analysis methodologies. A major portion of the study in this thesis is based on a continuation of the analysis tools developed by Sim and Kim [5, 22], hence a large focus was made on the findings of these works. Other sources are also included for their insight related to rotordynamic phenomena and physical characteristics associated with some types of bearing configurations (e.g. squeeze film dampers and foil gas bearings). The following sources are presented in a topical order.

Sim and Kim [5] carried out parametric design studies for flexure pivot tilting pad gas bearings with a pad radial compliance mechanism (FPTPGB-Cs). Their work identified the characteristics of several key parameters, including pad radial and tilting stiffnesses, nominal clearance, pivot offset, and preload. The study was theoretical, utilizing time domain, "brute force" integration of rotor and bearing pad equations of motion under isothermal conditions. The rotor model consisted of a hollow rotor, which was allowed to experience centrifugal growth proportional to the square of the spin speed as predicted by plane stress and finite element models. Cylindrical, rigid-mode vibrations of the rotor were considered, such that only rotor translational motions were simulated. Each bearing pad model consisted of the pad itself (mass and tilting moment of inertia properties), connected to ground by a radial stiffness element and a rotational

stiffness element. Radial compliance of the bearing pads was presented as a means that could permit higher speed operation by allowing the bearing set bore circle to expand as the rotor experiences centrifugal growth. Main conclusions presented in this paper are as follows: (1) Maximum operating speed is dependent on minimum gas film thickness, which is a function of the nominal clearance, amount of rotor growth, and pad radial stiffness. (2) Larger nominal clearance and smaller pad radial stiffness are better able to accommodate rotor growth; however, the decreased bearing stiffness eventually causes instability at low speeds. Nevertheless, rotor centrifugal growth was shown to be a stabilizing mechanism in these cases, stiffening the bearing with increasing speed. (3) Larger preload and pivot offset increased critical speed and onset speed of instability due to increased hydrodynamic wedge effect. (4) Pad tilting motion has finite stiffness due to flexure pivot mechanism. Pad tilting stiffness was demonstrated to have little effect on direct stiffness (i.e. negligible effect on critical speed), but it was shown to have a significant effect on cross-coupled stiffness (i.e. contributes to destabilization of bearing). Moreover, decreasing pad tilting stiffness correlated linearly with an increase of onset speed of instability and reduction of whirl frequency ratio (WFR).

Although nonlinear behavior of rotor-bearing systems may be captured by time domain analyses, often this method is undesirable due to large computational time demands. Frequently, rotordynamic calculations are carried out by representing bearings (and other elements, such as seals, etc.) as springs and dashpots (i.e. with stiffness and viscous damping properties). Finding perturbation solutions of the Reynolds equation, the governing nonlinear differential equation for the fluid film lubricant of a bearing, is a

method that is used to calculate the bearing force coefficients. Nicholas [23] credits Lund [8] with using the perturbation technique to provide "the first major published document that contained tilting pad journal bearing stiffness and damping coefficients." As summarized by Nicholas, "Lund's pad assembly method" is the concept of determining the dynamic force coefficients of individual pads for a given rotor eccentricity, then summing the contributions of all pads to obtain the dynamic force characteristics of the entire bearing. In his work, Lund notes that "[cross-coupled stiffness and damping terms] vanish when pad inertia is neglected," and Nicholas identifies this as the first time that this fact was reported. Lund [24] also presents the calculation of stiffness and damping coefficients for gas tilting pad bearings and a method of linear stability analysis by which comparison of a critical rotor mass (calculated from a zero-effective damping condition) is compared to the actual rotor mass at given operating conditions. Instability is defined when actual rotor mass exceeds critical rotor mass.

Delgado et al. [25] predict dynamic force coefficients for shoed brush seals, wherein the model for an individual shoe is identical to that of a tilting pad with three degrees of freedom (tilting, radial, and transverse motions) and a pivot offset of 50%. Delgado et al. present a detailed formulation of the perturbation technique, including a convenient relation between the pressure gradients with respect to shoe motions and the pressure gradients with respect to rotor motions. In this manner, zeroth-order solutions of Reynolds equation are solved, followed by first-order solutions for the pressure gradients with respect to the rotor motions, then first-order solutions for the pressure

gradients with respect to the shoe motions are computed from the relation without needing to be solved directly.

Sim and Kim [22] advanced their previous insight [5] on the characteristics of FPTPGB-Cs (and rotor experiencing centrifugal growth) by analyzing predicted dynamic force coefficients and performing linear stability analyses. Formulations of the perturbation equations (zeroth- and first-order forms of Reynolds equation) are presented, referencing [25] due to the similarity of the tilting pad model to the shoed brush seal. Computation of synchronous force coefficients were performed, and the following conclusions were noted: (1) Virtually isotropic bearing characteristics were observed, especially at higher speeds when dimensionless rotor eccentricity was less than 0.05. Only at low speeds, when eccentricities are relatively large, did slight anisotropic behavior become noticeable. (2) Direct stiffness showed a near-linear increase with speed, while direct damping showed a sharp decrease (not-quite exponential) with speed. (3) Cross-coupled stiffness and damping coefficients become zero when rotor speed is at the tilting natural frequency of the pads, where pad motions are virtually in-phase with rotor motions. (4) Direct stiffness and damping were shown to become zero when rotor speed is at the radial natural frequency of the pads. In the case of this study, the pad radial natural frequency was over four times larger than the pad tilting natural frequency, and it was required to neglect rotor centrifugal growth (to allow higher simulation of rotor speeds without consuming bearing clearance) to show this point. (5) Stability analyses referencing Lund's approach [24] showed that the bearings being studied would be stable up to the limit set by rotor centrifugal growth.

Recently, Kim [26] and Kim et al. [27] looked at comparisons of natural frequencies from time domain analysis simulations to the natural frequencies computed by a method using frequency-dependent bearing impedance coefficients. Both references follow Lund's analysis for evaluating a threshold speed of instability [24], but Kim et al. [27] conclude that the method is not dependable for this purpose since threshold speeds of instability were far less than predicted in time domain simulations; however, the method was found to predict comparable natural frequencies. Kim et al. [27] also presents an alternative method for calculating natural frequencies from bearing impedance coefficients that gives reasonable results with time domain simulations.

Zhu and San Andrés [28] present studies on hybrid FPTPGBs. Hybrid operation refers to the ability of the gas bearing to operate under hydrodynamic and/or hydrostatic fluid pressure generation. The test rotor-bearing system in this study showed instability at approximately 81 krpm when operating in pure hydrodynamic mode, and the addition of hydrostatic pressure stabilized the system beyond 99 krpm, the speed limit of the driving motor. Increasing hydrostatic feed pressure was shown to increase direct stiffness coefficients and first rigid-mode critical speed while decreasing viscous damping ratio. Predictions of direct stiffness coefficients were favorable to test results; however, predictions of direct damping coefficients were approximately 100% larger than measured.

San Andrés [6] furthered the work of ref. [28] by presenting additional experimental results and predictive model validation of force coefficients, mass flow rate of hydrostatic supply orifice, and drag torque. San Andrés reports that the current

hydrodynamic bearing model is better than used previously [28]; however, there were still large discrepancies with the predictions of direct damping. Nonetheless, overall trends of direct stiffness and damping versus hydrostatic supply pressure were reported to correlate well with predictions. The hydrostatic supply orifice model showed agreeable mass flow rate vs. supply pressure behavior with experiments, and the drag torque model of the bearings overestimated coast-down time constants by approximately 50% since motor drag was not considered.

San Andrés and De Santiago [29] measure imbalance responses of a rotor supported on oil lubricated flexure pivot tilting pad bearings (FPTPBs) in series with integral squeeze film dampers (SFDs). This paper compared the performance of the rotor-bearing system with and without the SFDs activated. The benefits of SFDs are reported as increased tolerance to imbalance (demonstrated FPTPB-SFD system able to tolerate twice the imbalance level of FPTPB-only system), reduced transmitted forces to ground, and relocation of critical speeds. From the experimental an analytical results, the maximum test speed was 9,000 rpm (stable), and the FPTPB-only system had a critical speed at 5,750 rpm (vertical direction). Adding the SFD resulted in a 1^{st} critical speed (rigid rotor cylindrical mode) at ~3,000 rpm due to reduced support stiffness, but also 2^{nd} critical speeds at ~4,500 rpm (vertical direction, same vibration amplitude as 1^{st} critical speed) and ~7,000 rpm (horizontal direction, smaller than 1^{st} critical speed). The 2^{nd} critical speeds were explained as "resonance of the bearing pedestals." Although relocation of system critical speeds was noted as a benefit of incorporating SFDs, there

were no comments on how relocation of the rotor's critical speed at the expense of adding additional bearing support resonances should be considered in the design.

Rotordynamic performance of foil bearings is not of particular interest in this thesis; however, general characteristics of the structural support mechanism for such bearings were reviewed. Numerous works on foil bearings [11, 14-20] emphasize the usefulness of the elastic foil-support structure to provide damping to the rotor-bearing system by a dry friction mechanism (Coulomb-type damping). Heshmat and Ku [15], Salehi et al. [16], and Rubio and San Andrés [18, 19] do experimental and analytical studies to quantify structural stiffness, friction coefficients, and equivalent viscous damping for bump-type foil bearings. Song and Kim [20] also do experimental studies to identify frequency-dependent viscous damping and structural loss factor values for foil bearings using side-loaded coil compression springs as elastic supports. Because the geometry of the top foil support structure can be relatively simple, designers have the ability to control the stiffness and damping characteristics by modifying certain parameters (e.g. bump foil thickness, bump radius, height, pitch, etc.). Furthermore, compliance of the foil bearing support structure has been noted to accommodate rotor misalignments [11, 15] and shock loading [17, 21].

CHAPTER III

RESEARCH OBJECTIVE

Previous work on flexure pivot tilting pad gas bearings (FPTPGBs) for microturbomachinery are advanced in the present work. First, FPTPGBs with radial compliance (FPTPGB-Cs) have beam structures behind the tilting pads that allow pads to deflect in the radial direction (Figure I-1(d)). The structure lends itself to be damped, if necessary, by means of placing a damping material behind the beam. Adding dampers to the system has the potential to dampen pad and rotor vibrations and is investigated. Second, there is an interest to study the effects of flexible bearing supports applied to FPTPGBs and FPTPGB-Cs (Figure I-4) with the presumed benefits of increasing tolerance to misalignments, soften the effects of shock loading, etc.

Background – Previous Work

Contributions by a former research assistant under the author's advisory committee chair include development of computer simulation codes for calculating transient rotor-bearing system responses to imbalance and calculating frequency-dependent stiffness and damping coefficients for FPTPGB-Cs, designing and procuring test bearings, and constructing a test rig. Operation of the test rig proved to be challenging due to difficult alignment of the impulse turbine drive system, and a poor thrust bearing design that resulted in severe air hammering at most operating speeds. For safety, and to prevent possible bearing and/or rotor damage, maximum test speeds

were limited to ~60 krpm, well below the designed operating limit of over 120 krpm. A vibration monitoring and data acquisition system was developed (using *LabVIEW* [30]) and was capable of generating waterfall plots [31][1]; however, a significant amount of manual post-processing was necessary to extract the data, which was tedious and time consuming.

Problem Description / Activities of Present Work

The activities for the present work include both theoretical and experimental studies. First, formulations for the FPTPGB damper configurations are developed and implemented to the existing simulation codes. This involves implementing a damper model for the pads' motions in the radial direction relative to the bearing shell and including the addition of degrees of freedom for the bearing shell translational motion. The flexible bearing shell support model reflects the realistic properties found for foil gas bearings, which is a structural stiffness/damping model [18-20]. The rotor-bearing model maintains the previous assumptions [5, 22] of isothermal operation and cylindrical mode rigid rotor vibrations – the latter assumption is justified from preliminary experiments which displayed the tendency to exhibit forward-cylindrical rotor precession. The new capability of being able to simulate the effects of a flexible bearing support include a parameter study – the focus on preliminary design aspects, considering the effects of bearing shell mass and support stiffness on the rotordynamic performance of the system.

---

[1] Often, terms "waterfall plot" and "cascade plot" are used interchangeably; however, the reference makes the following distinction: A waterfall plot graphs FFT spectrum *vs. time*, while a cascade plot graphs FFT spectrum *vs. rotor speed*.

Second, extensive refurbishments are performed on the current test rig in order to be able to run at high speeds (above 120 krpm) with reliable setup and adjustability features. A new thrust bearing system is designed and built that is stable at all operating speeds. The refurbishments also include the design and manufacture of a new test rotor with a new turbine drive system.

Finally, a new data acquisition system is created with capabilities required to fully comprehend the experimental tests. A commercial rotordynamics data acquisition system available in the laboratory (ADRE 208 Data Acquisition Interface Unit [32]) could not fully meet the testing requirements since it is limited to 60 krpm maximum rotor speeds, therefore, a new data acquisition system is developed using *LabVIEW*, which is able to meet the needs of the present tests. The new data acquisition system is practical and capable of handling synchronous rotor speeds above 120 krpm (also 3X and higher supersynchronous vibration components) and has simple data processing that can generate useful rotordynamic analysis plots (e.g. Bode plots and cascade plots). Experimental results for the working test rig are analyzed, and the effect of behind-pad dampers are studied.

Summary of activities in present work:

1. Further development of bearing simulation codes and analytical studies.
    a. Damper model behind pads and new dynamics model that includes degrees of freedom for flexible bearing shell supports.
    b. Study of flexible bearing shell supports with FPTPGBs and FPTPGB-Cs; applications on preliminary design focused on effect of bearing shell mass and bearing shell support stiffness on rotordynamic performance.
2. Redesign and modification of the existing FPTPGB test rig for improved reliability, safe operation, and high speed capability (120+ krpm).
    a. New thrust bearing system.
    b. New rotor and turbine drive system.
3. Development and implementation of a practical data acquisition system.
    a. Capable of handling synchronous rotor speeds above 120 krpm and vibration components beyond 360 krpm (6 kHz).
    b. Simple data processing that can generate Bode plots and cascade plots.
4. Experimental studies and comparisons with predictions: imbalance response testing; study of behind-pad dampers to improve stability (i.e. delay onset speed of instability) of an unstable system.

CHAPTER IV

GEOMETRY, PARAMETERS, AND CONFIGURATIONS OF FLEXURE PIVOT TILTING PAD BEARINGS

Figure IV-1 shows a general rotor-bearing system with flexure pivot tilting pad bearings having radial compliance (FPTPGB-C) and an elastically supported bearing shell. The inertial frame is indicated by $(\tilde{X},\tilde{Y},\tilde{Z})$, where $\tilde{X}$ is in the direction of gravity loading, and $\tilde{Z}$ is parallel to the rotor rotation vector. Pad motions relative to the bearing shell are given by tilting ϕ and radial δ coordinates (see Figure IV-2). The coordinates of the rotor and bearing shell relative to the inertial reference frame are given by $(\tilde{x}_R, \tilde{y}_R)$ and $(\tilde{x}_{BS}, \tilde{y}_{BS})$, respectively. Bearing shell rotational stiffness is considered to be large enough to assume negligible bearing shell rotation – thus, angular positions of the pads with respect to the inertial frame are constant. The masses of the rotor, bearing shell, and pads are denoted m_R, m_{BS}, and m_p; pads also have tilting mass moment of inertia i_p. Pad tilting stiffness is k_ϕ, and pad radial compliance is characterized by radial stiffness k_δ and damping c_δ. Stiffness and damping for the elastic bearing shell support are denoted k_{BS} and c_{BS}.

Figure IV-2 shows the schematic of a general FPTPGB-C. Eccentricities of the rotor from the bearing shell center are $e_{\tilde{X}} = \tilde{x}_R - \tilde{x}_{BS}$ and $e_{\tilde{Y}} = \tilde{y}_R - \tilde{y}_{BS}$. The eccentricities of the pad centers from the bearing center are denoted by the preload

radius r_p. Physically, preload is associated with the hydrodynamic wedge effect (or converging wedge) created by the reduction in fluid film thickness as it flows from the leading edge of the pads towards minimum film thickness. The radial distance between the set bore (maximum circle inscribed by un-deflected pads) and the surface of a centered rotor is the set bore clearance C_{SB}. The nominal bearing clearance C is considered as the theoretical clearance of a centered rotor at $\pm 90^o$ from the pad pivot (i.e. location of minimum clearance); physically this may also be represented as the sum of the preload radius and the set bore clearance, i.e. $C = C_{SB} + r_p$. The angle to the pad pivots is θ_p, and pivot offset is the ratio of the angle of the pivot from the pad leading edge to the total pad angle. The value of pivot offset for FPTPGBs is typically greater than 0.5 [5, 6, 22] as illustrated in Figure IV-1 and Figure IV-2. Pivot offset greater than 0.5 results in greater stability due to larger wedge effect which stiffens the bearing [5].

For this configuration, the local film thickness may be stated as

$$h = C + e_{\tilde{X}} \cos\theta + e_{\tilde{Y}} \sin\theta - r_g - \left(r_p - \delta\right)\cos\left(\theta - \theta_p\right) - R\phi \sin\left(\theta - \theta_p\right), \qquad \text{(IV-1)}$$

where R is the radius of the rotor and r_g is the radial growth of the rotor. Significant rotor growth may be attributed to both centrifugal and thermal effects from high speed operation, especially in gas bearing systems [5, 11, 12]; however, the present model ignores thermal growth (e.g. assume adequate cooling of the system prevents significant temperature increase). The rotor centrifugal growth may be expressed by

$$r_g = \frac{R\rho\omega^2}{4E}\left[R_i^2(\nu+3)+R^2(\nu+2)(\nu-1)\right] \qquad \text{(IV-2)}$$

for given material density ρ, Young's modulus E, and Poisson's ratio ν. R_i is the inner radius of a hollow rotor. Equation (IV-2) is derived for a simplified plane stress elastic model [5, 12, 22, 33]; however, it also agrees very well with finite element results [5]. Note the significance of the hollow rotor effect on centrifugal growth – for example, a hollow, stainless steel rotor (typical $\nu = 0.27$) with $R_i \approx 0.7R$ has twice the radial growth of a solid rotor.

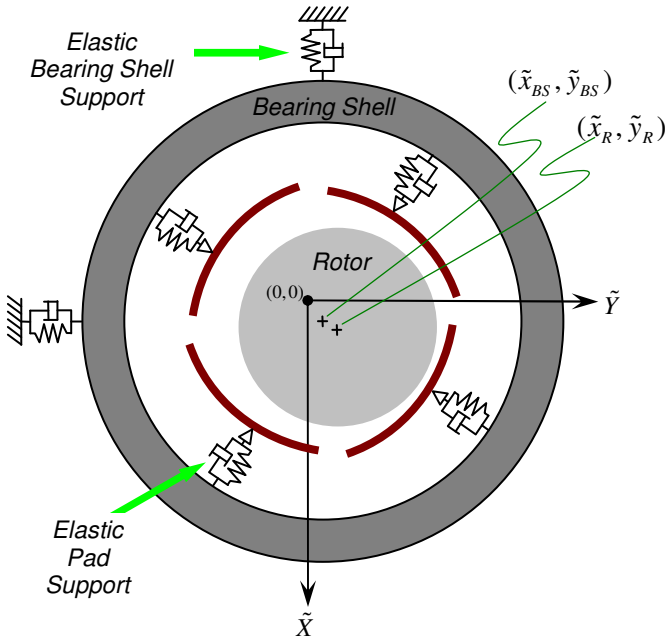

Figure IV-1: General configuration of FPTPGB-C with elastic bearing shell support.

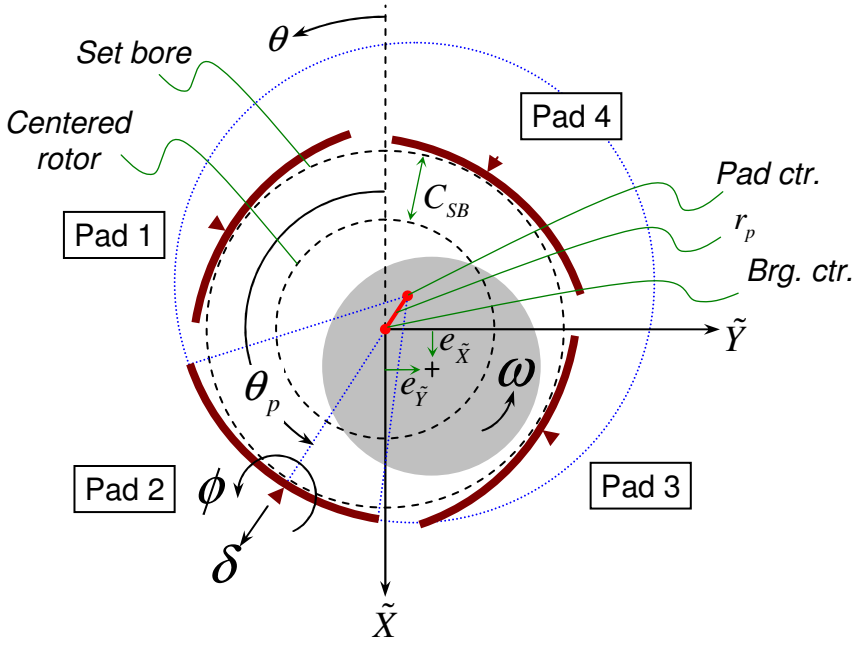

Figure IV-2: FPTPGB-C geometry.

CHAPTER V

NUMERICAL MODELING METHODOLOGY

The main analysis tool used in this work is a time-domain orbit simulation code that solves for time-space dependent pressure distributions for the gas film in the bearing and integrates equations of motion for the rotor, pads, and bearing shell. The governing equation that is used to obtain pressures is the Reynolds equation for a compressible fluid. Since the orbit simulation method solves the nonlinear governing equations in the time domain, it is able to capture nonlinear phenomena that occur in a rotor-bearing system, namely limit cycle behavior displayed by non-synchronous rotor vibration. A secondary analysis tool that is used is a perturbation method which solves first-order linearized forms of the Reynolds equation that give frequency-dependent bearing impedance coefficients. Bearing impedance coefficients may be used in subsequent rotordynamic analyses to predict natural frequencies, etc. This chapter continues to describe the details of the two numerical modeling methodologies.

Orbit Simulation

In the orbit simulation, transient motion of the pads, bearing shell, and rotor are predicted by numerical integration of equations of motion in the time domain. Forces and moments on the pads and rotor are found by solving for the hydrodynamic pressure distributions of the thin fluid film using the transient Reynolds equation given by

$$\frac{\partial}{\partial\theta}\left(PH^3\frac{\partial P}{\partial\theta}\right)+\frac{\partial}{\partial Z}\left(PH^3\frac{\partial P}{\partial Z}\right)=\Lambda\frac{\partial}{\partial\theta}(PH)+\sigma\frac{\partial}{\partial\tau}(PH), \qquad \text{(V-1)}$$

with bearing number $\Lambda=(6\mu\omega/p_a)(R/C)^2$ and squeeze number $\sigma=2\Lambda$. This form of the Reynolds equation [34] assumes hydrodynamic pressure is constant in the cross-film direction and only varies in the circumferential (θ) and axial (Z) directions, and it assumes isothermal conditions (i.e. temperature and viscosity are constant throughout the film). Also note that Equation (V-1) is non-dimensional, utilizing absolute pressure normalized by atmospheric pressure ($P=p/p_a$), film thickness of Equation (IV-1) normalized by nominal clearance ($H=h/C$), axial coordinate normalized by rotor radius ($Z=z/R$), and time normalized by rotor speed ($\tau=\omega t$). The same central difference method with power-law scheme using Gauss-Seidel iteration used in [5, 35] is employed to solve for non-dimensional pressure. Assuming pure cylindrical-mode rotor vibrations permits a half-pad solution for the pressures due to axial symmetry. A grid size of 13×8 (for θ- and Z-directions, respectively) was used for each half-pad, which was reported to give accurate results for a similar type of bearing configuration in [5].

Recall that the coordinate system in Figure IV-1 and Figure IV-2 is denoted by $(\tilde{X},\tilde{Y})$, where the $\tilde{X}$-direction is the implied direction of the rotor weight. Note that the over-tilde accented notation differs from the unaccented notation which considers $X=$ horizontal and $Y=$ vertical on the test rig (described later in Chapter VI), i.e. $\tilde{X}=-Y$ and $\tilde{Y}=X$ where $\tilde{Z}=Z$. All of the formulations for the numerical models consider the

over-tilde accented notation shown in the descriptions in Chapter IV, thus equations of motion for the rotor are

$$m_R \begin{Bmatrix} \ddot{\tilde{x}}_R \\ \ddot{\tilde{y}}_R \end{Bmatrix} = m_R u_{im} \omega^2 \begin{Bmatrix} \cos \omega t \\ \sin \omega t \end{Bmatrix} + \begin{Bmatrix} m_R g \\ 0 \end{Bmatrix} + \begin{Bmatrix} F_{\tilde{X},\text{ext}} \\ F_{\tilde{Y},\text{ext}} \end{Bmatrix} + \begin{Bmatrix} F_{\tilde{X}} \\ F_{\tilde{Y}} \end{Bmatrix}. \tag{V-2}$$

The right hand side of Equation (V-2) includes imbalance forces, weight of the rotor, external loads, and the bearing reaction force created by fluid film pressure between rotor and pads. The force on the rotor due to the fluid film pressure distribution is evaluated by

$$\begin{Bmatrix} F_{\tilde{X}} \\ F_{\tilde{Y}} \end{Bmatrix} = p_a R^2 \sum_{\text{all pads}} \left(\iint P \begin{Bmatrix} \cos\theta \\ \sin\theta \end{Bmatrix} d\theta dZ \right). \tag{V-3}$$

Equations of motion of the pads for tilting and radial motion are respectively given by the following:

$$i_p \ddot{\phi} + k_\phi \phi = M_p \tag{V-4}$$

$$m_p \left(\ddot{\delta} - \ddot{\tilde{x}}_{BS} \cos\theta_p - \ddot{\tilde{y}}_{BS} \sin\theta_p \right) + c_\delta \dot{\delta} + k_\delta \delta = F_{p,\text{normal}} \tag{V-5}$$

In Equation (V-4), M_p is the moment exerted on the pad by the gas film given by

$$M_p = p_a R^3 \iint (P-1)\sin(\theta-\theta_p)\, d\theta dZ\,, \tag{V-6}$$

and in Equation (V-5), $F_{p,\text{normal}}$ is the normal reaction force exerted on the pad by the gas film in the δ-direction. The pads are assumed to be rigid to the bearing shell in the transverse direction (due to short length of the flexure pivot); thus a force balance on a pad in the transverse direction gives the holding force exerted by the bearing shell on the pad as

$$F_{p,\text{hold}} = F_{p,\text{trans}} - m_p\left(\ddot{\bar{x}}_{BS}\sin\theta_p - \ddot{\bar{y}}_{BS}\cos\theta_p\right). \tag{V-7}$$

The normal and transverse forces acting on the pads due to the gas film are considered with fluid shear components assuming Couette-dominated velocity profiles:

$$F_{p,\text{normal}} = p_a R^2 \iint (P-1)\cos(\theta-\theta_p) d\theta dZ - \frac{\mu R^3 \Omega}{C}\iint \frac{\sin(\theta-\theta_p)}{H} d\theta dZ \tag{V-8}$$

$$F_{p,\text{trans}} = p_a R^2 \iint (P-1)\sin(\theta-\theta_p) d\theta dZ + \frac{\mu R^3 \Omega}{C}\iint \frac{\cos(\theta-\theta_p)}{H} d\theta dZ \tag{V-9}$$

It was found that the effect of the fluid shear forces on the pad have the largest influence in the transverse direction, but is one order-of-magnitude less than the normal-pressure-related counterpart (Equation (V-9)). The shear component is three orders-of-magnitude smaller than the pressure component in the pad radial direction (Equation

(V-8)). Shear forces are considered in the pad translational formulations, but are ignored in the tilting formulation (Equation (V-6)) because they have a negligible effect on the pad rotational motion due to relatively short moment-arm to the pad pivot [5, 27]. Shear forces acting on the rotor are also assumed to have negligible effects on the rotor motion, thus they are also excluded in Equation (V-3).

Equations of motion for the bearing shell are

$$m_{BS}\begin{Bmatrix}\ddot{\tilde{x}}_{BS}\\ \ddot{\tilde{y}}_{BS}\end{Bmatrix}+c_{BS}\begin{Bmatrix}\dot{\tilde{x}}_{BS}\\ \dot{\tilde{y}}_{BS}\end{Bmatrix}+k_{BS}\begin{Bmatrix}\tilde{x}_{BS}\\ \tilde{y}_{BS}\end{Bmatrix}$$

$$=\sum_{\text{all pads}}\left(\begin{bmatrix}-\cos\theta_p & \sin\theta_p\\ -\sin\theta_p & -\cos\theta_p\end{bmatrix}\begin{Bmatrix}c_\delta\dot{\delta}+k_\delta\delta\\ F_{p,\text{hold}}\end{Bmatrix}\right)+\begin{Bmatrix}m_{BS}g\\ 0\end{Bmatrix}. \tag{V-10}$$

Equations (V-7) and (V-10) are a system of differential-algebraic equations (DAEs) for the second-derivative terms $\ddot{x}_{BS}$ and $\ddot{y}_{BS}$ and the algebraic term $F_{p,\text{hold}}$. Thus, Equation (V-7) may be substituted into Equation (V-10) to eliminate dependence on $F_{p,\text{hold}}$, resulting in the new equations of motion of the bearing shell as (after some algebraic manipulation and the use of Cramer's rule):

$$\begin{Bmatrix}\ddot{\tilde{x}}_{BS}\\ \ddot{\tilde{y}}_{BS}\end{Bmatrix}=\begin{Bmatrix}C_1B_2-B_1C_2\\ A_1C_2-C_1A_2\end{Bmatrix}\frac{1}{A_1B_2-B_1A_2} \tag{V-11}$$

where

$$
\left.
\begin{aligned}
A_1 &= m_{BS} + m_p \sum_{\text{all pads}} \left(\sin^2 \theta_p\right) \\
A_2 = B_1 &= -m_p \sum_{\text{all pads}} \left(\sin\theta_p \cos\theta_p\right) \\
B_2 &= m_{BS} + m_p \sum_{\text{all pads}} \left(\cos^2 \theta_p\right) \\
C_1 &= \sum_{\text{all pads}} \left[-\left(c_\delta \dot{\delta} + k_\delta \delta\right)\cos\theta_p + F_{p,\text{trans}} \sin\theta_p\right] \\
&\qquad - c_{BS}\dot{x}_{BS} - k_{BS} x_{BS} + m_{BS} g \\
C_2 &= \sum_{\text{all pads}} \left[-\left(c_\delta \dot{\delta} + k_\delta \delta\right)\sin\theta_p - F_{p,\text{trans}} \cos\theta_p\right] \\
&\qquad - c_{BS}\dot{y}_{BS} - k_{BS} y_{BS}
\end{aligned}
\right\} \qquad \text{(V-12)}
$$

Equations (V-2), (V-4), (V-5), and (V-11) are numerically integrated to determine the time response of the twelve state variables (rotor: 2, bearing shell: 2, and pads: 2×4=8). A Runge-Kutta fourth-order method is used to integrate for the first five time steps, then a fifth-order Adams-Bashforth scheme is used for the remaining numerical integration as used by [5, 35].

Perturbation Method Simulation

Analysis by the orbit simulation method may require extensive computational effort, and it is sometimes difficult to identify sources of peculiar phenomena related to natural frequencies of moving elements within the rotor-bearing system. Due to the highly nonlinear nature of the equations of motion, identification of system natural

frequencies from the equations is impossible. A linear analysis provides a method for predicting various natural frequencies existing in the system by utilizing linearized bearing impedance coefficients which are found by a perturbation method. Although this analysis is based on a small displacement approximation, it can be useful for explaining interesting rotordynamic behaviors shown by orbit simulations. In this manner, a linear analysis can be a useful, complimentary analysis method to orbit simulation predictions.

The details of the perturbation method simulation that follow are a summary of the work presented by Sim and Kim [22] and Kim et al. [27], although some notation may be different. The formulation in [22] is for a FPTPGB-C and a fixed bearing shell, i.e. $\tilde{x}_{BS} = \tilde{y}_{BS} \equiv 0$. The perturbation method assumes small oscillations of the rotor and pads at the same excitation frequency Ω. The Reynolds equation considered for this analysis has the same form as Equation (V-1) with a bearing number of $\Lambda = (6\mu\omega / p_a)(R/C)^2$, but a difference is that time is normalized by the excitation frequency (i.e. $\tau = \Omega t$) which makes the squeeze number become $\sigma = 2\Lambda\nu$, where excitation frequency ratio $\nu = \Omega / \omega$. A complex notation allows the perturbed rotor and pad motions about static equilibrium positions (subscript '0') to be represented by the following:

$$\varepsilon_{\tilde{X},\tilde{Y}} = e_{\tilde{X},\tilde{Y}} / C = (\varepsilon_{\tilde{X},\tilde{Y}})_0 + (\Delta\varepsilon_{\tilde{X},\tilde{Y}})e^{i\tau} \tag{V-13}$$

$$\Psi = \delta / C = (\Psi)_0 + (\Delta\Psi)e^{i\tau} \tag{V-14}$$

$$\Phi = R\phi / C = (\Phi)_0 + (\Delta\Phi)e^{i\tau} \tag{V-15}$$

The non-dimensional film thickness and hydrodynamic pressure expressions may be represented by $H = h/C = (H)_0 + (\Delta H)e^{i\tau}$ and $P = p/p_a = (P)_0 + (\Delta P)e^{i\tau}$, respectively. Substitution of these equations into the Reynolds equation yields the zeroth-order Reynolds equation given by Equation (V-16), four first-order Reynolds equations given by Equation (V-17), and higher order terms which are ignored. In Equation (V-17), the H_α and P_α terms represent the partial derivatives of the film thickness and pressure with respect to the rotor and pad perturbations ($\alpha = \tilde{X}, \tilde{Y}, \Psi, \Phi$), respectively. For example, $H_\Psi = \partial H / \partial\Delta\Psi = \partial\Delta H / \partial\Delta\Psi$.

$$\frac{\partial}{\partial\theta}\left(P_0 H_0^3 \frac{\partial P_0}{\partial\theta}\right) + \frac{\partial}{\partial Z}\left(P_0 H_0^3 \frac{\partial P_0}{\partial Z}\right) = \Lambda \frac{\partial}{\partial\theta}\left(P_0 H_0\right) \tag{V-16}$$

$$\begin{aligned} &\frac{\partial}{\partial\theta}\left[P_0 H_0^3 \frac{\partial P_\alpha}{\partial\theta}\right] + \frac{\partial}{\partial\theta}\left[\left(3H_0^2 P_0 H_\alpha + H_0^3 P_\alpha\right)\frac{\partial P_0}{\partial\theta}\right] \\ &+ \frac{\partial}{\partial Z}\left[P_0 H_0^3 \frac{\partial P_\alpha}{\partial Z}\right] + \frac{\partial}{\partial Z}\left[\left(3H_0^2 P_0 H_\alpha + H_0^3 P_\alpha\right)\frac{\partial P_0}{\partial Z}\right] \\ &= \Lambda \frac{\partial}{\partial\theta}\left(P_0 H_\alpha + P_\alpha H_0\right) + \sigma i\left(P_0 H_\alpha + P_\alpha H_0\right) \end{aligned} \tag{V-17}$$

Substituting Equations (V-13)-(V-15) into Equation (IV-1) yields the expanded form of the perturbed film thickness:

$$\Delta H = \Delta\varepsilon_{\tilde{X}} \cos\theta + \Delta\varepsilon_{\tilde{Y}} \sin\theta + \Delta\Psi \cos\left(\theta - \theta_p\right) - \Delta\Phi \sin\left(\theta - \theta_p\right) \tag{V-18}$$

Thus, differentiating Equation (V-18) by each of the rotor and pad perturbations gives:

$$H_{\tilde{X}} = \cos\theta,\ H_{\tilde{Y}} = \sin\theta,\ H_{\Psi} = \cos\left(\theta - \theta_p\right),\ H_{\Phi} = -\sin\left(\theta - \theta_p\right) \tag{V-19}$$

The expanded form of the perturbed pressure has the form of Equation (V-20), but unlike the perturbed film thickness partial derivatives, the individual P_α terms are unknown and must be solved for. The partial derivatives of the pressures with respect to the pad perturbations are related to the partial derivatives of the pressures with respect to the rotor perturbations by a coordinate transformation as shown in Equation (V-21).

$$\Delta P = P_{\tilde{X}} \Delta\varepsilon_{\tilde{X}} + P_{\tilde{Y}} \Delta\varepsilon_{\tilde{Y}} + P_{\Psi} \Delta\Psi + P_{\Phi} \Delta\Phi \tag{V-20}$$

$$\begin{Bmatrix} P_{\Phi} \\ P_{\Psi} \end{Bmatrix} = \begin{bmatrix} \sin\theta_p & -\cos\theta_p \\ \cos\theta_p & \sin\theta_p \end{bmatrix} \begin{Bmatrix} P_{\tilde{X}} \\ P_{\tilde{Y}} \end{Bmatrix} \tag{V-21}$$

The solution procedure to calculate the perturbed pressures begins with selecting a rotor speed ω and calculating the equilibrium positions of the rotor and pads which gives the equilibrium film thickness H_0 and pressure distribution P_0 from Equation (V-16). Next, an excitation frequency $\Omega = \nu\omega$ is selected and Equation (V-17) is solved for the $P_{\tilde{X}}$ and $P_{\tilde{Y}}$ pressure gradients. The solutions of Equations (V-16) and (V-17) are

carried out in a similar manner as the solutions of the Reynolds equation in the orbit simulation, using a central difference scheme with Gauss-Seidel iteration (mesh size is doubled to 26×16 per half-pad for better differentiation results). Then, the P_Φ and P_Ψ pressure gradients are calculated by the coordinate transformation of Equation (V-21). Finally, the perturbed pressure fields are integrated over the pads to obtain impedances (complex stiffness and damping) which are represented in dimensional form as $z_{\alpha\beta} = k_{\alpha\beta} + i\Omega c_{\alpha\beta}$ (more details can be seen in [22, 27]). Thus, the equation for perturbed motions of the pads can be written as:

$$\left(-\Omega^2\left[m_p\right]+\left[z_p\right]\right)\begin{Bmatrix}\Delta\phi\\ \Delta\delta\end{Bmatrix} = -\left[z_1\right]\begin{Bmatrix}\Delta e_{\tilde{X}}\\ \Delta e_{\tilde{Y}}\end{Bmatrix} - \left[z_2\right]\begin{Bmatrix}\Delta\phi\\ \Delta\delta\end{Bmatrix} \tag{V-22}$$

Here, $\left[m_p\right]$ and $\left[z_p\right]$ are the mass and impedance matrices from the mechanical properties of the pads, and $\left[z_1\right]$ and $\left[z_2\right]$ are the impedance matrices from the perturbation calculations. The expressions for these matrices are:

$$\left[m_p\right] = \begin{bmatrix} i_p & 0 \\ 0 & m_p \end{bmatrix}, \left[z_p\right] = \begin{bmatrix} k_\phi & 0 \\ 0 & k_\delta + i\Omega c_\delta \end{bmatrix},$$
$$\left[z_1\right] = \begin{bmatrix} z_{\phi\tilde{X}} & z_{\phi\tilde{Y}} \\ z_{\delta\tilde{X}} & z_{\delta\tilde{Y}} \end{bmatrix}, \left[z_2\right] = \begin{bmatrix} z_{\phi\phi} & z_{\phi\delta} \\ z_{\delta\phi} & z_{\delta\delta} \end{bmatrix} \tag{V-23}$$

The perturbed reaction force on the rotor contributed from all pads is equated to the equivalent representation of total bearing impedances and rotor motions. This expression is written in Equation (V-24), where $[z_3]$ and $[z_4]$ are impedance matrices from the perturbation calculations shown in Equation (V-25), and $[Z_R]$ is the total bearing impedance matrix with respect to rotor eccentricities from equilibrium. The total bearing impedance matrix is calculated by isolating $\{\Delta\phi, \Delta\delta\}^T$ in Equation (V-22) and substituting into Equation (V-24), resulting in the final form of Equation (V-26).

$$\sum_{\text{all pads}} \left([z_3] \begin{Bmatrix} \Delta e_{\tilde{X}} \\ \Delta e_{\tilde{Y}} \end{Bmatrix} + [z_4] \begin{Bmatrix} \Delta\phi \\ \Delta\delta \end{Bmatrix} \right) = [Z_R] \begin{Bmatrix} \Delta e_{\tilde{X}} \\ \Delta e_{\tilde{Y}} \end{Bmatrix} \tag{V-24}$$

$$[z_3] = \begin{bmatrix} z_{\tilde{X}\tilde{X}} & z_{\tilde{X}\tilde{Y}} \\ z_{\tilde{Y}\tilde{X}} & z_{\tilde{Y}\tilde{Y}} \end{bmatrix}, \quad [z_4] = \begin{bmatrix} z_{\tilde{X}\phi} & z_{\tilde{X}\delta} \\ z_{\tilde{Y}\phi} & z_{\tilde{Y}\delta} \end{bmatrix} \tag{V-25}$$

$$[Z_R] = \sum_{\text{all pads}} \left\{ [z_3] - [z_4] \left([z_2] + [z_p] - \Omega^2 [m_p] \right)^{-1} [z_1] \right\} \tag{V-26}$$

CHAPTER VI

EXPERIMENTAL FACILITY

A rig for testing flexure pivot tilting pad gas bearings (FPTPGBs) had been constructed for previous works[2]. However, as described in Chapter III, improvements were required in order to enhance thrust bearing stability, increase maximum operating speed beyond 120 krpm, and improve data acquisition and data processing capabilities. A new rotor, rotor turbine drive system, and thrust bearings were made, and a new computer data acquisition program was developed to accomplish the improvements. This chapter continues to describe the details of the current experimental facility, including the test rig components and test bearings, the data acquisition system, and the data processing methods.

Overview of Test Rig Layout

The FPTPGB test rig contains a solid, stainless steel rotor with six-bladed impulse turbines on the ends, machined as a single component (Figure VI-1). The rotor also has radial patterns of tapped holes at each end for the addition of imbalance masses. General properties of the rotor are shown in Table VI-1. The previous rotor was a similar design with impulse turbines; however, it was hollow, requiring the turbines to be attached to the rotor as an assembly. The new rotor was chosen to be solid for several reasons: A solid rotor is easier to machine than a hollow rotor, especially with turbines

[2] "Previous" is used in this chapter to describe activities done before the author's current experience with the testing equipment (i.e. test rig, rotor, bearings, etc.).

that are easier to machine from the ends of the solid rotor than assemble with a hollow rotor (e.g. avoid necessity for shrink-fitting, welding, etc.). A solid rotor also has less centrifugal growth than a hollow rotor [5], which is beneficial for high speed operation since centrifugal growth consumes the bearing clearance and can be a limit on maximum operating speed. Although centrifugal growth may also be a stabilizing mechanism for a rotor-bearing system [5], properly designed bearings do not need this feature.

Refer to Table VI-2 and Figure VI-2 for the following descriptions of the test rig layout: The rotor is supported by two FPTPGBs, each contained within a bearing housing. The bearings are aligned and fixed to the bearing housings (see Appendix A for procedure). Locations of the bearings are to the outsides of the bearing housings as shown in Figure VI-2(a), and vibration sensors are mounted to the inside of the bearings. Outboard to the bearing housings are turbine shroud and thrust nozzle assemblies (Figure VI-2(b)), which deliver pressurized air to drive the impulse turbines and for aligning and supplying air to the thrust bearings. Figure VI-3(a) shows the offset of pressurized air inlets in the turbine shroud which provide the circular flow that drives the impulse turbine. Figure VI-3(b) shows the end surface of the thrust nozzle, where an array of four 0.5 mm diameter feed holes supply the air for the air film that exists between the turbine end (see Figure VI-1) and the thrust nozzle surface – the thickness of the air film is approximately 5 mils (0.127 mm). Finally, a tachometer is located at the center of the rotor, between bearing housings. Further descriptions of the test rig components and setup may be found in Appendix A.

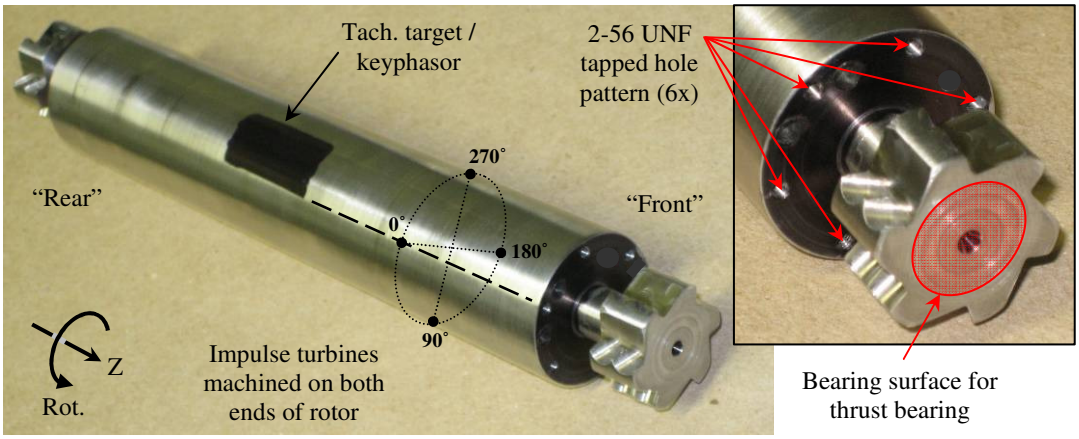

Figure VI-1: Test rig rotor with impulse turbines.

Table VI-1: Test rig rotor properties.

Property	Value	
Total rotor mass	1.77 lbm	(0.802 kg)
Approx. journal diameter	1-1/8 in.	(28.6 mm)
Approx. bearing span	4 in.	(100 mm)
Overall length	7-1/2 in.	(190 mm)

Table VI-2: Key to labeling in Figure VI-2.

Label	Component
A	Rotor with impulse turbines
B	Flexure pivot tilting pad gas bearings
C	Bearing housings
D	Horizontal proximity probes
E	Vertical proximity probes
F	Turbine shroud and thrust nozzle assemblies
G	Tachometer

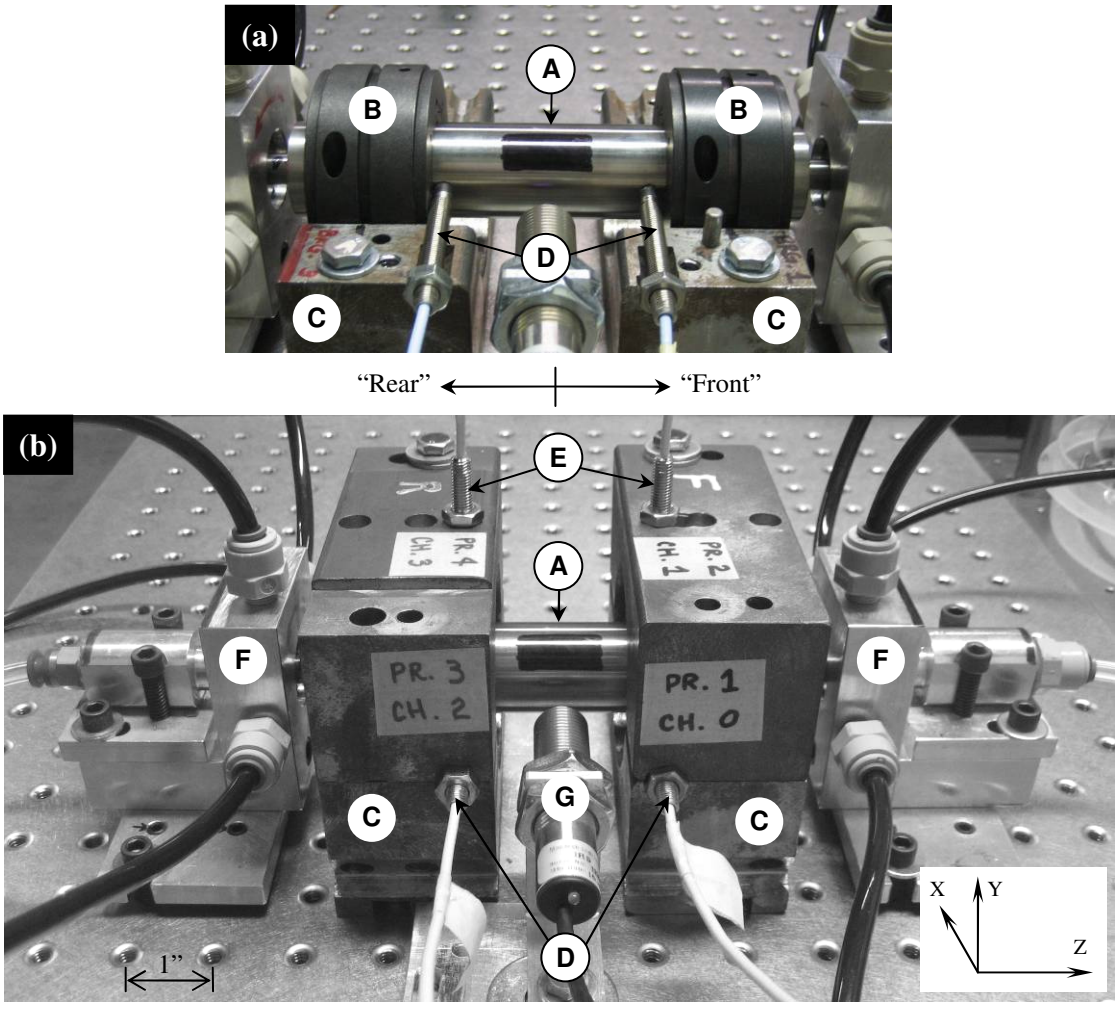

Figure VI-2: **Flexure pivot tilting pad gas bearing test rig – (a) bearing / sensor placement; (b) full assembly.**

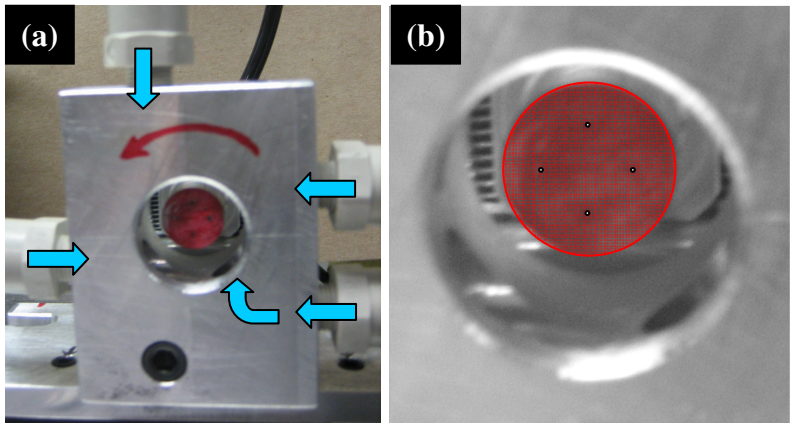

Figure VI-3: **End view of turbine shroud and thrust nozzle assembly – (a) offset pressurized air inlets create circular flow for driving impulse turbines; (b) magnified view shows face of thrust nozzle with circular array of air supply orifices (4 x 0.5 mm diameter).**

Test Bearings

The test bearings are FPTPGB-Cs and have been used extensively in experimental studies that predate the author's experience on the present work. Over the life of the bearings, there were two occasions where the bearing coatings were replaced – the procedure first involved media blasting to remove the old coating before applying new Teflon® coating according to the original specifications. There were three bearings that were used in the experimental studies: one of the two bearings in the initial setup was damaged and needed to be replaced by a backup bearing. All three bearings were measured after recoating; the summary of the measurements are shown in Table VI-3. It is worthy to note the large variation in the estimated clearances of the bearings is due to the relatively large deviation in the measured set bore diameters in the axial direction. Full details of the bearing measurements and clearance estimation is presented in Appendix B.

The initial setup (Setup #1) used Bearings 1 and 3 since the axial variance in the measured set bores was the smallest. The original dimensions of the rotor were specified based on this set of bearing measurements resulting in an estimated nominal clearance of 33-34 microns. During testing with Setup #1, damage occurred to the rotor and Bearing 1, the details of which are found in Chapter VII. The rotor was refurbished (notice the slight decrease in rotor journal diameter in Table VI-3), and Bearing 2 was used in place of Bearing 1. The new setup (Setup #2) resulted in an estimated nominal clearance of approximately 35 microns for both bearings. Note the larger range for Bearing 2 is due to much higher variation of measured set bore diameters in the axial direction than with Bearing 3.

Table VI-3: **Summary of rotor-bearing clearance estimation based on 15 micron preload radius – measurement data and estimation of variance presented in Appendix B. Units are inches unless otherwise noted.**

Parameter	Bearing 1	Bearing 2	Bearing 3
Setup #1	*Rotor "Front"*	-	*Rotor "Rear"*
Rotor dia. ($2R$)	1.1277 ± 0.00005 (28.644 ± 0.001 mm)	-	1.1294 ± 0.00005 (28.687 ± 0.001 mm)
C_{SB}	0.0007 ± 0.0002 (18.2 ± 4.4 μm)	-	0.0008 ± 0.0002 (19.1 ± 5.0 μm)
C	0.0013 ± 0.0002 (33.2 ± 4.9 μm)	-	0.0013 ± 0.0002 (34.1 ± 5.5 μm)
Setup #2	-	*Rotor "Front"*	*Rotor "Rear"*
Rotor dia. ($2R$)	-	1.1274 ± 0.00005 (28.636 ± 0.001 mm)	1.1293 ± 0.00005 (28.684 ± 0.001 mm)
C_{SB}	-	0.0008 ± 0.0003 (19.9 ± 7.9 μm)	0.0008 ± 0.0002 (20.3 ± 5.0 μm)
C	-	0.0014 ± 0.0003 (34.9 ± 8.4 μm)	0.0014 ± 0.0002 (35.3 ± 5.5 μm)

The remaining FPTPGB-C properties are related to the pad characteristics: number of pads, pad offsets, pad orientations, pad masses and radial stiffnesses, and pad tilting moments of inertia and tilting stiffnesses. Radial stiffnesses were measured and found to be larger, and tilting stiffnesses were found to be lower than previously estimated by simple beam calculations (ref. Appendix B). The summary of the remaining parameters of the test bearings are shown in Table VI-4.

Table VI-4: Additional pad-related test bearing parameters.

Parameter	Value	
No. pads	4	
Pad offset	0.7	
Pad span	80	degree
Start angle of first pad	5	degree
Pad mass, m_p	0.016	kg
Pad tilting moment of inertia, i_p	1.0×10^{-6}	kg-m^2
Pad radial stiffness, k_δ		
• Lower pads	1.5×10^{7}	N/m
• Upper pads	0.8×10^{7}	N/m
Pad tilting stiffness, k_ϕ	20	N-m/rad

Instrumentation and Data Acquisition

As described in the overview of the test rig layout, instrumentation for the experimental studies consists of four proximity probes to measure rotor vibrations and a tachometer. The proximity probes are eddy current sensors which are set up as orthogonal pairs in two planes (approximately 2-1/4" apart) as shown in Figure VI-2(b). Preliminary testing used an optical tachometer which required the use of a reflective tape target. The tachometer was upgraded to an infrared tachometer which was able to use a black marker as the target. The advantages of using black marker versus reflective tape are smaller mass addition to the rotor for large duty cycle targets and the elimination of the possibility of the tachometer target becoming detached during high speed operation. Full details of instrument specifications and calibration are presented in Appendix A.

Recall that a commercial rotordynamics data acquisition system available in the laboratory (ADRE 208 DAIU [32]) could not be used since it was limited to measuring rotor speeds only up to 60 krpm, requiring a new data acquisition system to be able to measure vibrations at higher rotor speeds. The signals from the instruments are processed by a data acquisition program created in *LabVIEW*. Digital sampling of the signals was set to 20,000 samples at a rate of 100 kHz. The sample rate has the capability to capture up to 25X frequency components at 120 krpm[3], which far exceeds the specification of measuring 3X frequencies at 120 krpm. However, it was determined that the higher sample rate was required in order to save a sufficient amount of data points that would yield satisfactory results after processing the data with a digital

[3] Maximum frequency = ½ x (100 kHz) (60 s/min) = 3,000 krpm = 25 x 120 krpm.

bandpass filtering algorithm (ref. Appendix C). Live-display monitoring capabilities of the data acquisition program include time signal displays of the proximity probes and tachometer signal, XY plots of the rotor-center locus, rotor spin speed, and FFT frequencies of the time signals. The time signal data and FFT data may be saved at any time or for multiple times during coast-down tests. A post-processing program written in MATLAB reads the various saved files and performs several tasks, including: filtering proximity probe digital time signals to extract the synchronous component (or other desired components), determine synchronous vibration amplitude and phase lag, and create cascade plots of the FFT data. More descriptions of the data acquisition system components, setup, and features are presented in Appendix A.

CHAPTER VII

EXPERIMENTAL STUDIES: TEST RIG PERFORMANCE AND EFFECT OF BEHIND-PAD DAMPER ON STABILITY

This chapter outlines all of the experimental testing performed with the test rig described in Chapter VI. The scope of the testing involves (1) evaluation of the test rig operating at high speeds, including imbalance response, and (2) evaluation of viscoelastic dampers applied behind the pads of FPTPGB-Cs. To the author's knowledge, hydrodynamic stability of FPTPGB-rotor systems (comparable in size to the bearings and rotor in this work) has only been demonstrated successfully up to ~81 krpm, where subsynchronous instability was observed [28]. However, previous design studies used to design the current bearing set[4] predict stability beyond 140 krpm [5, 22]. As will be presented in the following sections, operation of the current FPTPGB-rotor system is demonstrated beyond 120 krpm for the first time.

As introduced in Chapter I, a pad surface with radial compliance can tolerate rotor growths due to centrifugal and thermal effects. As presented, the radial compliance structures found in FPTPGB-Cs represents a beam spring (Figure I-1(c-d)), and the second aspect of the experimental scope evaluates the performance of FPTPGB-Cs with dampers added behind this structure to enhance stability. Since the rotor-bearing system

[4] Cited references involve studies that were used to design the current bearings; however, several differences exist between the parameters in the design studies and the actual parameters of the bearings and rotor of the current test rig. Namely, radial stiffness of the pads is higher (as identified by experiments) and the mass of the rotor is larger.

has stable operation beyond 120 krpm, the system is first made less stable by increasing the bearing clearance in the vertical direction. Then, dampers are applied and the rotordynamic response is evaluated to see if the threshold of instability is increased.

Initial Test Rig Evaluation with Setup #1

Initial testing with the test rig was performed with Bearings 1 and 3 (Setup #1) as described in Chapter VI; the parameters of the rotor and bearings are shown in Table VI-3 and Table VI-4. Coast-down tests were performed, wherein the rotor is brought up to a desired speed by manually controlling the flow of pressurized air flowing through the turbine shrouds to the impulse turbines (source pressure at ~80-100 psi before ball valve), and then closing off the supply pressure to the turbine shrouds allowing the rotor speed to be reduced by air drag effects. The general sequence for the coast down tests is as follows: the rotor is brought up to maximum speed in a relatively short amount of time (~10 seconds), the data acquisition system saving mode is activated, and the turbine supply pressure is turned off as quick as possible. The data acquisition system saving mode is deactivated once the rotor is stopped.

Figure VII-1 shows the synchronous response Bode plots of a coast down test from above 112 krpm. The vibration amplitudes for the horizontal and vertical vibration probes (and the major amplitude of the elliptical orbit) are displayed as zero-to-peak in microns (Note: horizontal = X-direction, vertical = Y-direction, and rotation in $+Z$-direction as shown in the test rig schematic in Figure VI-2). Phase angles are negative, indicating phase lag measurements. Note that at each probe station, the vertical lags the horizontal by approximately 90˚ and the "Front" and "Rear" orbits are nearly in phase at high speeds, indicating the presence of forward, cylindrical, near-circular rotor precession. Below 40 krpm, this appears to no longer hold as indicated by the change in phase angles and asymmetry of the "Front" and "Rear" Bode plots. Exact imbalance levels along the rotor are unknown; however estimating 700 mg-mm at each bearing results in a 1.7 micron imbalance radius, which is approximately the level of vibration amplitude at high speeds from the experiment.

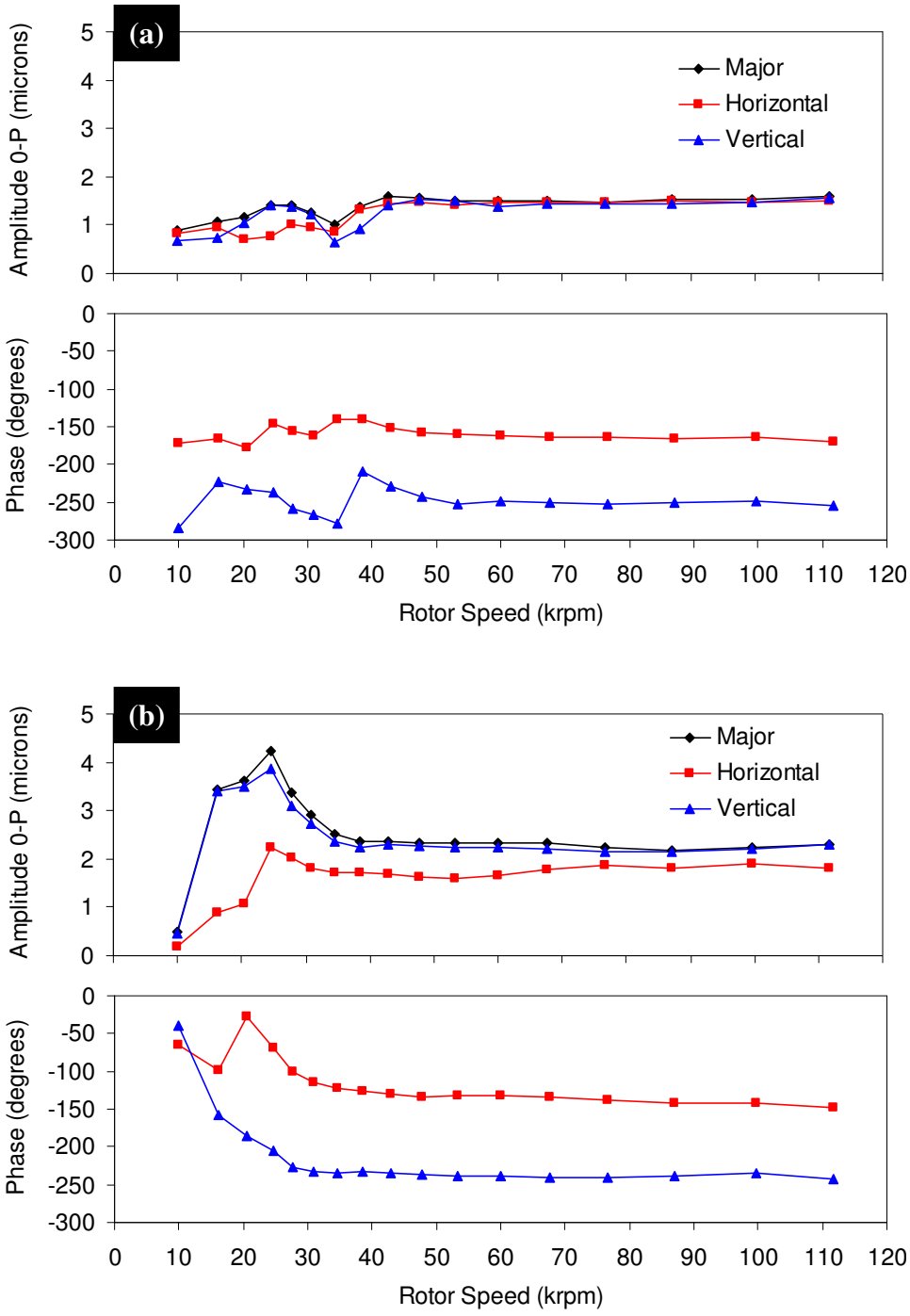

Figure VII-1: **Synchronous response Bode plots for test rig Setup #1 for (a) "Front" and (b) "Rear" probe stations. Hydrodynamic stability shown above 112 krpm.**

The orbit simulation was used to model the rotor-bearing system using 700 mg-mm imbalance and nominal clearances of 31-34 microns, which is within the range of the estimated bearing clearances shown in Table VI-3. Recall that nominal clearances of the bearings were estimated and had rather large uncertainties due to the axial variation of the measured set bore clearances. Other bearing parameters are as shown in Table VI-4. Plots of the predicted synchronous vibration amplitudes are compared with the major amplitude for the "Rear" probe station in Figure VII-2. Critical speeds are predicted between 15-22 krpm, increasing as nominal clearance decreases and the bearing becomes stiffer. Amplitudes also increase because smaller gas film has less damping – similar results were also shown in [5]. Nominal clearances of 31 and 32 microns were predicted to be stable as no subsynchronous vibrations were present for the entire speed range. Nominal clearances of 33 and 34 microns were predicted to be unstable for speed ranges of approximately 40-80 krpm and 30-120 krpm, respectively, due to subsynchronous rotor precession. The rotor precesses or whirls at its natural frequency, which is shown in Figure VII-3 for the 33 micron case. An interesting observation is that larger clearances may cause the rotor to experience subsynchronous whirling at relatively low speeds, but increasing the speed causes the system to self-stabilize.

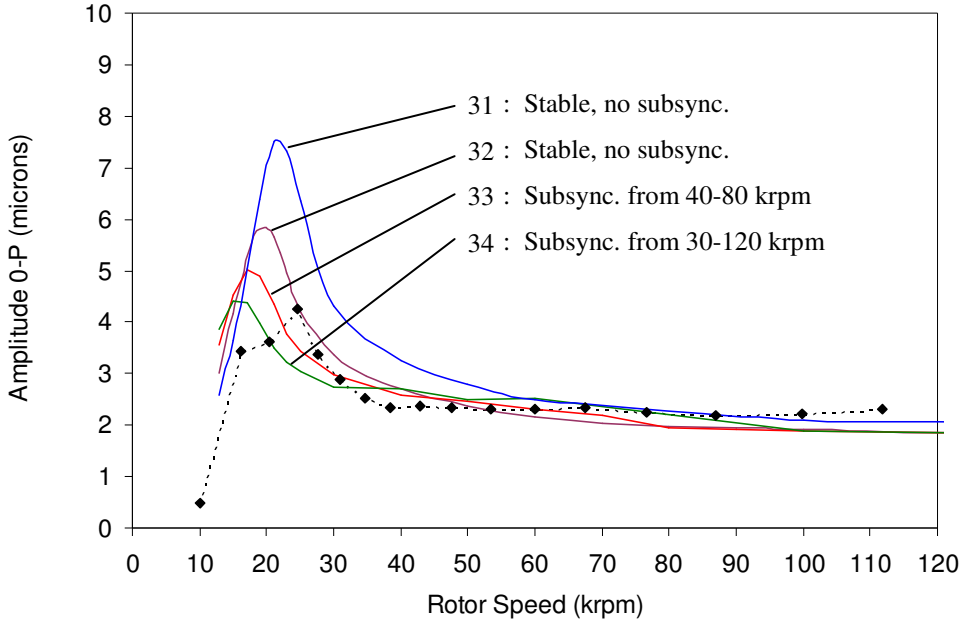

Figure VII-2: **Predicted synchronous response (filtered out subsynchronous for unstable cases) for rotor-bearing system with 700 mg-mm imbalance and nominal clearances of 31-34 microns. Results compared with major amplitude from "Rear" probe station for test rig Setup #1.**

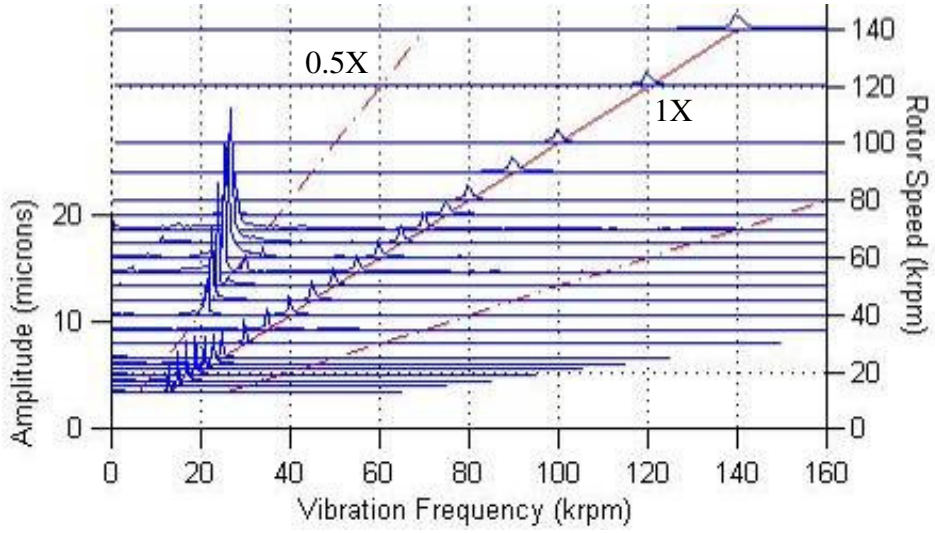

Figure VII-3: **Cascade plot of predicted response for 33 micron nominal clearance using orbit simulation. Stability is shown through 140 krpm even though subsynchronous rotor whirl is present from 40-80 krpm.**

The source of the stabilization is rotor growth which reduces the minimum film thickness and increases the effective preload. Figure VII-4 shows this effect by comparing the responses of the 33 micron bearing case with and without the rotor growth model given by Equation (IV-2). In both cases, subsynchronous vibrations appear at approximately the same speed, but as speed increases, the vibrations in the no-rotor-growth model eventually become too large, and the simulation predicts contact of the rotor and bearing. In the case where rotor growth is present, subsynchronous vibrations are consistently lower than the no-rotor-growth case, and eventually subsynchronous vibrations vanish completely.

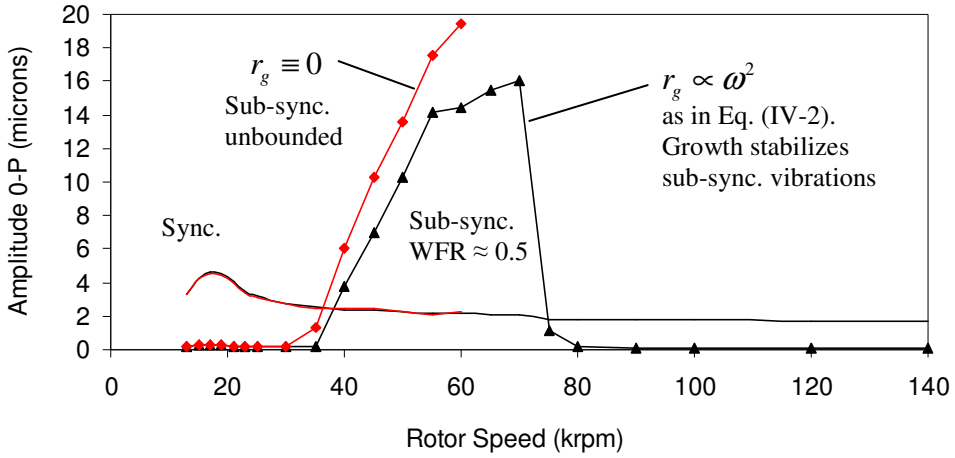

Figure VII-4: Predicted synchronous and subsynchronous responses for 33 micron nominal clearance and model comparing effect of centrifugal rotor growth. Rotor centrifugal growth stabilizes subsynchronous vibrations by increasing effective preload.

Figure VII-5 is the cascade plot for the "Rear Vertical" probe of the test rig for the same coast down test in Figure VII-1. The cascade plots for the other three probes are not included for brevity and since features of the plots are the same. The main observation is that the test rig is stable without any subsynchronous vibrations for the entire speed range up to 112 krpm. The source of large 2X vibrations is unknown, but is possibly related to alignment issues with the bearings, drive turbines, or thrust bearings, and also some level of rotor out-of-roundness[5]. The source of the 6X vibrations is likely related to the turbines which have six blades. Figure VII-6 shows a similar cascade plot for the maximum speed recorded in this study. No subsynchronous vibrations were present up to 121 krpm. Note: This is highest speed recorded by the data acquisition system, which saves data intermittently; actual highest speed observed was beyond 125 krpm before turbine supply pressure was turned off.

Multiple, consecutive coast down tests were performed with maximum rotor speeds above 110 krpm. While operating at 120+ krpm for an extended period of time, the "Front" bearing seized on the rotor. The next section discusses the potential causes of the rotor-bearing failure and gives the details of subsequent refurbishments.

[5] Slow-roll compensation is a typical method used to eliminate non-dynamic effects (such as rotor out-of-roundness and static sensor effects) from the rotor's vibration time signal. The method subtracts the response of the system recorded at a low speed (i.e. negligible dynamic effects) from all responses measured higher speeds (i.e. where dynamic effects are more prominent). In the current test rig, the lift-off speed of the rotor was ~6-10 krpm – too high to neglect dynamic effects – and could not be maintained steadily to obtain a proper slow-roll phasor measurement.

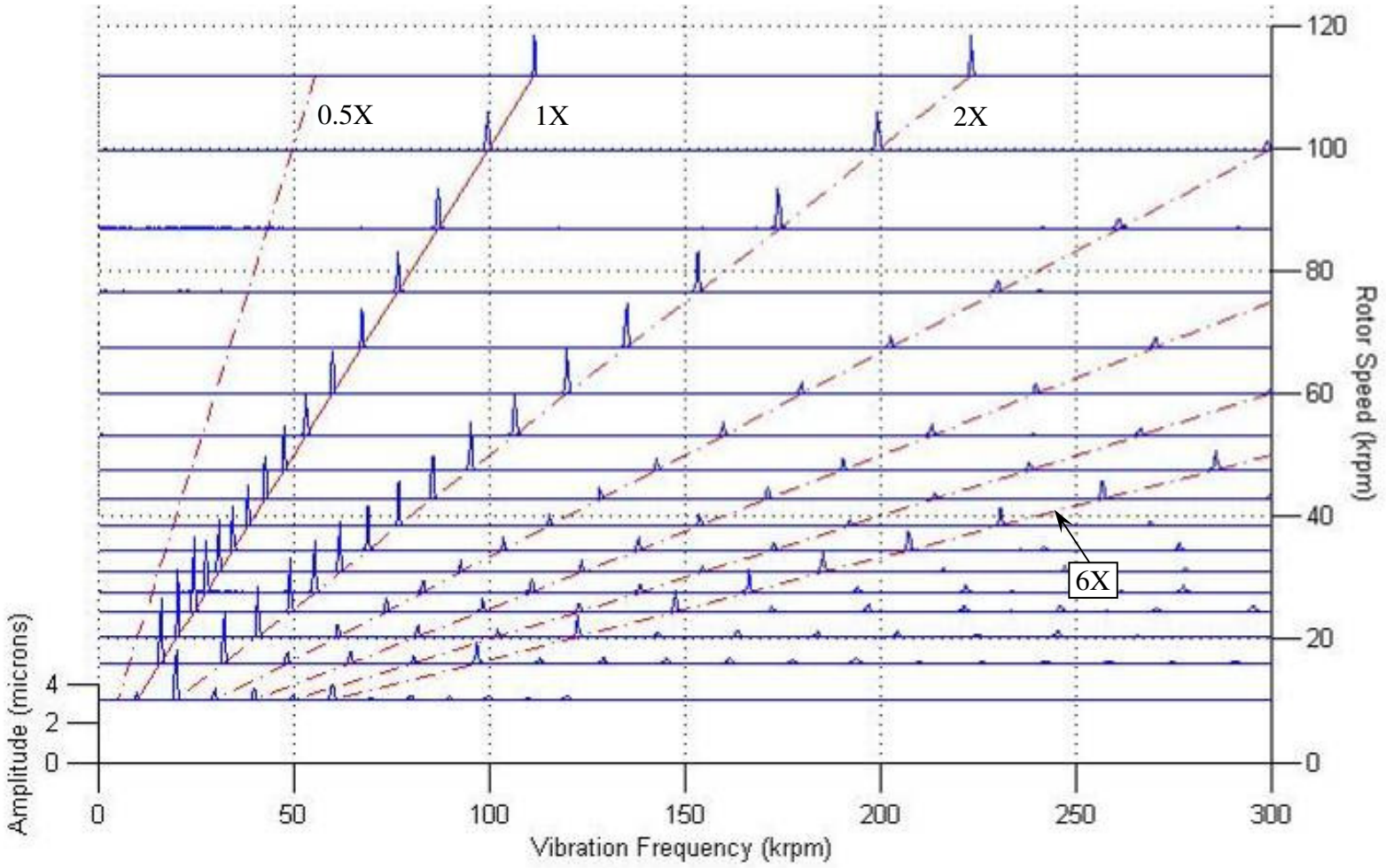

Figure VII-5: **Cascade plot for test rig Setup #1 – Response for "Rear Vertical" probe. Stability of the rotor-bearing system demonstrated beyond 112 krpm with no subsynchronous vibrations in range.**

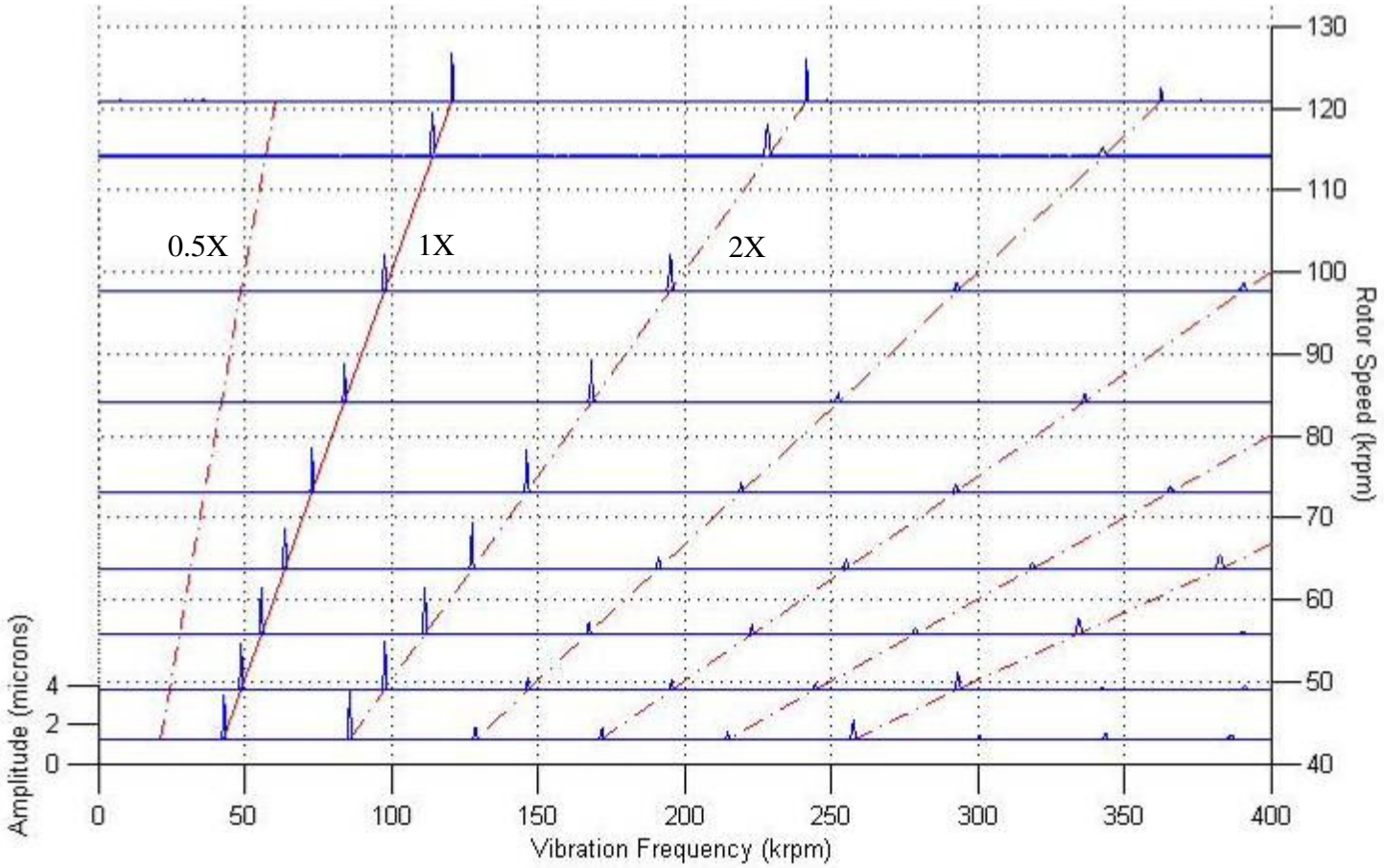

Figure VII-6: **Cascade plot for test rig Setup #1 – Response for "Rear Vertical" probe. Stability of the rotor-bearing system demonstrated beyond 120 krpm with no subsynchronous vibrations in range.**

Description of Rotor-Bearing Failure and Refurbishments

While operating at 120+ krpm for an extended period of time, the "Front" bearing (Bearing 1 for Setup #1) seized on the rotor, resulting in severe galling at a local circumferential region on both the rotor and bearing; however, the "Rear" bearing (Bearing 3) was completely undamaged (Figure VII-7). The failure mode appears to be adhesive wear, but the root cause is undetermined. Some levels of thermal rotor growth may have occurred during extended high speed running (unfortunately not quantified since temperatures were not monitored), resulting in further reduction of bearing clearance (i.e. apart from centrifugal growth alone).

In addition, gas bearings with very small clearances are susceptible to damage from debris infiltration. The test rig is not sealed off from the environment, and outside air is allowed to enter the bearing from between pads due to hydrodynamic operation. Observing that typical atmospheric dust may be as large as 30 microns [36], it is recognized that dust particles could be a serious threat to the rotor-bearing system at high speeds due to reduced clearances and the potential for large levels of frictional heating with relative surface velocities approximately equal to 180 m/s at 120 krpm.

Figure VII-7(a,b) shows evidence of rubbing which polished the rotor surfaces within both bearings. This is benign rubbing that occurred during starts/stops and is inevitable without hydrostatic operation. Figure VII-7(a) shows the damaged rotor surface which was discolored by extreme heating, and Figure VII-7(c) shows the corresponding location on a region of the "Front" bearing pad where the coating was

melted and base material (stainless steel) was removed. Figure VII-7(d) shows the state of both bearings after the incident.

The rotor was polished in an attempt to repair (diameter reduced slightly), but deep scratches (~1 mil, with narrow area much less than bearing surface are) remained on the surface (Figure VII-8). The original "Front" bearing, Bearing 1, was deemed unsalvageable and was replaced by Bearing 2 for the remaining experiments (Setup #2).

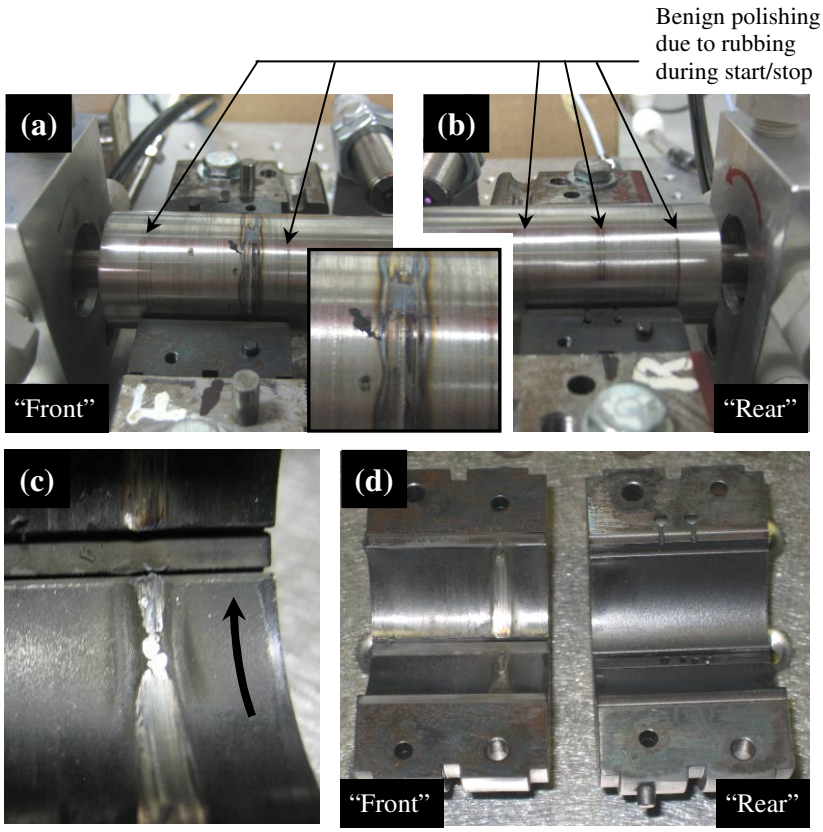

Figure VII-7: **Damaged rotor and bearing after seizure occurred while running at 120+ krpm for extended period. (a) Localized heating and micro-welding on circumference of rotor within "Front" bearing (inset shows magnified view of damaged region). (b) Undamaged rotor within "Rear" bearing. (c) Close-up of damage to "Front" bearing (arrow indicates rotor spin direction). (d) Side-by-side comparison of "Front" and "Rear" bearings to show condition after rotor-bearing system failure.**

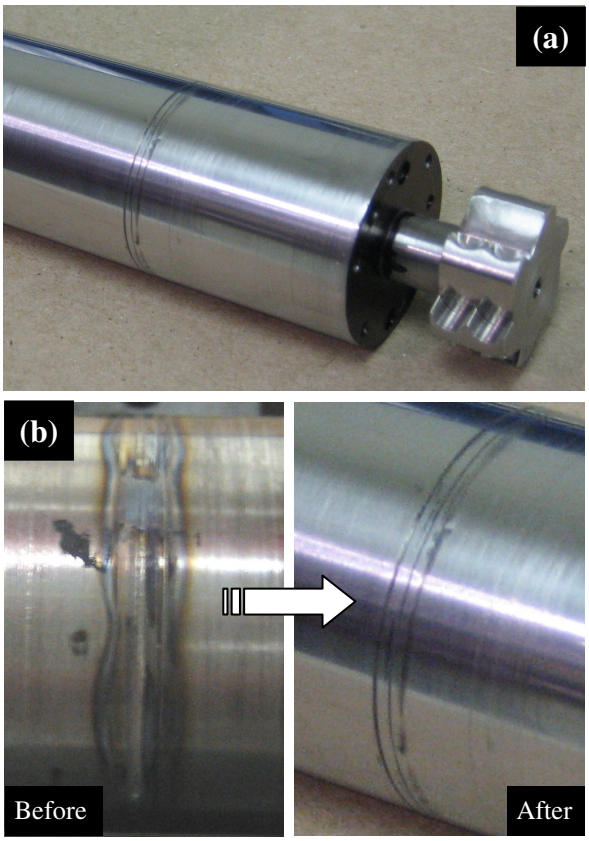

Figure VII-8: **Rotor after polishing to repair damaged surface. (a) "Front" end of rotor with remnant of deep grooves (~ 1 mil). (b) Before and after comparison of damaged region on rotor surface.**

Calibrated Imbalance Response Testing with Setup #2

Calibrated imbalance masses were added to the rotor in test rig Setup #2 to see the effect of imbalance on the system. Masses of 24, 40, and 53 mg (radius of 12 mm corresponds to 288, 480, and 636 mg-mm) were added to each end of the rotor at 0° (Figure VI-1), and coast down tests were performed up to 80 krpm. Large amplitudes of the vibrations for added imbalances of 40 and 53 mg prevented fully hydrodynamic

operation of the test rig below 27 and 31 krpm, respectively, due to the rotor apparently contacting the bearing surfaces near the critical speed around 20 krpm.

The synchronous Bode plots for the baseline imbalance response (no added imbalance) and the calibrated imbalance response with 288 mg-mm added in-phase at each end of the rotor are shown in Figure VII-9 and Figure VII-10, respectively. The specific speeds at which data points are collected by the data acquisition system are not set values, thus there are slight deviations between the speed at which data is shown in Figure VII-9 and the corresponding data in Figure VII-10. However, in the range of ~14-70 krpm, the speeds match up approximately within an order of ~100 rpm (see Table VII-1 and Table VII-2), and the two data are used to perform a baseline subtraction to determine the response to the calibrated 288 mg-mm imbalance. Figure VII-11 shows the results of the baseline subtraction compared with predicted responses to 288 mg-mm for 31 and 32 micron nominal clearances. Note that all phase angles have been shifted to compensate for the location of the vibration sensors with respect to the tachometer (see Appendix D). The predictions of the phase angles match very well with the data, and the predictions of the critical speeds and super-critical speed amplitudes are comparatively close. The peak amplitudes of the measurements have notable differences with predictions due to the sensitivity of this property to bearing nominal clearance. Large variations of the measured bearing nominal clearances can be attributed to this discrepancy.

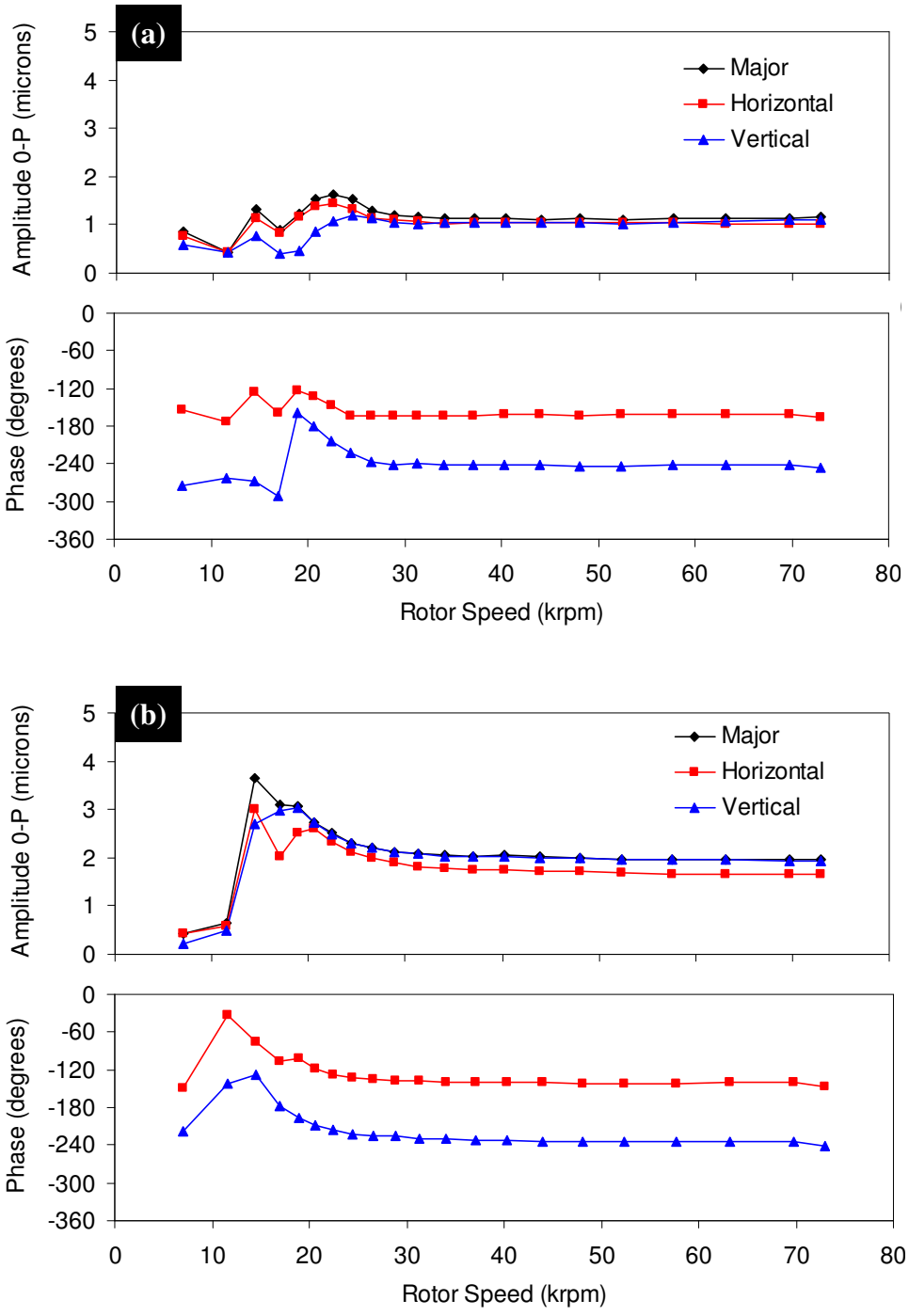

Figure VII-9: **Synchronous response Bode plots for test rig Setup #2 for (a) "Front" and (b) "Rear" probe stations. Baseline response without added imbalance.**

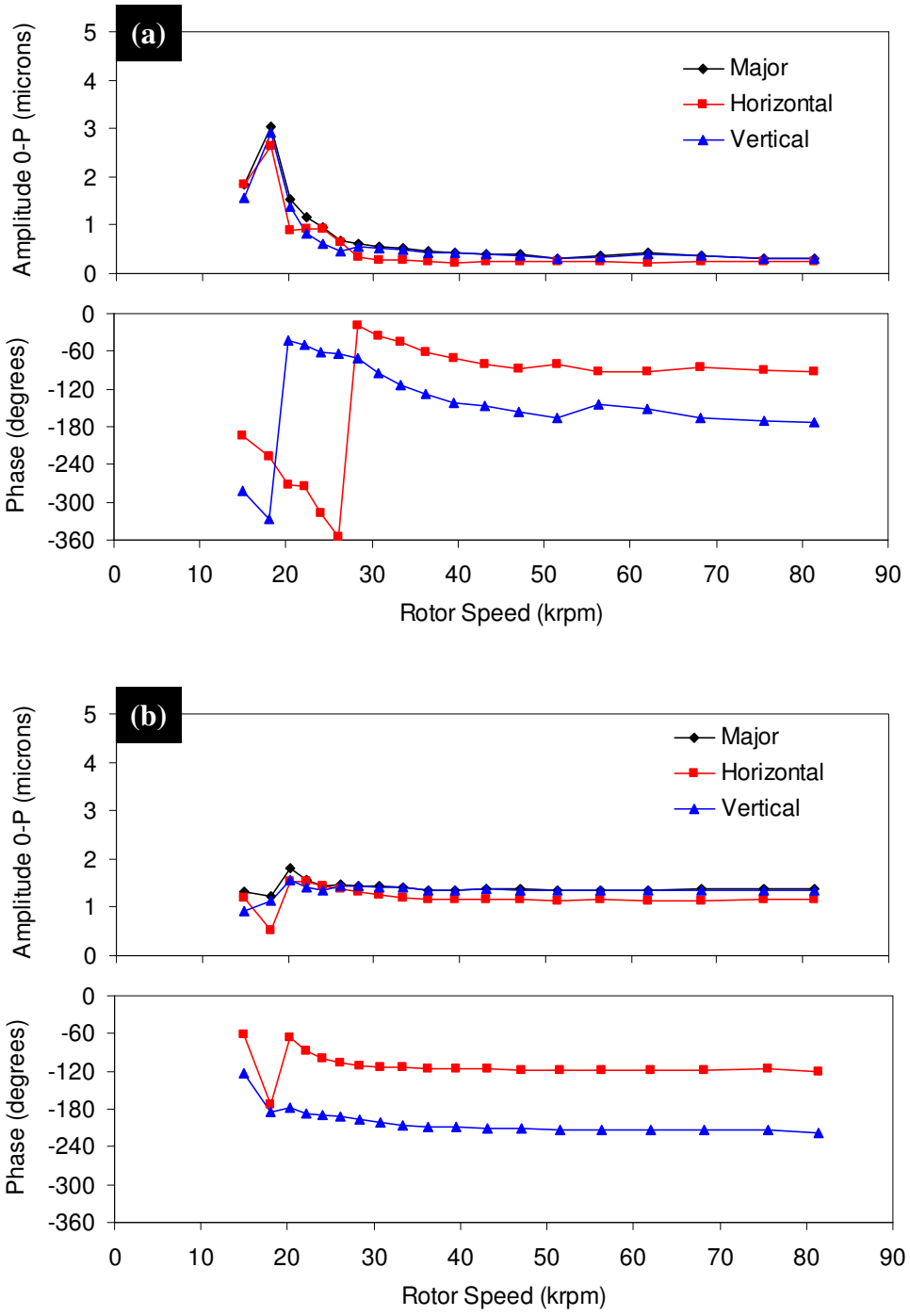

Figure VII-10: Synchronous response Bode plots for test rig Setup #2 for (a) "Front" and (b) "Rear" probe stations. In-phase imbalance of 288 mg-mm added to each end of rotor.

Table VII-1: Measured amplitude and phase angle data for test rig Setup #2 with baseline imbalance. Only speeds used for baseline subtraction presented.

krpm	Front				Rear			
	Horizontal		Vertical		Horizontal		Vertical	
	Amp.	Phase	Amp.	Phase	Amp.	Phase	Amp.	Phase
69.70	1.02	-159.9	1.10	-240.9	1.65	-139.6	1.94	-235.4
63.14	1.01	-161.3	1.08	-240.7	1.65	-140.8	1.95	-235.5
57.65	1.04	-162.1	1.04	-240.8	1.67	-141.7	1.95	-235.4
52.42	1.03	-161.8	1.02	-243.6	1.68	-141.5	1.96	-235.4
48.02	1.04	-162.4	1.05	-243.9	1.70	-141.3	1.99	-234.9
43.93	1.03	-161.7	1.05	-242.6	1.73	-140.8	2.01	-234.4
40.28	1.03	-162.1	1.06	-241.2	1.74	-140.2	2.04	-232.9
37.04	1.03	-162.8	1.04	-241.2	1.75	-140.0	2.03	-231.9
34.06	1.03	-164.1	1.03	-241.2	1.79	-138.7	2.04	-230.7
31.30	1.07	-164.0	1.03	-240.1	1.81	-137.0	2.07	-228.7
28.81	1.09	-163.5	1.06	-241.1	1.91	-137.6	2.12	-226.2
26.52	1.13	-163.6	1.14	-237.3	1.98	-135.3	2.20	-225.9
24.45	1.33	-162.6	1.20	-223.3	2.12	-132.4	2.30	-222.0
22.49	1.44	-146.0	1.08	-203.0	2.35	-127.6	2.50	-216.6
20.65	1.38	-133.1	0.85	-180.1	2.62	-117.3	2.72	-208.8
16.97	0.83	-157.6	0.40	-291.5	2.02	-107.5	2.98	-176.9
14.45	1.14	-124.8	0.77	-268.2	2.99	-76.4	2.71	-127.0

Table VII-2: Measured amplitude and phase angle data for test rig Setup #2 with 288 mg-mm added imbalance. Only speeds used for baseline subtraction presented.

krpm	Front				Rear			
	Horizontal		Vertical		Horizontal		Vertical	
	Amp.	Phase	Amp.	Phase	Amp.	Phase	Amp.	Phase
68.25	0.24	-85.92	0.37	-166.59	1.15	-117.31	1.35	-213.14
62.02	0.22	-92.38	0.41	-152.48	1.14	-119.21	1.35	-213.04
56.35	0.25	-91.93	0.34	-144.30	1.16	-119.48	1.33	-212.93
51.46	0.25	-80.71	0.30	-165.65	1.15	-118.54	1.36	-212.53
47.04	0.24	-87.12	0.37	-157.07	1.17	-118.02	1.36	-211.43
43.05	0.25	-80.22	0.39	-145.90	1.18	-116.31	1.37	-210.18
39.50	0.23	-71.81	0.42	-141.18	1.17	-116.40	1.34	-207.80
36.29	0.26	-62.28	0.44	-127.97	1.17	-115.63	1.35	-208.29
33.38	0.26	-44.27	0.50	-113.65	1.21	-114.79	1.41	-206.49
30.71	0.27	-35.01	0.52	-94.40	1.24	-114.17	1.43	-202.17
28.30	0.34	-19.52	0.56	-70.74	1.32	-111.63	1.43	-197.38
26.09	0.64	-355.24	0.45	-62.77	1.39	-105.94	1.44	-192.49
24.08	0.92	-317.23	0.63	-62.34	1.43	-99.04	1.34	-189.41
22.13	0.93	-274.29	0.84	-49.65	1.52	-88.31	1.40	-186.28
20.31	0.89	-271.22	1.39	-42.80	1.55	-66.24	1.56	-176.85
18.05	2.65	-227.17	2.92	-326.41	0.52	-172.25	1.13	-184.16
14.95	1.85	-195.36	1.56	-282.44	1.18	-61.51	0.92	-122.28

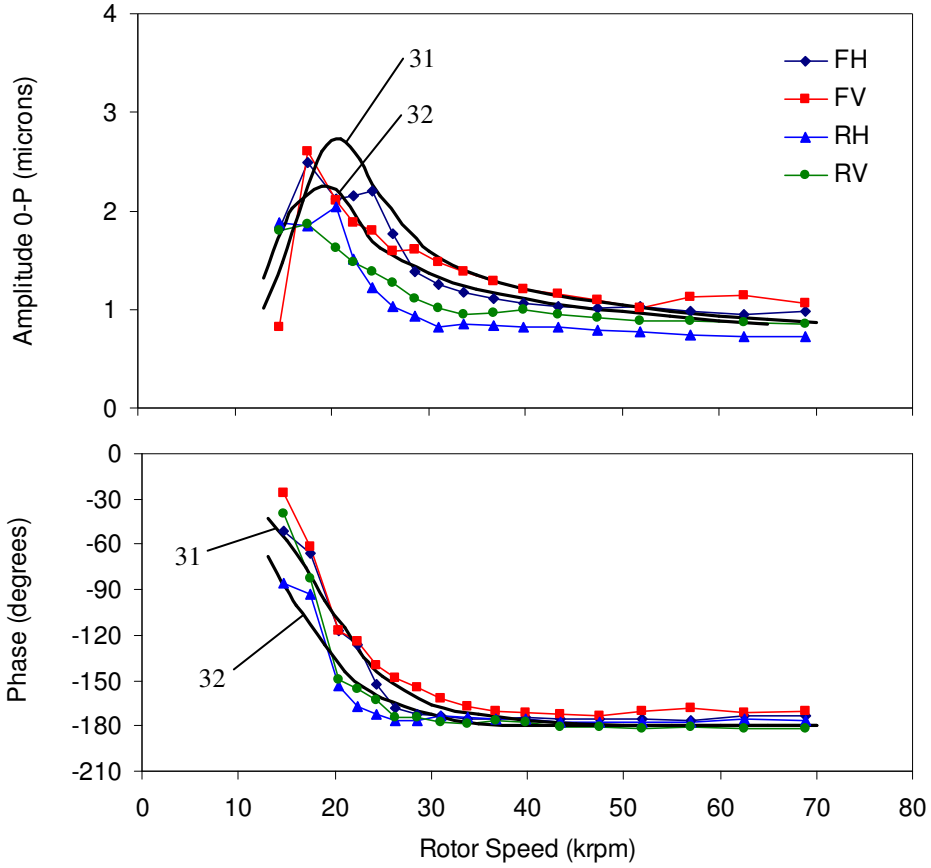

Figure VII-11: Imbalance response (baseline subtracted) for 288 mg-mm imbalance applied in phase at each end of rotor. Thick lines represent predictions for nominal clearances of 31 and 32 microns.

The effect of the larger imbalances of 480 and 636 mg-mm were also evaluated to compare linearity of the imbalance response. Table VII-3 presents the amplitude and phase angle data for all of the imbalance cases taken at approximately 70 krpm. This speed is well above the critical speed, thus phase angles of the responses are expected to lag the calibrated masses by 180˚, assuming symmetry of the system. To check this, the responses of the rotor without added imbalance (baseline) are vector-subtracted from the responses to the various imbalances. Table VII-4 represents the results of these calculations, where phase angles have also been shifted to compensate for the location of the vibration sensors with respect to the tachometer (see Appendix D). The phase angles are all close to -180˚, and the amplitudes closely follow a linear response to imbalance as indicated by Figure VII-12.

Table VII-3: Measured amplitude and phase angle data for test rig Setup #2 at ~70 krpm for different cases of added imbalance. Amplitudes in microns and phase angles in degrees.

Case	Front				Rear			
	Horizontal		Vertical		Horizontal		Vertical	
	Amp.	Phase	Amp.	Phase	Amp.	Phase	Amp.	Phase
baseline	1.02	-159.9	1.10	-240.9	1.65	-139.6	1.94	-235.4
288 mg-mm	0.24	-85.9	0.37	-166.6	1.15	-117.3	1.35	-213.1
480 mg-mm	0.71	-11.1	0.91	-104.4	0.89	-90.0	1.13	-185.5
636 mg-mm	1.23	-4.5	1.46	-99.1	0.93	-65.2	1.18	-161.3

Table VII-4: **Amplitude and phase angle data for baseline subtraction of data in Table VII-3. Amplitudes in microns and phase angles in degrees. Phase angles compensated for position of the vibration sensors with respect to the tachometer as explained in Appendix D.**

Case	Front				Rear			
	Horizontal		Vertical		Horizontal		Vertical	
	Amp.	Phase	Amp.	Phase	Amp.	Phase	Amp.	Phase
288 mg-mm	0.98	-173.2	1.06	-171.3	0.73	-173.5	0.86	-181.1
480 mg-mm	1.67	-173.2	1.87	-171.3	1.27	-173.5	1.49	-181.1
636 mg-mm	2.20	-173.2	2.42	-171.3	1.66	-173.5	1.98	-181.1

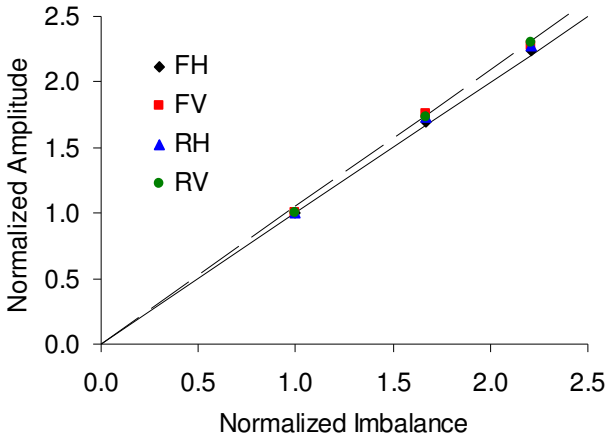

Figure VII-12: **Response amplitudes normalized by amplitude for 288 mg-mm vs. added imbalance normalized by 288 mg-mm. Solid line represents 1:1 and dashed line represents +5%.**

Testing with Dampers Behind Pad Radial Compliance Structure with Setup #2

Test rig Setup #1 was demonstrated to be capable of running beyond 120 krpm, but extended operation at high speeds eventually lead to failure of the "Front" bearing (Bearing 1). Recall that root causes for the failure were speculated, but not verified. Setup #2 replaces Bearing 1 with Bearing 2 as the "Front" bearing and continues to use Bearing 3 as the "Rear" bearing with a slightly modified rotor as described in a previous section. The rotor and bearing properties for Setup #2 are shown in Table VI-3; all other bearing properties are the same as Setup #1. The test rig Setup #2 was also shown to be very stable beyond 100+ krpm.

Experimental analysis

In order to test the effectiveness of dampers behind the pad radial compliance structure, the bearings were purposely made unstable by increasing the clearance in the vertical direction via placing shims between the upper and lower halves of the bearings (Figure VII-13). Then, dampers were used behind the pad radial compliance structure to try to enhance the stability. The damping material used was a 3M™ 110P05 viscoelastic damping polymer. The damper was used in its original packing, which is a laminate between layers of paper backing and plastic film, and was cut to fit in the wire-EDM gap (approximately ½-inch wide). Before inserting the damper, the thickness was compressed from approximately 13-14 mil to less than 12 mil to fit in the gap behind the pad radial compliance structure. Stiffness of the damper was estimated to be approximately $2\text{-}3\times10^{6}$ N/m based on pad natural frequency measurements with

installed dampers similar to those in Appendix B. Frequency-dependent damping properties are assumed to follow a structural model, and loss factors are estimated from the data sheet to range from 0.15-0.5 for operating temperatures from 20-25˚C [37].

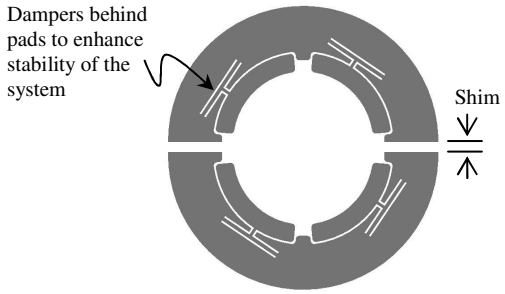

Figure VII-13: Adding shims between upper and lower bearing halves to increase vertical clearance and induce instability below 60-70 krpm, and adding dampers to enhance stability.

Figure VII-14 shows the synchronous response Bode plot of test rig Setup #2 with 3 mil shims inserted between upper and lower halves of the bearings. Figure VII-15 shows the corresponding plot for the case with the dampers. The effect of added damping to the system can only be effectively compared at the critical speed, and unfortunately the resolution of the measurements at this speed is poor due to large time between data points (~3-4 s), and the motion of the rotor is more complex (i.e. not simple cylindrical) as indicated by the phase angles below 20 krpm. The large time between data points is a limitation of the developed data acquisition system, and it is caused by the high sample rate (100 kHz and 20,000 samples) and the data saving demands (0.9 MB per FFT file and 2.0 MB per time signal file) on the desktop computer used, which tended to "bog down" with these parameters. Recall that the high sample

rate and number of samples was selected in order to have sufficient data for digital filtering in the post-processing tasks, which could give reliable results above 6 krpm (Appendix C). Due to the above reasons, the added damping to the system could not be properly evaluated for the synchronous response (i.e. estimate damping ratios), but the comparisons will made for the subsynchronous responses.

Figure VII-16 and Figure VII-17 show the corresponding cascade plots for the "Rear Vertical" probe for the no-damper and with-damper cases, respectively. Both cases exhibit regions with subsynchronous vibrations from approximately 20-25 krpm (WFR $\approx$ 0.5) and also at high speeds (WFR $\approx$ 0.23-0.26). Figure VII-18 shows the comparison of the subsynchronous vibration response (i.e. 1X and higher frequencies filtered out of raw signal) that captures the beneficial behavior of the damper: Namely, the damper helps to suppress the subsynchronous vibrations at high speed to increase maximum operating speed (without subsynchronous vibrations) by approximately 16%. However, subsynchronous vibrations at the midrange are minimally affected by the damper.

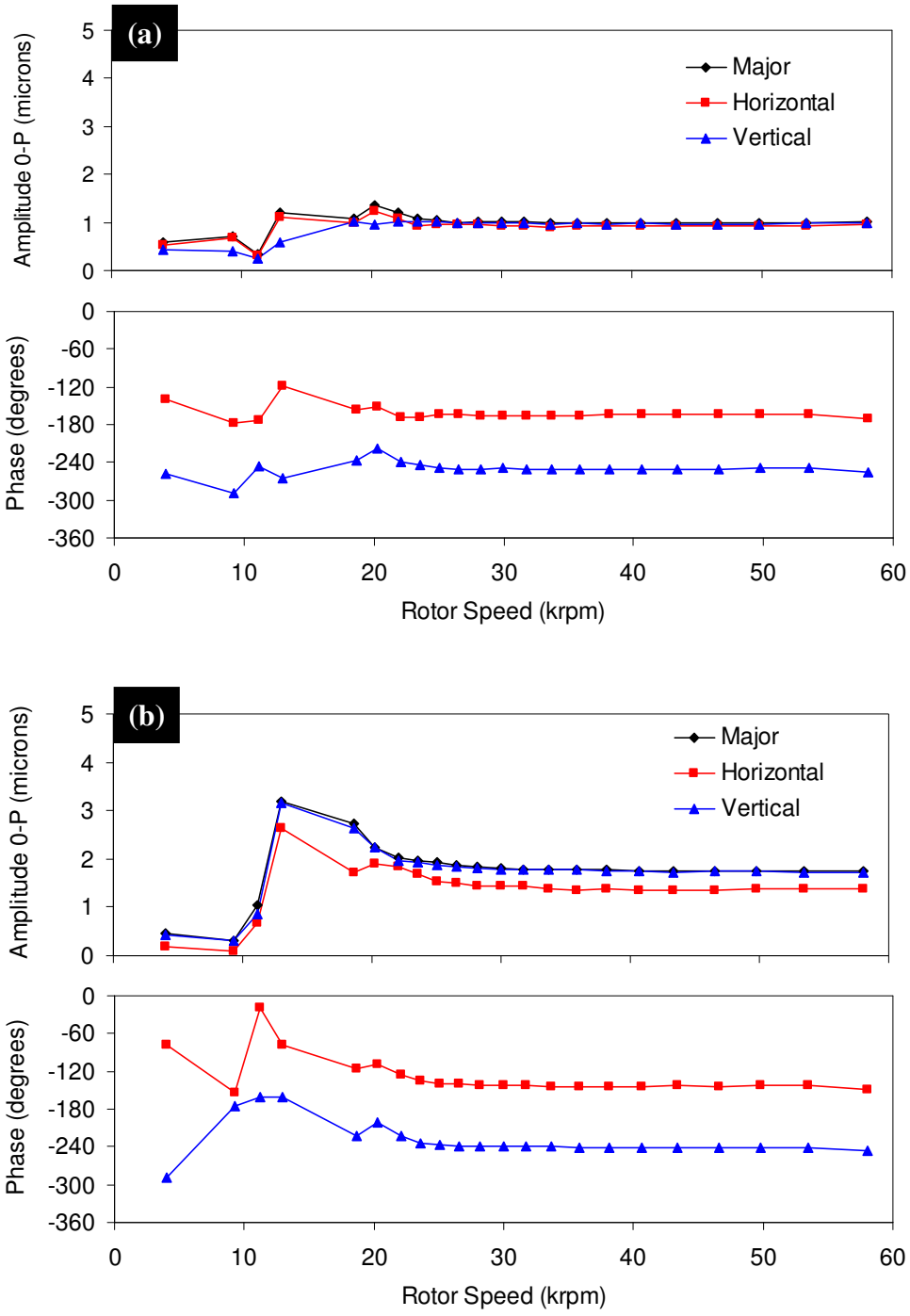

Figure VII-14: **Synchronous-filtered response Bode plots for test rig Setup #2 with 3 mil shim and no damper for (a) "Front" and (b) "Rear" probe stations. Subsynchronous vibrations occurred from approx. 20-25 krpm and above 43 krpm.**

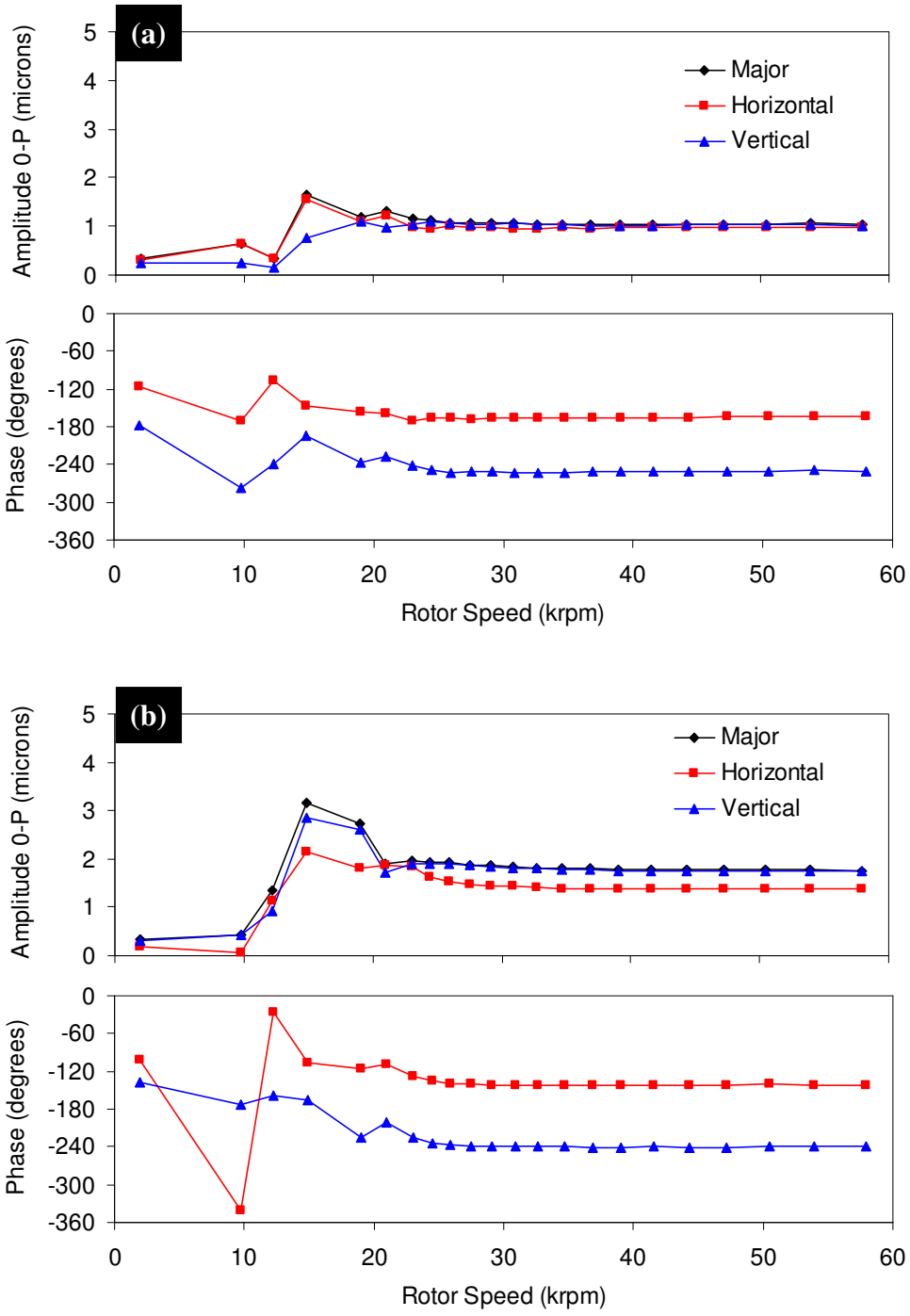

Figure VII-15: **Synchronous response Bode plots for test rig Setup #2 with 3 mil shim and with added damper for (a) "Front" and (b) "Rear" probe stations. Subsynchronous vibrations occurred from approx. 21-26 krpm and above 50 krpm.**

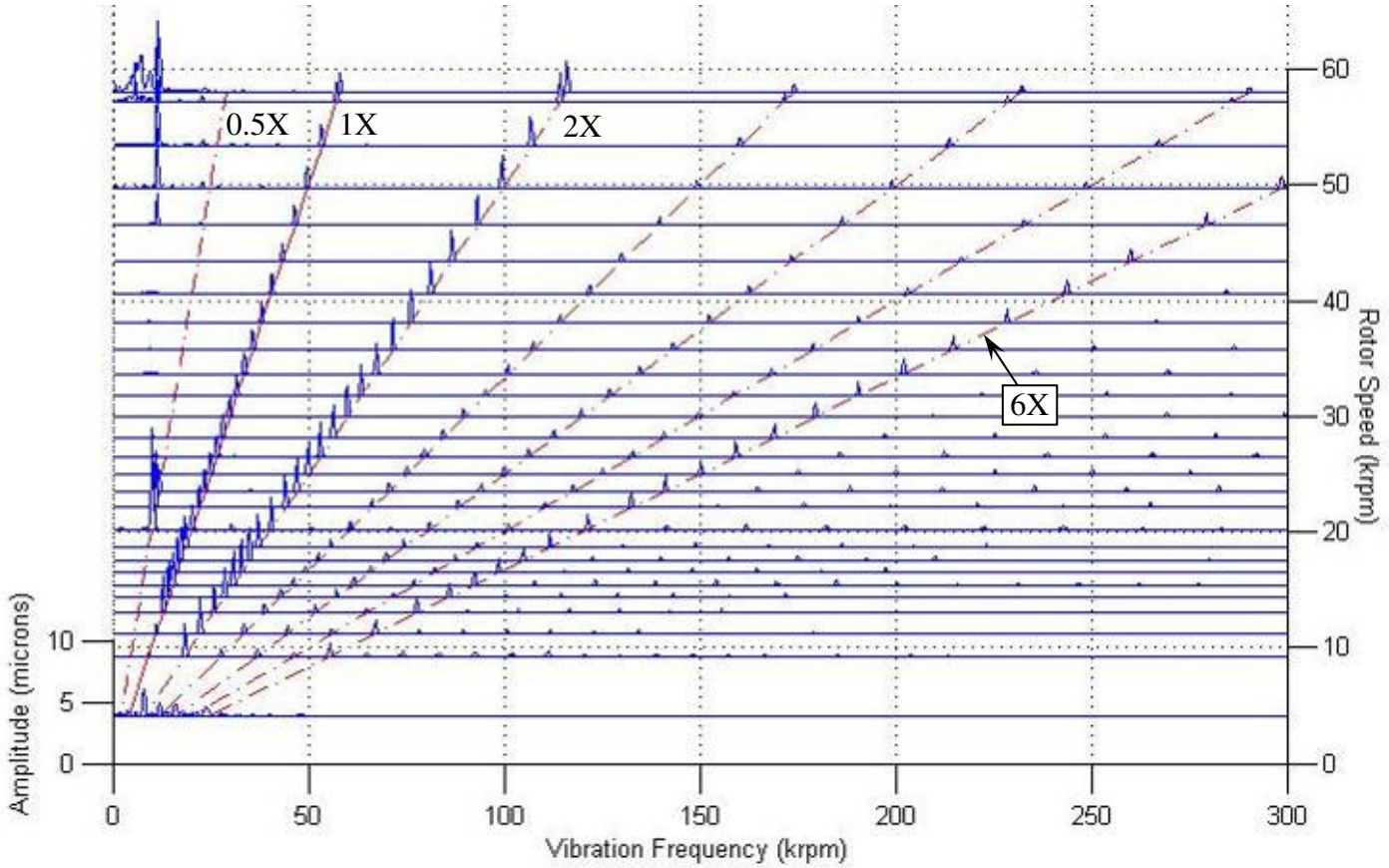

Figure VII-16: Cascade plot for test rig Setup #2 with 3 mil shim and no damper – Response for "Rear Vertical" probe.

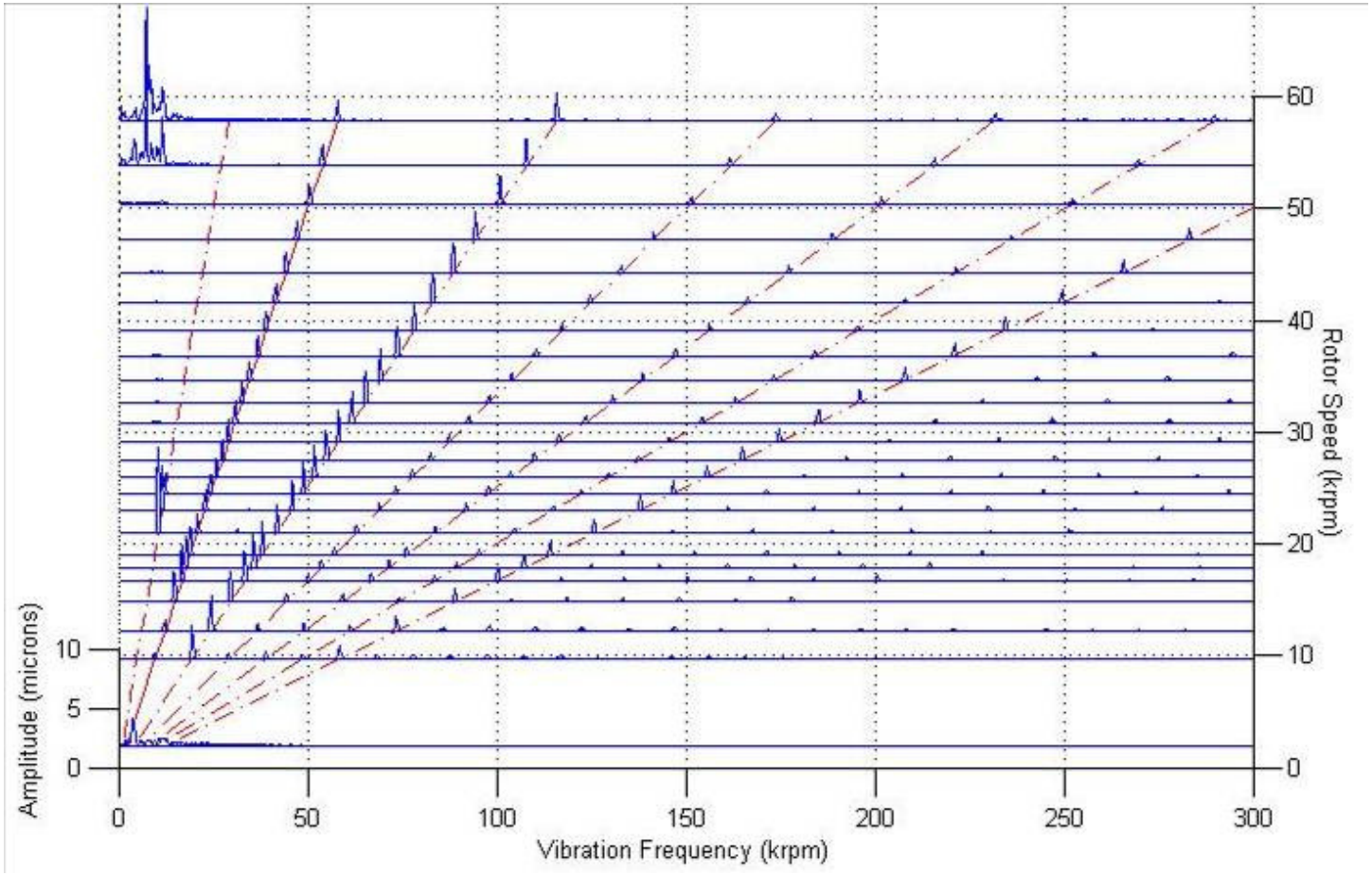

Figure VII-17: Cascade plot for test rig Setup #2 with 3 mil shim and with damper – Response for "Rear Vertical" probe.

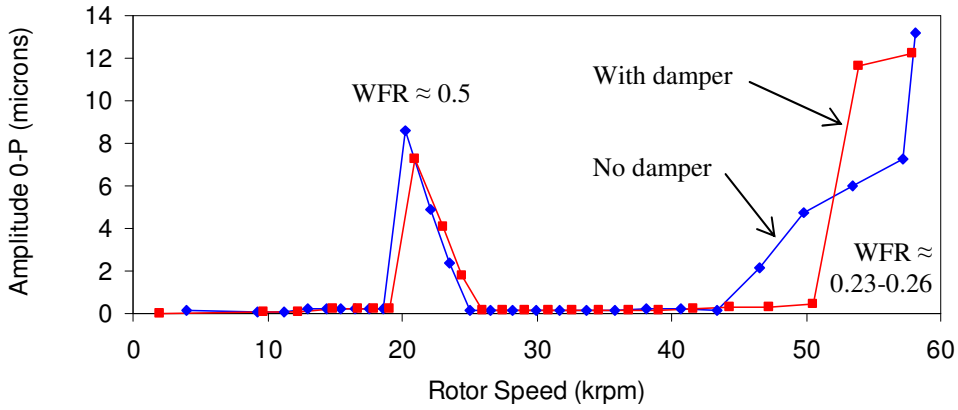

Figure VII-18: Comparison of subsynchronous responses for Setup #2 with 3 mil shim with and without damper for "Rear Vertical" probe. Damper has little effect on subsynchronous vibrations that occur at the middle of the speed ranges, but damper increases maximum operating speed by 16%.

Simulation analysis

A shim of 3 mil was required to destabilize the rotor-bearing system at below 60 krpm as shown in the above results. Shims of 1-2 mil were also used, but the system was still stable at speeds up to the maximum attempted speed of 105 krpm. However, both cases still exhibited the appearance of subsynchronous vibration with WFR ≈ 0.5. The trend of becoming unstable with WFR ≈ 0.5 and re-stabilizing to reach higher operating speeds was also shown by the orbit simulations as nominal clearance increases (cf. Figure VII-3). Recall that the ability to re-stabilize was shown to be the positive effect of rotor centrifugal growth. The orbit simulation was also employed to consider the effect of splitting the bearing by adding shims. The effect of the shim is modeled in the film thickness expression, Equation (IV-1), by adding $\frac{1}{2} d \left| \cos\theta \right|$, where d is the

shim thickness. Simulations in this case showed the same tendency to cause instability in the middle regions of the operating range; however, instability at higher speed was not seen even up to 200+ krpm. Also, the simulation shows a higher sensitivity to the split offset effect since it is drastically affected by a split an order of magnitude smaller than the ones imposed on the test rig.

Figure VII-19 shows the predicted responses (vertical direction) for the case of a bearing with a nominal clearance of 30 micron and a split of 0.25 mil – one-twelfth the shim thickness added to the bearings in the test rig. For the ideally modeled case (i.e. uniform bearing geometry, perfect bearing alignment, etc.), the bearing has subsynchronous vibrations occurring from after 35 krpm to after 65 krpm. Adding various dampers (see Table VII-5) improves the response by reducing the amplitudes of the subsynchronous vibrations. Note that an increase in stiffness affects the amplitudes in a similar manner as increasing loss factor. This is because damping in the structural model is proportional to stiffness and loss factor (i.e. $c_{damp} \propto \eta k_{damp}$); however, there is also the effect of added radial stiffness of the pad because of the damper ($k_{\delta} = k_{beam} + k_{damp}$). The stiffness effect is isolated in the simulation results shown in Figure VII-20, where the same dampers are applied neglecting the added stiffness effect (i.e., $k_{\delta} = k_{beam}$ only). The results in this case indicate that the addition of damper stiffness alone has a significant effect. For comparison, Figure VII-21 shows the simulation with 32 micron nominal clearance, but the larger clearance meant that it was even more sensitive to the split effect and could only tolerate a thinner shim. Note that the subsynchronous response for the 32 micron case with 0.125 mil shim is still worse

than the 30 micron case with 0.25 mil shim: Damper 1 reduces maximum subsynchronous vibrations by 58% in Figure VII-19, but only by 35% in Figure VII-21.

Table VII-5: Properties of dampers used in orbit simulations.

Loss Factor / Stiffness	0.15	0.25
2×10^6 N/m	Damper 1	Damper 2
4×10^6 N/m	Damper 3	Damper 4

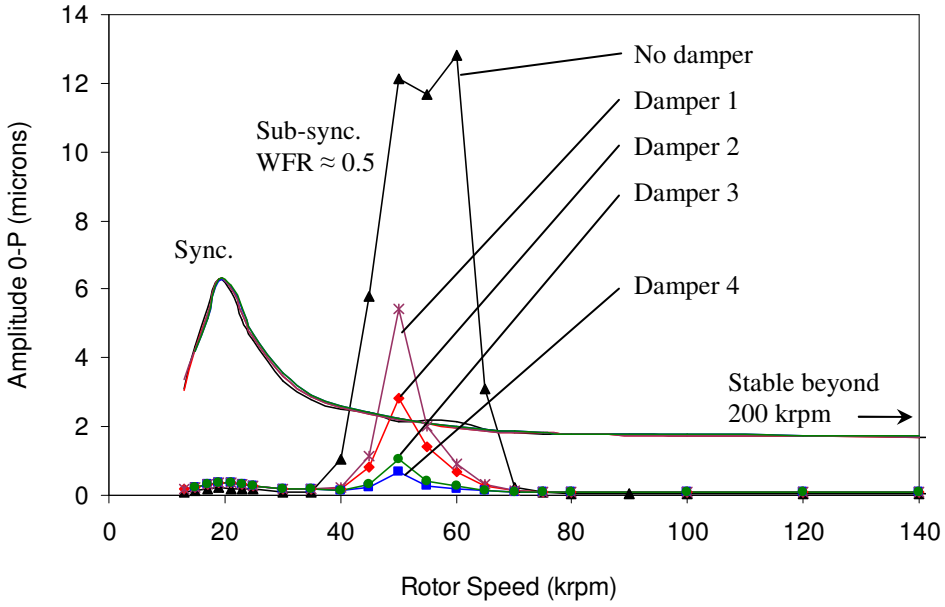

Figure VII-19: Predicted vertical responses for rotor-bearing system with split offset (0.25 mil) in bearing – nominal clearance 30 micron. Dampers added to suppress subsynchronous vibrations.

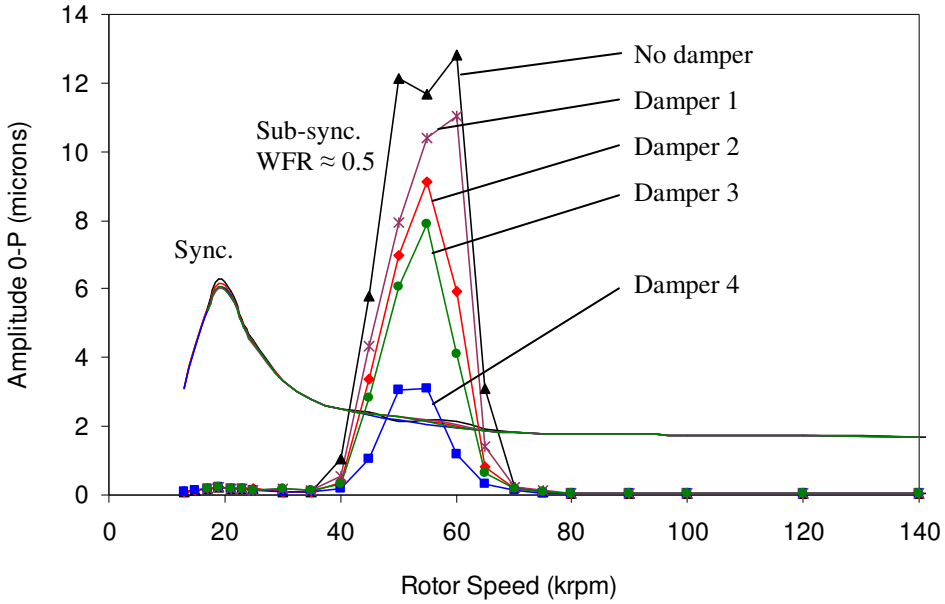

Figure VII-20: Predicted vertical responses for rotor-bearing system with split offset (0.25 mil) in bearing – nominal clearance 30 micron. Dampers added ignoring stiffness contribution.

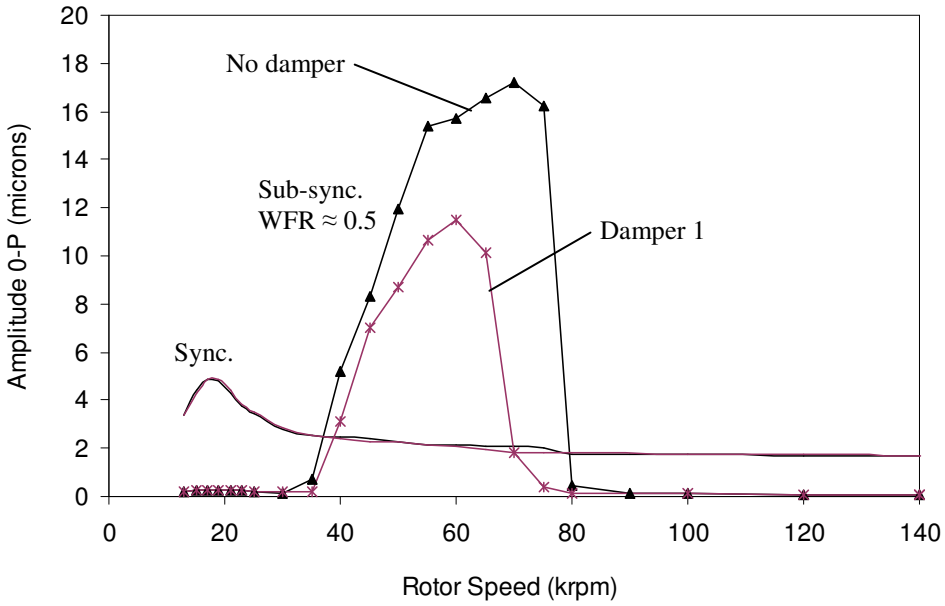

Figure VII-21: Predicted vertical responses for rotor-bearing system with split offset (0.125 mil) in bearing – nominal clearance 32 micron.

Discussion and concluding remarks

Realistically, the simulation results perhaps make more sense than the experimental results. Considering relative sizes, the 1-3 mil ≈ 25-75 micron shims are extremely large compared to approximate nominal clearances of 30-35 microns measured in the bearings. The fact that the rotor-bearing system was stable at all under these conditions was quite surprising. The simulations, of course, are totally idealized models of the bearing: they assume cylindrical motion (reasonable considering measured phase angles in the experiments), uniform bearing geometry in the axial direction, and perfect bearing alignment. Other elements not taken into account are effects of the turbines, and thrust bearings. In the model under ideal conditions, the smaller shims (0.125-0.25 mil ≈ 3-6 micron) that caused subsynchronous vibrations are more easily justified in an intuitive sense. It is believed that the two largest points of uncertainty in the experiments are the clearance of the bearings, and the true level of alignment of the bearings in the rig. Recall that measurements of the bearing clearances showed large variations in the axial direction, and the reported clearances had to reflect the level of this variation. Also, although much care was taken to perfectly align the bearings with the rotor in the housings by the method described in Appendix A, the quality of the final alignment is certainly not truly known. In fact, the alignment procedure was based on the assumption of relatively uniform clearances in the axial direction and at the location of the pad pivots, so alignment was related to the clearance. The presence of misalignments could tend to impose eccentricity or loading effect of the

rotor in the bearings which may explain greater stability than predicted by orbit simulations.

The dampers had a negligible effect on suppressing subsynchronous vibrations at midrange speeds in the experiments, but simulations showed a significant improvement (although subsynchronous vibrations were never shown to be eliminated), especially due to the stiffness contribution of the damper. The damper stiffness was estimated from the measured increase in pad natural frequency when the damper was installed in the bearing. Thus, the as-installed damper stiffness was measured at a frequency on the level of 5 kHz (equivalent to synchronous pad motion at 300 krpm). This may not be realistic, as stiffness may be expected to reduce at lower frequency and would explain why the effect is not seen for rotor speeds at around 20 krpm ≈ 300 Hz, while they are noticeable at around 50 krpm ≈ 800 Hz.

As a point of comment, adding shims to the bearings was shown to have the negative effect of allowing subsynchronous rotor vibrations in middle regions of the operating range, but it also had the positive effect of decreasing the drag on the rotor due to larger film thickness. Figure VII-22 shows the rotor speed vs. time for the test with the 3 mil shim. The trend of the data shows an exponential decay of the rotor's speed due to air drag effects, and a curve fit indicates an exponential time constant of $1/(0.0166\ s^{-1}) = 60.2$ s. Similar calculations were made for 2 mil, 1 mil, and no shim cases, resulting in time constants of 54.3, 48.8, and 44.2 s, respectively. Note that the exponential time constant increases linearly as the shim thicknesses is increased (Figure

VII-23). As a comparison, hybrid FPTPGBs tested by San Andrés [6] for a similar sized rig reported time constants ranging from 57-63 s.

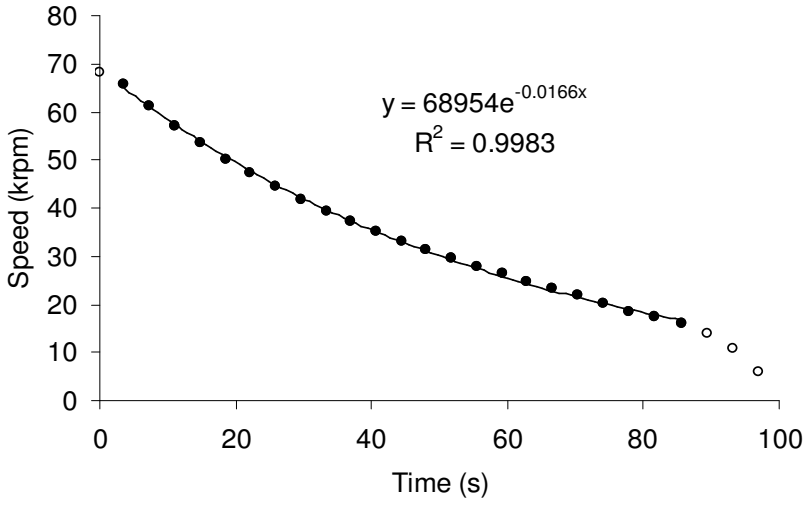

Figure VII-22: Coast down speed vs. time for test rig Setup #2 and 3 mil shim. Filled-in symbols represent data points used for curve fit.

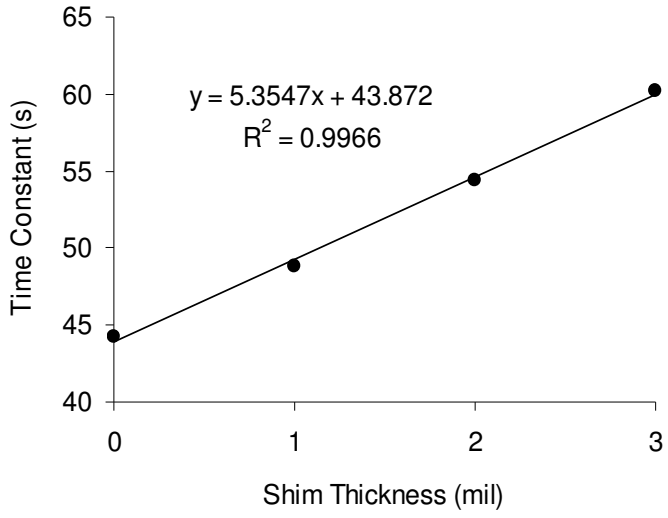

Figure VII-23: Summary of exponential time constant vs. shim thickness for coast down tests with test rig Setup #2. Increasing shim thickness linearly increases the exponential time constant due to reduced friction drag of the air film.

Closure on Experimental Studies

Initial testing was performed with test rig Setup #1, and the rotor-bearing system was demonstrated to be capable of running beyond 120 krpm without subsynchronous vibrations. The source of large 2X vibrations is unknown, but possibly related to misalignments in the bearings, turbine housings, or thrust bearings as well as rotor out-of-roundness. The source of 6X vibrations was identified to be caused by the six-bladed turbines on the rotor. Slight modification of the test rig was required due to a failure of one of the bearings during a high speed test, and the resulting Setup #2 was still demonstrated to be stable above the maximum attempted speed beyond 105 krpm. Imbalance response testing confirmed that the bearings behaved linearly with imbalance at high speeds, and predictions with the orbit simulation model showed reasonable agreement when compared to the data from the baseline subtraction for added imbalance of 288 mg-mm.

Testing with dampers behind the pads of the test bearings showed only minor improvements to the intentionally-destabilized system. Gas film thickness in the vertical direction was increased by using shims between the upper and lower halves of the bearings, and regions of approximately half-synchronous vibrations were introduced around 20-25 krpm. After this region, shim sizes of 1-2 mil did not have subsynchronous vibrations up to the maximum attempted speed above 105 krpm, while a shim size of 3 mil introduced another region of subsynchronous vibration at around 43 krpm. For the 3 mil shim case, dampers were applied behind the pads of the bearings, and the upper region of subsynchronous vibrations was delayed to after 50 krpm;

however, virtually no effect was shown on the midrange subsynchronous vibrations. Orbit simulations were able to predict the occurrence of midrange vibrations at half-synchronous whirl by increasing nominal clearance and/or adding shims to increase vertical clearance, and these vibrations were shown to be self-stabilized due to the rotor's centrifugal growth. Simulation of the case of added shims and behind-pad dampers showed considerable improvement on suppressing midrange subsynchronous rotor vibrations, notably due to a significant effect from the increase in pad radial stiffness. As an explanation, it was presented that the stiffness of the dampers was only determined at a relatively high frequency, and it was noted that the actual stiffness contribution of the damper at the lower frequencies where subsynchronous vibrations were present may have been much lower. While the shims had the negative effect of inducing subsynchronous vibrations to the system, the coast down time constants were shown to increase linearly with the amount of vertical clearance added by the shims.

The fact that the rotor-bearing system was stable at all when shims of 1-3 mil were added is surprising since 3 mil is over two times larger than the estimated nominal bearing clearance. The orbit simulation, which models an ideal, perfectly aligned system with uniform axial bearing geometry, was only able to tolerate shim sizes on the order of 10% of nominal clearance. It is believed that the two largest points of uncertainty in the experiments are the clearance of the bearings which have variation in the axial direction, and the true level of alignment of the bearings in the rig. The presence of misalignments could possibly impose eccentricity or loading effect of the rotor in the bearings which could explain much greater stability of the test rig than predicted by orbit simulations.

CHAPTER VIII

SIMULATION STUDY OF FPTPGBs AND FPTPGB-Cs WITH A CORRUGATED BUMP FOIL SUPPORT

The orbit simulation had been employed in the previous chapter to predict behaviors of a fixed FPTPGB-C with comparisons to experiments. The predictions were reasonable, and noted shortcomings were related to the uncertainty of bearing clearances and the true level of alignment in the test rig. The model developed for the orbit simulation has the ability to simulate the configuration where the bearing shell is also free to move, and this chapter presents the results of a parameter study that compares the effect of bearing shell mass and support stiffness, two controllable features in the design of such a configuration. Bearing shell mass (mass of total bearing, excluding masses of pads) can be controlled by changing the outer diameter of the bearing, the axial length of the bearing shell, and by eliminating other unnecessary material left after the wire-EDM process. The bearing shell support considered for the application is a corrugated bump foil as used in foil gas bearings; stiffness can be controlled by varying foil thickness and bump height, radius, and pitch. A structural stiffness model for the bump foil has been used in the literature for bump foils [19, 26, 38] and is adopted in this case.

The simulations in this study consider a hollow rotor with parameters summarized in Table VIII-1. The first case simulates the bearing without radial compliance (i.e. $k_\delta \to \infty$), and the second case simulates the bearing with radial

compliance and k_δ = 1e7 N/m [6]. Bearing shell support stiffnesses considered are k_{BS} = 5e6, 1e7, and 5e7 N/m, and bearing shell masses are m_{BS} = 0.1, 0.2, and 0.3 kg. The bearing shell support stiffnesses used are larger than in typical foil bearings but were chosen to be more comparable to the stiffnesses found within the gas film (~1e6-1e7 N/m). The structural loss factor of the support used for the simulations is 0.25, similar to values from foil bearing papers [16, 19, 26]. The masses are also less than for the test bearings in the experimental study (~0.5 kg); however, it can be justified that the bulk of the bearing shell could be reduced in several areas.

Table VIII-1: Rotor-bearing system parameters.

Rotor Parameters		
Diameter, $2R$	28.6	mm
Wall thickness, $R - R_i$	3	mm
Mass, m_R	0.4	kg
Imbalance level	150	mg-mm
Bearing Parameters		
Number of pads	4	
Pad mass, m_p	0.016	kg
Pad tilting moment of inertia, i_p	1.0×10^{-6}	kg-m^2
Start angle of first pad	5	degree
Pad arc length	80	degree
Pivot offset	0.7	
Preload, $R_p = r_p / C$	0.5	
Pad tilting stiffness, k_ϕ	20	N-m/rad
Bearing length, L	33.2	mm
Nominal clearance, C	35	μm

[6] Hereon, shorter notation of 'AeB' is equivalent to ' $A\times10^B$ ', etc.

Bearings without Radial Compliance

Figure VIII-1 and Figure VIII-2 present the synchronous amplitude responses to imbalance (both rotor and bearing shell vibrations) from orbit simulations for the rotor-bearing of Table VIII-1 and no radial compliance. Figure VIII-1 shows the effect of bearing shell mass (m_{BS} = 0.1-0.3 kg with k_{BS} = 1e7 N/m), while Figure VIII-2 shows the effect of damper stiffness (k_{BS} = 5e6-5e7 N/m with m_{BS} = 0.2 kg). In both comparisons, maximum operating speed is limited to approximately 130 krpm, which is the limit allowed by bearing clearance due to centrifugal growth of the rotor. Note the appearance of at least two critical speeds[7] are observed for each of the responses in both cases. Three critical speed peaks are most prominently displayed for the intermediate parameters (m_{BS} = 0.2 kg and k_{BS} = 1e7 N/m), and the shape of the major resonance peak around 100 krpm for m_{BS} = 0.1 kg in Figure VIII-1 appears to be the coalescing of two separate critical speeds. Furthermore, the maximum speed for this configuration is only shown up to 110 krpm. This is due to the system being excited by the natural frequency associated with the upper critical speed as shown in Figure VIII-3. Note that this natural frequency is supersynchronous and exists from about 113 krpm to below 125 krpm, where it is eventually suppressed.

[7] The term critical speed is used here to describe the speed where a local-maximum amplitude exists in the imbalance response plot.

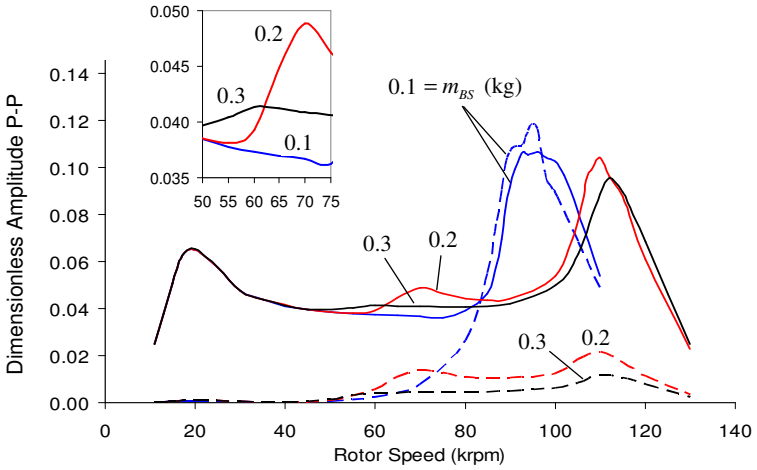

Figure VIII-1: **Synchronous imbalance responses – bearings without radial compliance. Rotor response (solid line) and bearing shell response (dotted line). Fixed bearing shell support stiffness (1e7 N/m) and varying bearing shell mass (0.1, 0.2, and 0.3 kg). Inset shows zoomed region by middle critical speeds.**

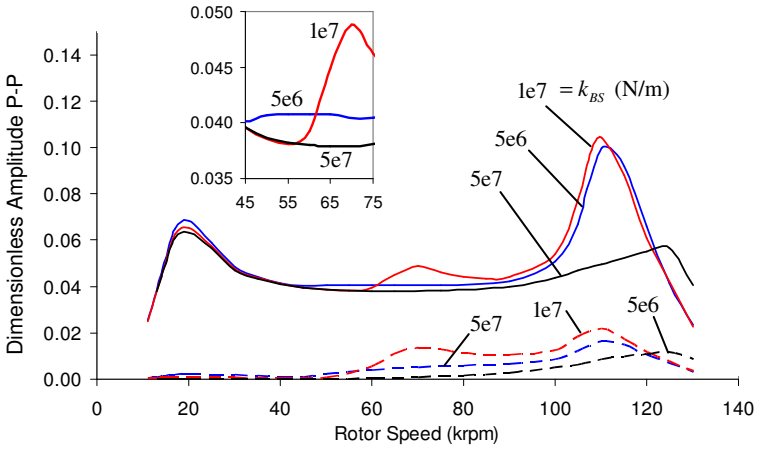

Figure VIII-2: **Synchronous imbalance responses – bearings without radial compliance. Rotor response (solid line) and bearing shell response (dotted line). Fixed bearing shell mass (0.2 kg) and varying bearing shell support stiffness (0.5e7, 1e7, and 5e7 N/m). Inset shows zoomed region by middle critical speeds.**

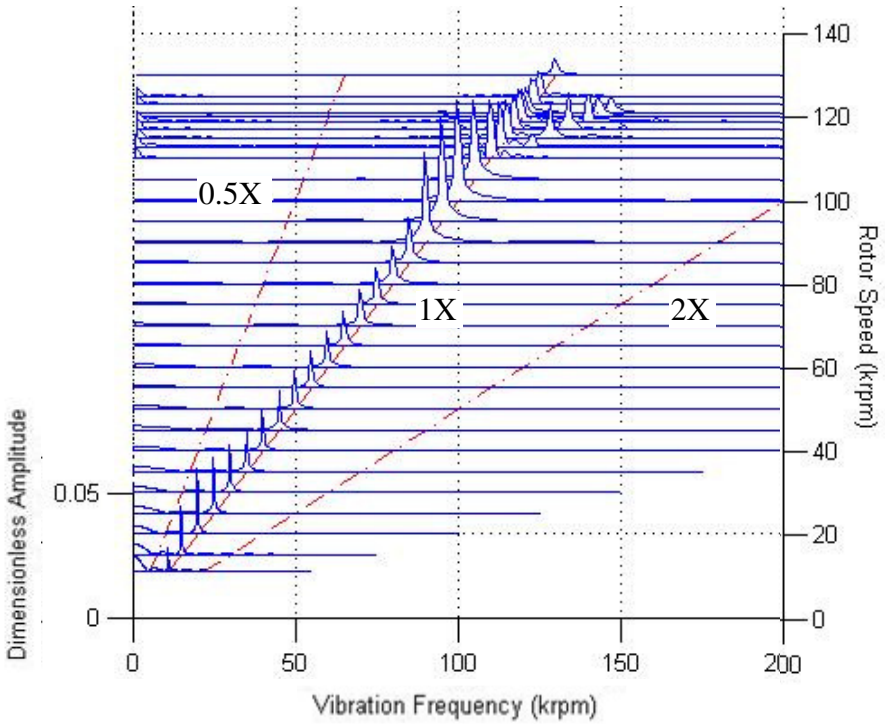

Figure VIII-3: Cascade plot of rotor vibrations for simulated case of bearings without radial compliance, bearing shell mass of 0.1 kg, and bearing shell support stiffness of 1e7 N/m. System excited by supersynchronous natural frequency associated with critical speed at ~100 krpm.

The first critical speed is certainly the critical speed due to the natural frequency of the rotor since bearing shell vibrations are negligible below 40 krpm, which is also the reason that the rotor critical speed changes very little with different bearing shell parameters. The other critical speeds are due to the effect of the bearing shell but cannot be easily explained by only using the orbit simulation results, thus requiring a complimentary analysis.

Description of linear analysis method

Recently, Kim [26] and Kim et al. [27] looked at comparisons of natural frequencies from orbit simulations to the natural frequencies computed by a method using frequency-dependent, linearized bearing impedance coefficients. The findings of [27] were that natural frequencies at a certain rotor speed ω could be estimated by finding where so-called modal stiffness (k_{modal}) vs. excitation frequency ratio ($\nu = \Omega / \omega$) curves are intersected by the curve of $m_R \Omega^2 = m_R \omega^2 \nu^2$ vs. ν – the intersection point occurs at $\nu = \nu_{nat.} = \Omega_{nat.} / \omega$. In [26, 27], k_{modal} is the real part of the eigenvalues of the frequency-dependent bearing impedance matrix.

Following the method of Kim et al. [27], the homogeneous equation of motion of the rotor can be written as

$$[M_R]\begin{Bmatrix} \ddot{\tilde{x}}_R \\ \ddot{\tilde{y}}_R \end{Bmatrix} + [Z_R]\begin{Bmatrix} \tilde{x}_R - \tilde{x}_{BS} \\ \tilde{y}_R - \tilde{y}_{BS} \end{Bmatrix} = \{0\}. \qquad \text{(VIII-1)}$$

Here, $[M_R] = m_R [I_2]$ and $[Z_R]$ is the frequency-dependent bearing impedance matrix calculated in the perturbation simulation (i.e. Equation (V-26)). Similarly, the bearing shell has the homogeneous equation of motion of

$$[M_{BS}]\begin{Bmatrix} \ddot{\tilde{x}}_{BS} \\ \ddot{\tilde{y}}_{BS} \end{Bmatrix} + [Z_{BS}]\begin{Bmatrix} \tilde{x}_{BS} \\ \tilde{y}_{BS} \end{Bmatrix} - [Z_R]\begin{Bmatrix} \tilde{x}_R - \tilde{x}_{BS} \\ \tilde{y}_R - \tilde{y}_{BS} \end{Bmatrix} = \{0\}. \qquad \text{(VIII-2)}$$

Here, $[M_{BS}] = m_{BS}[I_2]$ and $[Z_{BS}] = k_{BS}(1+i\eta)[I_2]$, where η is the loss factor of the bump foil structural model. Equations (VIII-1) and (VIII-2) are combined for the two-mass system with $\{\tilde{x}\} = \{\tilde{x}_R, \tilde{y}_R, \tilde{x}_{BS}, \tilde{y}_{BS}\}^T$:

$$[M']\{\ddot{\tilde{x}}\} + [Z']\{\tilde{x}\} = \{0\} \tag{VIII-3}$$

$$[M'] = \begin{bmatrix} [M_R] & [0] \\ [0] & [M_{BS}] \end{bmatrix} \text{ and } [Z'] = \begin{bmatrix} [Z_R] & [-Z_R] \\ [-Z_R] & [Z_R + Z_{BS}] \end{bmatrix} \tag{VIII-4}$$

Denote the eigenvalues of $[M']^{-1}[Z']$ as λ_K with corresponding eigenvectors $\{\psi_K\} = \{\bar{x}_{R,K}, \bar{y}_{R,K}, \bar{x}_{BS,K}, \bar{y}_{BS,K}\}^T$. Consider the motions of the rotor or bearing shell corresponding to the respective pair of eigenvector components $(\bar{x}, \bar{y}) = (\bar{x}_{R,K}, \bar{y}_{R,K})$ or $(\bar{x}_{BS,K}, \bar{y}_{BS,K})$, and define $\bar{c} = [\mathrm{Re}(\bar{y})\,\mathrm{Im}(\bar{x}) - \mathrm{Re}(\bar{x})\,\mathrm{Im}(\bar{y})]$. Then, it can be shown that forward whirling exists when $\bar{c} > 0$, and negative whirling exists when $\bar{c} < 0$. From the orbit simulations, the rotor and bearing shell are observed to be forward-whirling, thus, the following analysis only considers the eigenvalues that correspond with the forward whirling case.

Again, following Kim et al. [27], modal stiffness[8] is $k_{\text{modal}} = \mathrm{Re}(\lambda_K)$. Then, a natural frequency is defined when k_{modal} vs. ν intersects $\nu^2\omega^2$ vs. ν, or alternatively,

[8] Note that eigenvalues are calculated from the impedance matrix pre-multiplied by the mass matrix, thus units of 'modal stiffness' will be actually have units of stiffness divided by mass, e.g. N/kg-m or $(\text{rad/s})^2$.

when $f_K(\nu) = k_{\text{modal}} - \nu^2\omega^2 = 0$. In this way, for a given rotor speed ω and a range of ν, natural frequencies are defined as $\nu_{nat.}\omega$ where $\nu = \nu_{nat.}$ is a solution of $f_K(\nu) = 0$. For this study, $\nu = 0.2, 0.4, 0.6, ..., 4.0$ was used, and crossing points are determined by interpolation. Figure VIII-4 shows how this method is employed: At each rotor speed, bearing impedance matrices and forward-whirl eigenvalues are calculated for a range of frequency ratios, and the natural frequencies are defined when $f_K(\nu) = 0$. For example, the natural frequencies calculated at 40 krpm (Figure VIII-4(b)) are 0.58×40 krpm = 23.2 krpm and 3.98×40 krpm = 159.2 krpm.

Figure VIII-5 and Figure VIII-6 plot the calculated natural frequencies vs. rotor speed for bearings without radial compliance and comparisons of different bearing shell masses and bearing shell support stiffnesses, respectively. In both figures, natural frequencies associated with the rotor appear to be the lower set of curves, while natural frequencies associated with the bearing shell appear to be the upper set of curves. The diagonal line from the origin is the rotor speed line (i.e. 1:1), giving reference to when the rotor is traversing one of its natural frequencies. Within the range of frequency ratios tested, i.e. 0.2-4.0, zero-crossing points of $f_K(\nu)$ for the upper curves were not observed in some cases at low rotor speeds (e.g. Figure VIII-4(a)), which is the reason for the truncated curves as illustrated in Figure VIII-5.

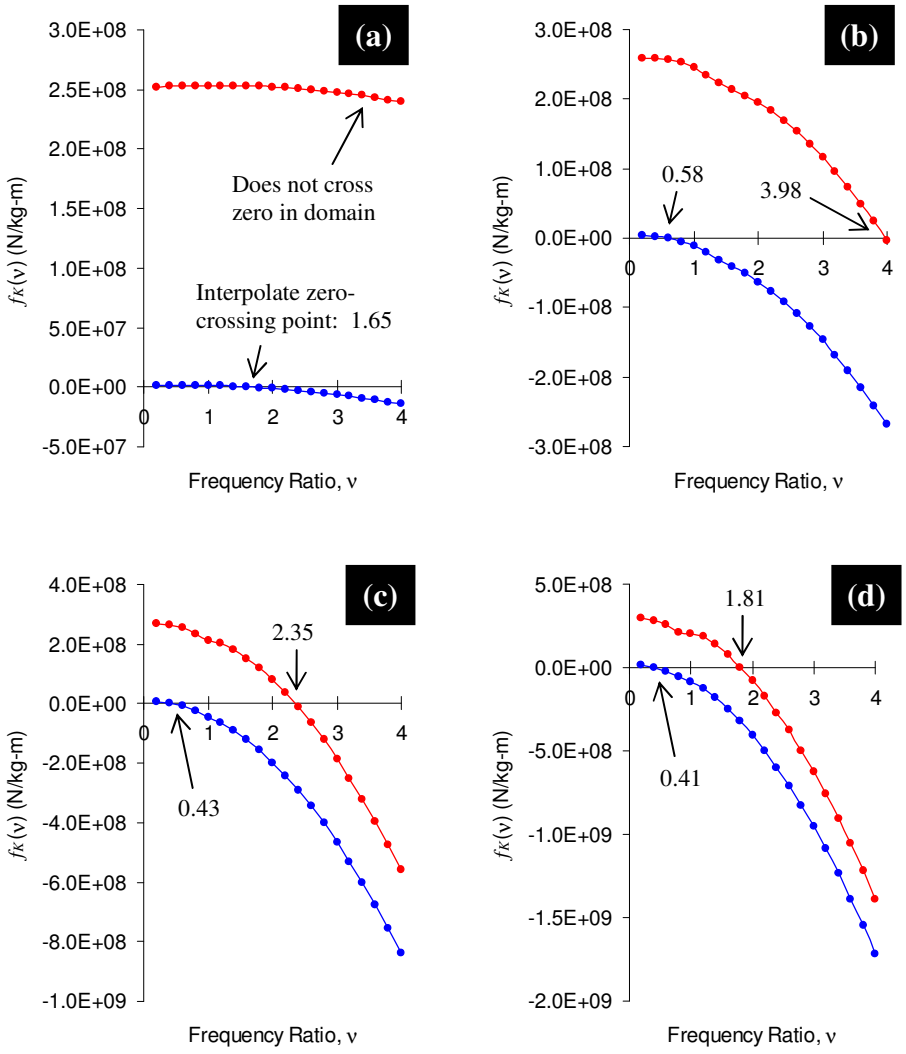

Figure VIII-4: **Plots of $f_K(\nu)$ vs. frequency ratio to determine zero-crossing points. Cases shown for bearing without radial compliance; 0.2 kg and 5e7 N/m bearing shell mass and support stiffness; and selected rotor speeds of (a) 10 krpm, (b) 40 krpm, (c) 70 krpm, and (d) 100 krpm.**

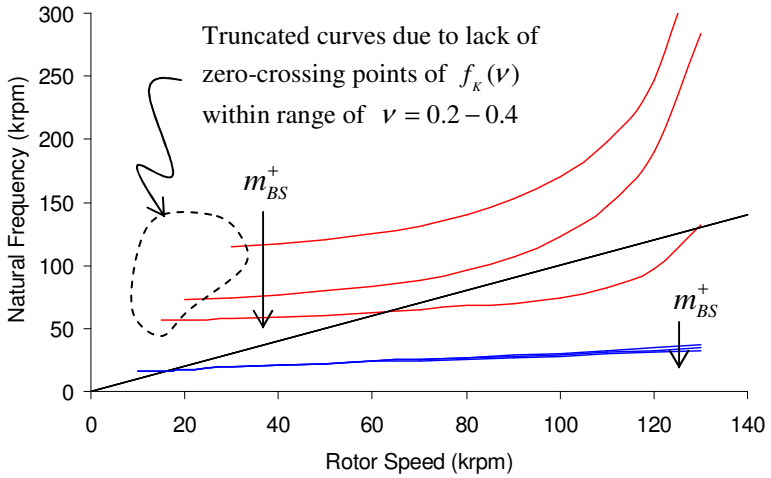

Figure VIII-5: Predicted natural frequencies for bearing without radial compliance and fixed bearing support stiffness (1e7 N/m); comparisons with different bearing shell masses (0.1, 0.2, and 0.3 kg).

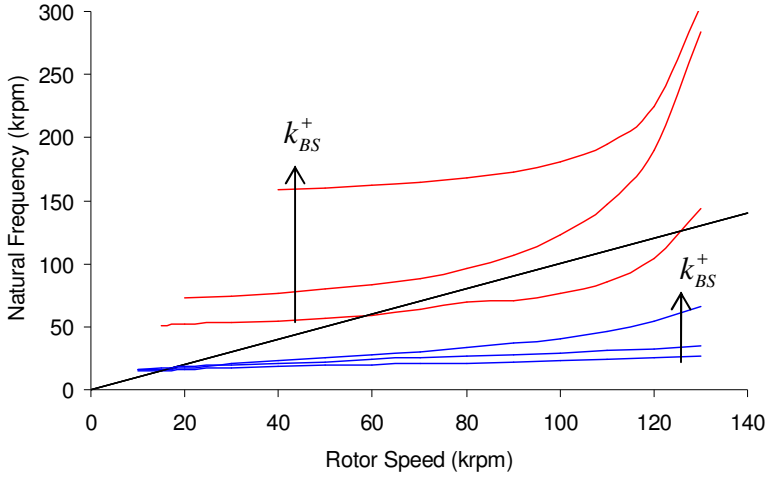

Figure VIII-6: Predicted natural frequencies for bearing without radial compliance and fixed bearing shell mass (0.2 kg); comparisons with different bearing shell masses (5e6, 1e7, and 5e7 N/m).

Discussion on first critical speed due to rotor natural frequency

At this time, orbit simulations are compared to the results of the linear analysis method described above. Notice that comparable parameters are for the variation of bearing shell mass (Figure VIII-1 and Figure VIII-5) and bearing shell support stiffness (Figure VIII-2 and Figure VIII-6). The natural frequency contours associated with the rotor are relatively constant with bearing shell mass, although decreasing slightly (Figure VIII-5). For comparison, the rotor speed crosses the natural frequency contours in Figure VIII-5 at about 17 krpm, which is slightly less than the first critical speed in Figure VIII-1 of 20 krpm. Similarly, the rotor speed crosses the rotor natural frequency contours from approximately 16-18 krpm, increasing with bearing shell support stiffness (Figure VIII-6), and are less than the critical speeds in Figure VIII-2 occurring at approximately 20 krpm. Conclusion 1: The natural frequencies of the rotor are less than the critical speeds from the orbit simulation – this is in agreement with the phenomenon observed in typical imbalance response of a rotor. Conclusion 2: The rotor natural frequencies change very little with bearing shell mass; however, the tendency shows a slight decrease as bearing shell mass increases. This is a typical result for a simple two-mass system as shown in Figure VIII-7. Note that the slope of the natural frequency contours in Figure VIII-7(a) are always negative as the lower mass (analogous to bearing shell) is increasing. Conclusion 3: The rotor natural frequencies increase as bearing shell support stiffness increases. In comparison to the simple two-mass system in Figure VIII-7(b), this is in agreement since the natural frequency of the upper mass (analogous

to rotor) increases and asymptotically approaches the natural frequency of $\sqrt{k_2/m_2}=1$ as the lower mass becomes rigid to ground.

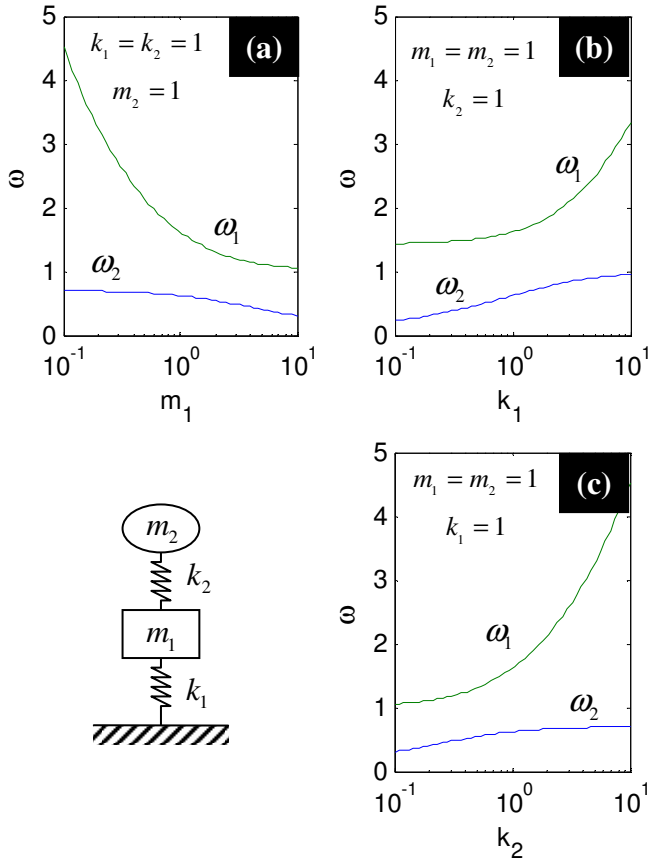

Figure VIII-7: **Trends of natural frequencies for a simple 2-mass system. Mass-1 and stiffness-1 are analogous to the bearing shell mass and support stiffness. Mass-2 and stiffness-2 are analogous to the rotor mass and gas film stiffness. Analogous comparisons show effects of increasing (a) bearing shell mass, (b) bearing shell support stiffness, and (c) gas film stiffness.**

Discussion on higher critical speeds

The analysis method used by Kim et al. [27] to predict rotor natural frequencies from linearized bearing impedance coefficients gives very reasonable results when compared to the critical speeds associated with the rotor found in the orbit simulations. Now, higher critical speeds from the orbit simulations are compared with the higher natural frequencies from the same eigenvalue analysis. Recall that the orbit simulations in Figure VIII-1 and Figure VIII-2 showed multiple critical speeds above the initial critical speed at 20 krpm. For a two-mass system, one would expect to observe only two natural frequencies. However, in the present case, stiffening of the gas film as speed increases (due to reduction in clearance by rotor centrifugal growth) subsequently increases the natural frequencies (e.g. the simple two-mass model in Figure VIII-7(c)). This causes the upper natural frequency contours in Figure VIII-5 and Figure VIII-6 (associated with bearing shell) to increase significantly at the high end of the speed range. Note that this key effect can cause the natural frequency contour to cross the rotor speed line twice, which explains more than two critical speeds for a two-mass system.

The general trends of the bearing shell natural frequency contours are as follows: increasing bearing shell mass decreases its natural frequency, and increasing bearing shell support stiffness increases its natural frequency. Both of these characteristics are similarly understood when comparing to the simple two-mass system in Figure VIII-7. In addition to this fundamental observation, the shape of the natural frequency contours allows for another useful insight as illustrated in Figure VIII-8. Notice that while

increasing bearing shell mass lowers the natural frequency contour and decreases the first crossing point (i.e. natural frequency), the second crossing point increases (a similar comparison may be made for the effect of bearing shell support stiffness). Certainly, both trends are presented by the orbit simulation as the middle critical speeds are decreasing and upper critical speeds are increasing with bearing shell mass in Figure VIII-1. Since generally $\omega_{nat.} \propto 1/\sqrt{m}$, one would immediately expect bearing shell natural frequency to decrease as bearing shell mass is increased (i.e. the lower crossing point in Figure VIII-8); however, one may not expect the opposite case (i.e. the upper crossing point in Figure VIII-8). In fact, the middle critical speeds from Figure VIII-1 are observed as ~100[9], ~70, and ~60 krpm for m_{BS} = 0.1, 0.2, and 0.3 kg, respectively, which corresponds with $\omega_{nat.,mid} \propto 1/\sqrt{m_{BS}}$. Furthermore, recall that the higher critical speed for the configuration with m_{BS} = 0.1 in Figure VIII-1 was observed to be excited by a supersynchronous natural frequency after passing the highest critical speed (Figure VIII-3), which is also consistent with the results of the linear analysis. Indeed, the predicted trends of the natural frequency contours provide a very reasonable explanation for the phenomenon seen in the orbit simulation.

[9] For bearing shell mass case of 0.1 kg in Figure VIII-1, it was noted previously that the higher speed resonance region appeared to be the coalescing of at least two critical speeds. Since the trend was observed that the middle (upper) critical speed increases (decreases) as mass increases, it is reasonably assumed that the middle and upper critical speeds for the 0.1 kg case are coinciding at the same speed.

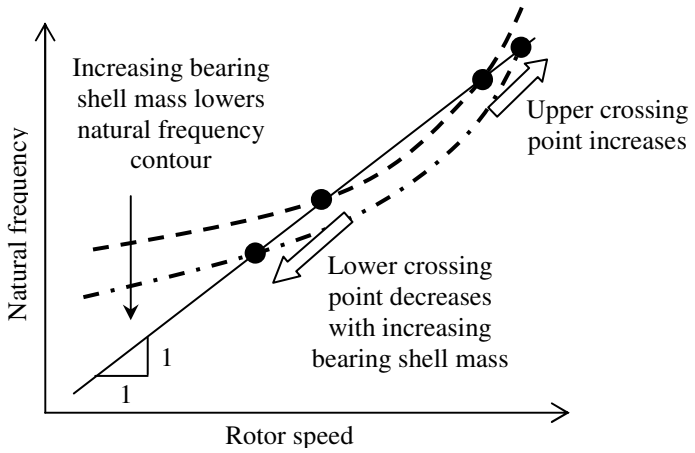

Figure VIII-8: Effect of increasing bearing shell mass on multiple crossing points for natural frequency contours.

The actual predictions of upper critical speeds are only present for the lowest curves in Figure VIII-5 and Figure VIII-6 which does not allow for the direct comparison with all cases of orbit simulations in Figure VIII-1 and Figure VIII-2. Nevertheless, for m_{BS} = 0.3 kg and k_{BS} = 1e7 N/m, natural frequency predictions of 63 and 129 krpm (Figure VIII-5) are slightly higher than critical speeds of approximately 60 and 115 krpm from orbit simulations (Figure VIII-1). Similarly, for m_{BS} = 0.2 kg and k_{BS} = 5e6 N/m, natural frequency predictions of 60 and 126 krpm (Figure VIII-6) are slightly higher than critical speeds of approximately 55 and 110 krpm from orbit simulations (Figure VIII-2).

Concluding remarks

The fact that the natural frequency contours calculated by the linear analysis used by Kim et al. [27] agree with many fundamental (i.e. intuitive) observations on the characteristics of the present model gives confidence to the other insights that it provides. Namely, the prediction of multiple crossing points due to steep curvature of the bearing shell natural frequency contours compliments the nonlinear orbit simulation in that it reasonably explains the presence and behavior of the higher critical speeds due to changes in bearing shell mass and support stiffness. The linear analysis is able to identify the natural frequencies of the rotor with good agreement to critical speeds shown in orbit simulations, but the performance is less favorable in predicting the bearing shell natural frequencies in all cases presented.

The concept of surrounding a FPTPGB with a structure like a corrugated bump foil was presented (Chapter I) as mechanism that could, primarily, tolerate rotor misalignments and shock loading like foil gas bearings [11, 15, 17, 21]. These abilities were not specifically addressed in the current study (a good topic for future work), but the identification of rotor-bearing performance characteristics based on the selection of bearing shell mass and support stiffness was considered as an initial design stage. The configuration was also noted to be similar to a squeeze film damper (SFD) in the sense that it is an elastically supported fluid film bearing. San Andrés and De Santiago [29] presented as study on oil-lubricated FPTPBs with SFDs and concluded that relocation of system critical speeds (from imbalance response tests) was noted as a benefit of incorporating SFDs. However, by introducing the SFDs, the additional resonance of the

base became present. There were no comments on how relocation of the rotor critical speeds at the expense of adding additional bearing support resonances should be considered in the design.

By adding the flexible bearing shell support to the FPTPGB, additional critical speeds also became present. Simulating various bearing shell masses and support stiffnesses demonstrated how these critical speeds were influenced. In the case of FPTPGBs (emphasize that pad radial compliance is not present), the performance was best for the largest bearing shell mass and the largest support stiffness. This conclusion is based on the imbalance responses shown in the orbit simulations in Figure VIII-1 and Figure VIII-2, where the criteria is taken as the condition that allows the operating range between critical speeds to be the largest.

Bearings with Radial Compliance

Figure VIII-9 and Figure VIII-10 present the synchronous amplitude responses to imbalance (both rotor and bearing shell vibrations) from orbit simulations for the rotor-bearing system of Table VIII-1. In this case the bearings have radial compliance of the pads with stiffness of k_δ = 1e7 N/m, and the maximum operating speed limited by centrifugal growth of the rotor is observed to increase from approximately 130 krpm (no radial compliance) to 180 krpm. Figure VIII-9 shows the effect of bearing shell mass (m_{BS} = 0.1-0.3 kg with k_{BS} = 1e7 N/m), while Figure VIII-10 shows the effect of bearing shell support stiffness (k_{BS} = 5e6-5e7 N/m with m_{BS} = 0.2 kg).

The only configuration displayed up to the maximum speed is for the largest stiffness in Figure VIII-10. All other configurations were excited by bearing shell and rotor natural frequencies shortly after passing the system's second critical speed. Recall that this was also observed to happen in the smallest bearing shell mass configuration in Figure VIII-1 (no radial compliance case), where the system was excited by the supersynchronous bearing shell natural frequency (Figure VIII-3). However, the present case with radial compliance has subsynchronous natural frequencies after the critical speed as indicated in Figure VIII-11. Note that the bearing shell natural frequency is excited first, then the rotor natural frequency after 85 krpm. The configuration in Figure VIII-11 is the only one that was able to suppress the non-synchronous vibrations before reaching maximum speed; all other configurations became completely unstable (unbounded amplitudes) at approximately 120 krpm.

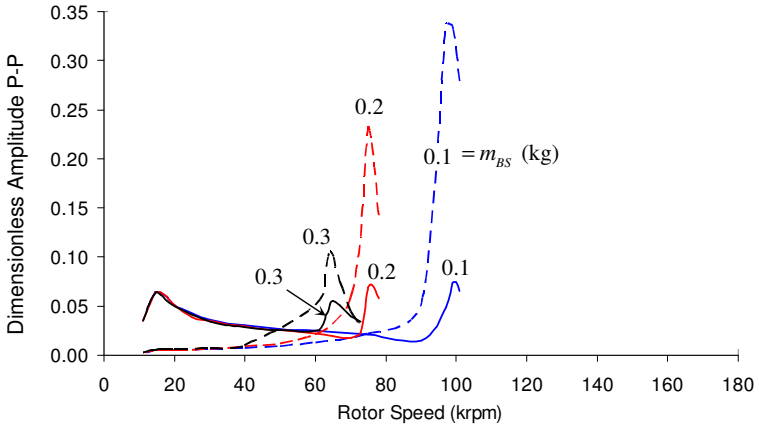

Figure VIII-9: Synchronous imbalance responses – bearings with radial compliance. Rotor response (solid line) and bearing shell response (dotted line). Fixed damper stiffness (1e7 N/m) and varying bearing shell mass (0.1, 0.2, and 0.3 kg).

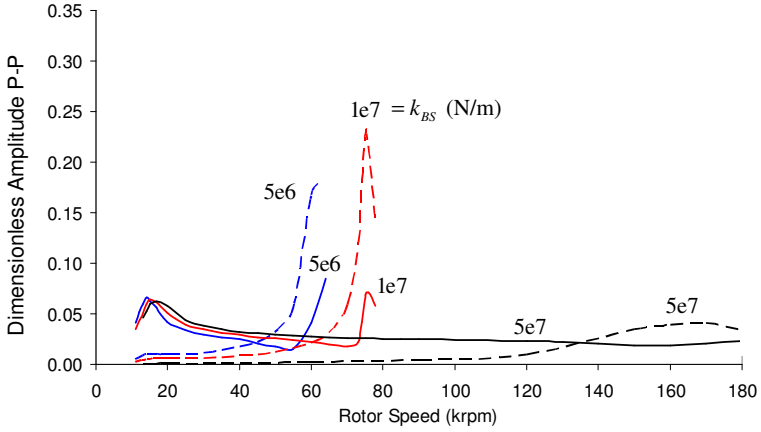

Figure VIII-10: Synchronous imbalance responses – bearings with radial compliance. Rotor response (solid line) and bearing shell response (dotted line). Fixed bearing shell mass (0.2 kg) and varying damper stiffness (0.5e7, 1e7, and 5e7 N/m).

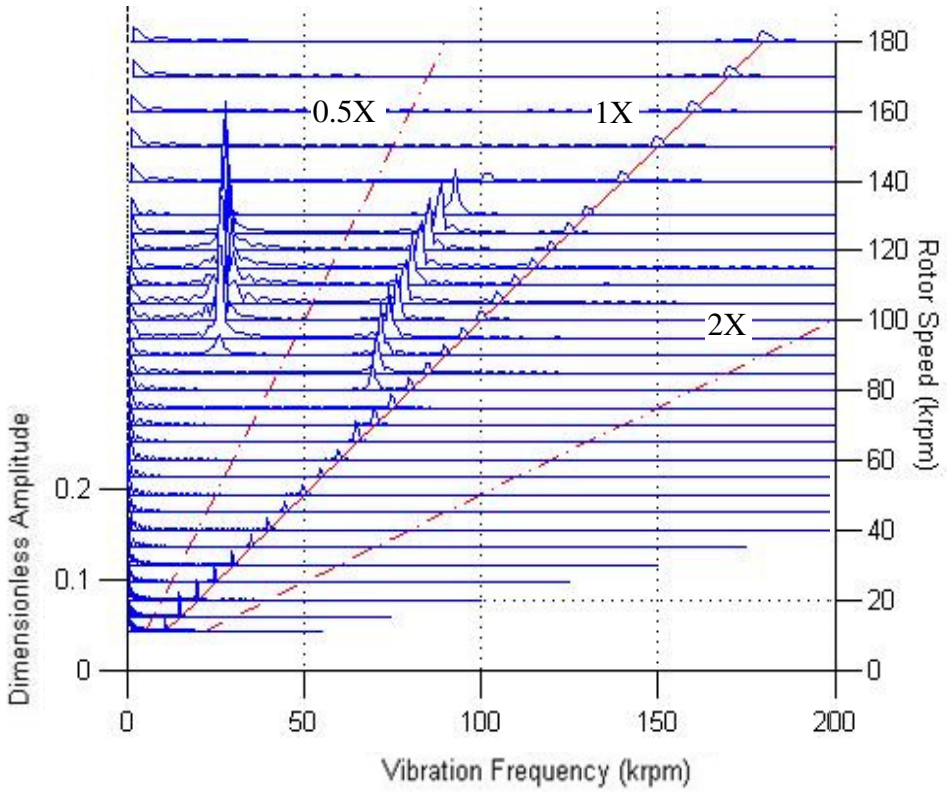

Figure VIII-11: Cascade plot of rotor vibrations for simulated case of bearings with radial compliance, bearing shell mass of 0.3 kg, and bearing shell support stiffness of 1e7 N/m. System excited by subsynchronous natural frequencies of rotor and bearing shell which are suppressed after 140 krpm.

The same linear analysis used in the previous section is now applied to the present case. Figure VII-12 and Figure VIII-13 present the calculated natural frequencies vs. rotor speed for bearings with radial compliance and comparisons of different bearing shell masses and bearing shell support stiffnesses, respectively. The peculiar behavior of the highest contour in Figure VIII-12 (circled region) comes from the fact that the $f_K(\nu)$ vs. ν curves have a curvature that causes the zero-crossing frequency ratio, i.e. $\nu_{nat.}$, to decrease abruptly between 145 and 150 krpm as shown in Figure VIII-14. Although the $f_K(\nu)$ vs. ν curves in Figure VIII-14 appear to be "smooth", the result that makes a sharp drop in the natural frequency contour does not seem to be reasonable, as it would be expected to see a much smoother transition as displayed by the other natural frequency contours.

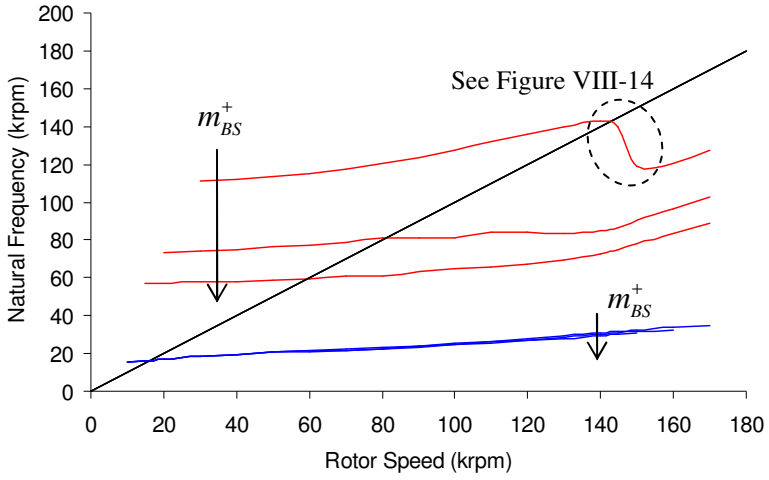

Figure VIII-12: Predicted natural frequencies for bearing with radial compliance and fixed bearing support stiffness (1e7 N/m); comparisons with different bearing shell masses (0.1, 0.2, and 0.3 kg).

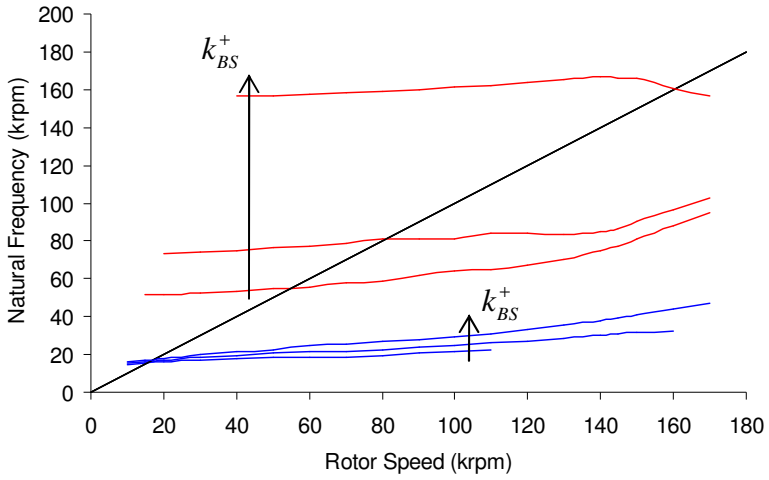

Figure VIII-13: Predicted natural frequencies for bearing with radial compliance and fixed bearing shell mass (0.2 kg); comparisons with different bearing shell masses (5e6, 1e7, and 5e7 N/m).

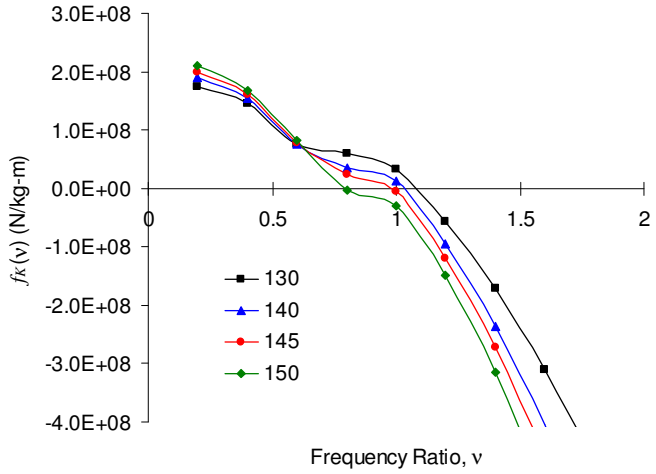

Figure VIII-14: Plots of $f_K(\nu)$ vs. frequency ratio for 0.1 kg and 1e7 N/m bearing shell mass and support stiffness at 130-150 krpm. Inflection in contour causes abrupt change in the zero-crossing frequency ratio.

The general trends of the natural frequency contours for the case of bearings with radial compliance are similar to the case without radial compliance. Namely, increasing bearing shell mass decreases its natural frequency and the natural frequency of the rotor, while increasing bearing shell support stiffness has the opposite effect. The rotor natural frequencies calculated from the linear analysis for the range of bearing shell masses are relatively constant at 16 krpm (Figure VIII-12), which is close to the critical speeds in the orbit simulations around 15 krpm, also relatively constant (Figure VIII-9). Similarly, rotor natural frequencies for the range of bearing shell stiffnesses are from 15-18 krpm (Figure VIII-13), and critical speeds are from 14-17 krpm (Figure VIII-10). In both comparisons, the natural frequency predictions from the linear analysis are slightly higher than the critical speed predictions from the orbit simulation, which is the opposite of what was observed in the previous case of bearings without radial compliance. As explained in the discussion for the previous case, it is more reasonable to expect that rotor natural frequencies would be slightly lower than critical speeds since that is the phenomenon observed in a typical imbalance response of a rotor. Therefore, the comparison between orbit simulations and the linear analysis seem to be somewhat discrepant in this regard for this case.

Both orbit simulations and linear analysis predict only one critical speed / natural frequency, which is due to the radial compliance of the pads that prevents the bearing clearances from being consumed by rotor centrifugal growth. A single bearing shell natural frequency, where the natural frequency contour transitions from supersynchronous to subsynchronous, is shown by both prediction methods and validates

a general agreement on trends. As for actual values, orbit simulations predict second critical speeds at approximately 65, 75, and 100 krpm for bearing shell masses of 0.3, 0.2, and 0.1 kg, respectively. The corresponding predictions of natural frequencies from the linear analysis are 59, 81, and 140 krpm. Notably, the comparison with the configuration for the smallest mass has the least agreeable result. Orbit simulations also predict second critical speeds at approximately 65, 75, and ~160-170 krpm for bearing shell support stiffnesses of 5e6, 1e7, and 5e7 N/m, respectively, and natural frequency predictions are 55, 81, and 160 krpm. As was noted in the previous study on bearings without radial compliance, the linear analysis method used provided general agreement on trends observed in the orbit simulations; however, agreement and the actual values is lacking. It is reasonable to say that the orbit simulation results are more reliable than the linear analysis based on the fact that the orbit simulation continuously solves the unsteady Reynolds equation and system dynamics in the time domain, preserving nonlinear effects therein (within the scope of the assumptions). The linear analysis based on impedances calculated with the assumption of infinitesimal oscillations about a fixed eccentricity may account for discrepancies when compared to a system that has finite oscillation amplitudes on the order of 20% of the bearing nominal clearance in some configurations[10].

Finally, the assessment of preferable values of bearing shell mass and bearing shell support stiffness are evaluated for the present case. Recall that analysis of the

[10] This is reference to the maximum amplitudes of the vibrations at bearing shell critical speeds, which were all observed to have rotor and bearing shell motions out of phase, which amplified actual eccentricities.

previous case for the FPTPGB favored larger bearing shell mass and larger bearing shell support stiffness. In these configurations, the operating ranges between the larger amplitude critical speeds of the imbalance response were maximized. By similar reasoning, larger bearing shell support stiffness is still favorable for the case of FPTPGB-Cs, but now choosing a smaller bearing shell mass. In the case of FPTPGB-Cs, where maximum speed is not limited by rotor centrifugal growth, the smaller bearing shell mass extends the onset speed of the bearing shell resonance peak.

The Effect of Rotor Growth and Radial Compliance on Pad Preload

This section provides a brief discussion on the effects of rotor centrifugal growth and pad radial compliance on pad preload, two prominent features noted in this work. Consider Figure VIII-15 which depicts a rotor, a deflected pad, and an un-deflected pad (i.e. no radial compliance). In the case of a pad without radial compliance, the rotor is only able to grow as large as the set bore before rotor-pad contact occurs. Moreover, as the rotor grows, it is apparent that the converging wedge effect continuously increases as the ratio of film thickness at the pad leading edge to the minimum film thickness approaches infinity. Increasing wedge effect (i.e. preload) can improve the stability of a bearing by increasing direct stiffness (Figure VIII-16), thus rotor growth can be a stabilizing mechanism, as was demonstrated in Figure VII-4. The limitation of this configuration is clearly the maximum speed that the bearing can tolerate before the gas film is reduced beyond a critical level.

In the case with radial compliance, the rotor initially expands and increases preload, causing the pad to deflect in order for the pad reaction force to balance the

increased fluid film reaction force. In this manner, the rotor is able to grow larger than the original set bore as the pad expands outward; however, in order to maintain preload, the pad deflection cannot exceed the original preload radius (Figure VIII-17).

Figure VIII-18 shows the mean local film thickness values for the bearing with radial compliance. The mean leading edge film thickness increases as mean pad tilt angle increases, but rotor growth eventually causes the mean tilt angle to neutralize and maintain positive trailing edge film thickness. The ratio of the leading edge film thickness to the minimum film thickness (at pivot) gives an indication of the converging wedge effect, i.e. preload. Note that the film thickness ratio in Figure VIII-18 drops off suddenly and tends toward unity beginning at ~150-160 krpm, which coincides with a drastic reduction in direct stiffness as shown in Figure VIII-16.

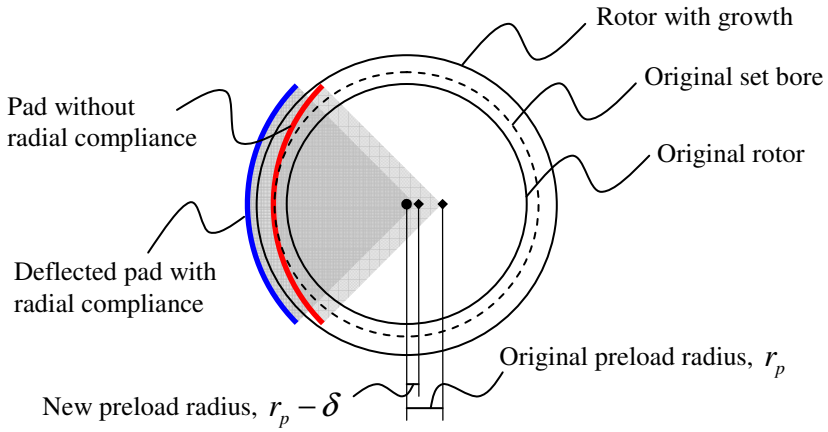

Figure VIII-15: Rotor growth increases the converging wedge effect for a bearing without radial compliance. Pad with radial compliance allows more rotor growth, but eventually leads to a loss of converging wedge.

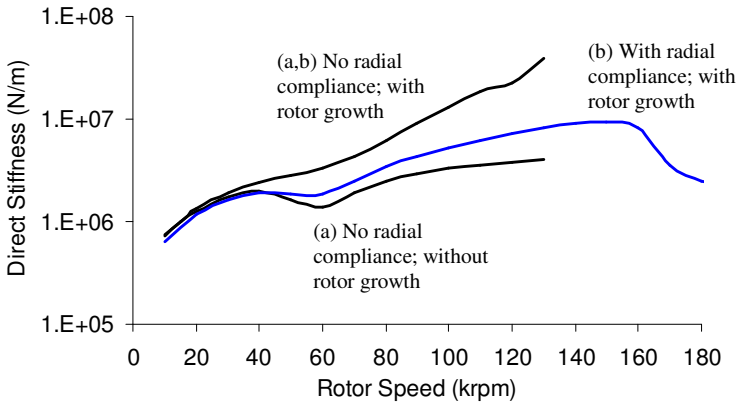

Figure VIII-16: Synchronous direct stiffness coefficients for various cases of bearings described in Table VIII-1. (a) Rotor growth significantly increases direct stiffness of bearing without radial compliance. (b) Radial compliance reduces the direct stiffness of the bearing and extends maximum operating speed.

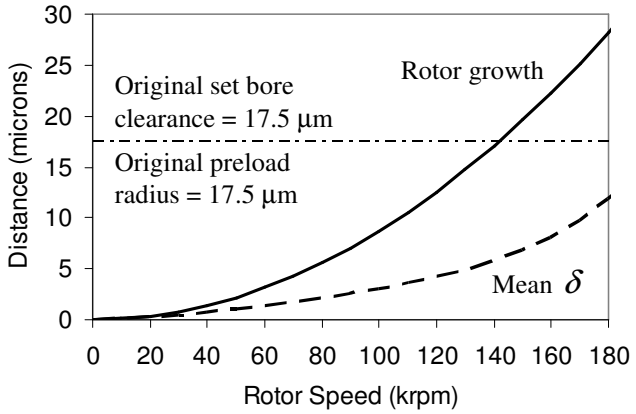

Figure VIII-17: Rotor growth and mean pad deflection vs. rotor speed for bearing with radial compliance described in Table VIII-1. Radial compliance allows rotor growth to exceed original set bore clearance, but mean pad deflection must be smaller than original preload radius to maintain converging wedge effect.

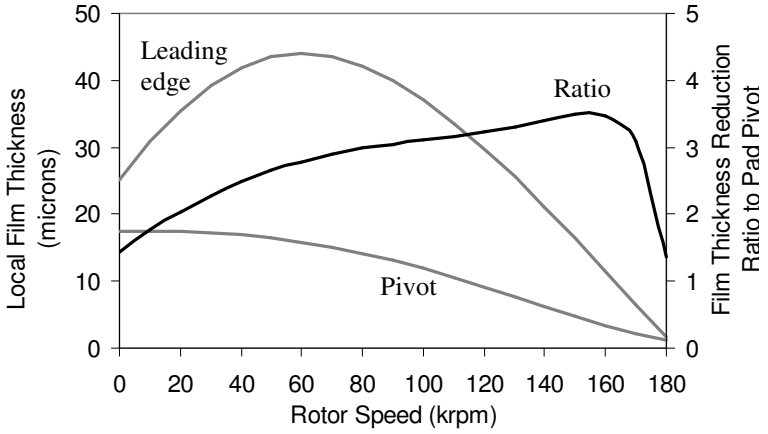

Figure VIII-18: Mean film thickness values vs. rotor speed for bearing with radial compliance described in Table VIII-1. Mean pad tilt angle increases initially to grow local film thickness at leading edge of pad, but it rotor growth causes pad angle to neutralize. Eventually film thickness reduction ratio drops to near unity, indicating loss of preload.

Closure on Simulation Studies

The orbit simulation can model the effect of a FPTPGB or FPTPGB-C supported by a flexible structure. The bearing shell support considered for the application is a corrugated bump foil as used in foil gas bearings, which uses a structural stiffness model. The simulation study focuses on the effects of bearing shell mass and bearing shell support stiffness on imbalance response performance with consideration to the design of such a system. For the case of FPTPGBs (no radial compliance), the stiffening effect caused by rotor growth typically causes the rotor-bearing system to experience three critical speeds: one for the rotor's natural frequency, and two for the bearing shell's natural frequency that can intersect the rotor speed curve multiple times.

Favorable configurations for FPTPGBs are larger bearing shell mass and larger bearing shell support stiffness.

For the case of FPTPGB-Cs (with radial compliance), stiffening effect still occurs due to rotor growth; however, the pads deflect and reduce the direct stiffness levels compared to FPTPGBs. The radial compliance allows the rotor to experience more growth (i.e., higher speed) than the no-radial compliance case, but eventually preload is lost and direct stiffness decreases abruptly. For the parameters studied, favorable configurations for FPTPGB-Cs are smaller bearing shell mass (opposite of FPTPGB case) and larger bearing shell support stiffness.

For both of the cases studied, larger bearing shell support stiffness was found to be preferable since it increased bearing shell natural frequencies. However, infinite stiffness would negate the intended purpose of flexible bearing shell supports, in particular to comply to tolerate misalignments. Thus, a compromise may need to be considered depending on the level of flexibility required to compensate for the misalignments. The focus of this study was the effect that flexible bearing shell supports have on the performance of the rotor bearing system without specifically addressing the alignment issue, but its importance recognized for proper design and implementation.

Large bearing shell mass was favored in the case of FPTPGBs, which may be a counter-intuitive conclusion in the sense that this would lower the bearing shell natural frequency. However, while the system indeed has critical speeds / natural frequencies that follow $\omega_{nat.} \propto 1/\sqrt{m_{BS}}$, the stiffening effect caused by a lack of radial compliance also introduces higher critical speeds that are of larger amplitude which increase with

bearing shell mass. Small bearing shell mass was favored in the case of FPTPGB-Cs, which is the intuitive conclusion in order to raise bearing shell critical speed. However, the limitation in this case is the minimum amount a material necessary for the bearing shell to maintain its structural integrity to support the pads, etc. Thus, as for the proper design of the bearing shell support stiffness, compromises also need to be considered to properly design the bearing shell.

CHAPTER IX

SUMMARY AND CONCLUSIONS

The present work consisted of analytical and experimental studies on flexure pivot tilting pad gas bearings with and without radial compliance (FPTPGBs and FPTPGB-Cs). The main analytical tool was a time domain orbit simulation, which employed a newly developed rotor-bearing model that allowed for the bearing to be mounted on a flexible support. The orbit simulation was used to predict rotor-bearing responses to imbalance, the presence and location of critical speeds, and nonlinear effects due to limit cycles at non-synchronous frequencies. A complimentary analysis method was an approach that used linear bearing impedance coefficients to predict system natural frequencies. Experimental studies first required the improvement of the experimental facility. This consisted of extensive refurbishment of an existing test rig that included design and manufacture of (1) a new test rotor, (2) a new air turbine drive system, and (3) a new thrust bearing system. The new thrust bearing system allowed successful operation of the test rig beyond 120 krpm. A new data acquisition system was also developed to meet the needs of high speed testing above 120 krpm with the ability to read larger than 3X frequency components.

Experimental studies included imbalance response testing and the investigation of dampers added behind the pads of the FPTPGB-Cs. Imbalance response testing verified that the rotor-bearing system behaved linearly in the region above the critical speed, and orbit simulations could predict the response to a calibrated imbalance with

notable agreement. Shims were added to the test bearings which increased the gas film in the vertical direction, inducing subsynchronous vibrations below 60 krpm. Shims of 1-2 mil only induced subsynchronous vibrations from ~20-25 krpm and remained stable beyond 100 krpm, while a shim of 3 mil induced subsynchronous vibrations from ~20-25 krpm and also from 43 krpm. Orbit simulations predicted this phenomenon due to excessive clearance and showed that the eventual suppression of the midrange subsynchronous vibrations is due to rotor growth which consumes bearing clearance and increases effective preload. A viscoelastic damper applied behind the pads of the FPTPGB-Cs was able to delay the onset of the upper region of subsynchronous vibrations to beyond 50 krpm, but midrange subsynchronous vibrations were negligibly affected. Orbit simulations predicted a large improvement with the addition of the dampers, but it was observed that this is likely the result of an overestimate of the damper's stiffness properties at the actual frequencies where subsynchronous vibrations occurred. Another simulation comparison showed that the effect of dampers decreases as nominal clearance increases.

The fact that the rotor-bearing system was stable at all when shims of 1-3 mil were added was surprising since 3 mil is over two times larger than the estimated nominal bearing clearance of ~30-35 micron. The orbit simulations model an ideal, perfectly aligned system and could only tolerate shim sizes on the order of 10% of nominal clearance. Discrepancies in this regard are believed to be attributed to two significant points of uncertainty: (1) actual bearing clearance which was observed to be non-uniform in the axial direction, and (2) the true level of alignment of the bearings in

the test rig. Misalignments could impose eccentricity or loading effect of the rotor in the bearings which could explain much greater stability of the test rig than predicted by orbit simulations.

The study on the effect of flexible bearing shell supports made use of the newly developed rotor-bearing model with the orbit simulation. The flexible bearing shell support was modeled with structural stiffness properties that mimicked a bump foil-type support. The benefits of such a configuration include the ability to tolerate rotor misalignments and shock loading like foil gas bearings. Although these abilities were not specifically addressed, the identification of rotor-bearing performance characteristics was evaluated as an initial design stage. Placement of the critical speeds that allowed for a large operating range was the key aspect considered. In this regard, FPTPGBs favored larger bearing shell mass and larger support stiffness, while FPTPGB-Cs favored smaller bearing shell mass with larger support stiffness. For design, infinite stiffness would negate the intended purpose of flexible bearing shell support, in particular to comply and tolerate misalignments, thus a prudent design will consider the level of flexibility required to compensate for the misalignments. Similarly, minimum bearing shell mass (favored for the FPTPGB-C case) is physically limited to the minimum amount of material of the structure that provides adequate rigid support to the pads, etc.

REFERENCES

[1] "Descriptions of KTURBO, Inc., Product Line of Turbo Blowers, Turbo Compressors, and Generators," [June 24, 2008], http://www.kturbo.com/english/main.html

[2] "Capstone Microturbine Solutions Product Index," [June 24, 2008], http://microturbine.com/prodsol/products/index.asp

[3] San Andrés, L., 2007, "Current Developments in Gas Bearings for Microturbomachinery [Presentation]," http://www.pucp.edu.pe/congreso/cibim8/pdf/06/06-35.pdf

[4] "Fuel Cell Turbocompressor [Presentation]," May 22, 2003, [June 24, 2008], http://www1.eere.energy.gov/hydrogenandfuelcells/pdfs/merit03/130_honeywell_mark_gee.pdf

[5] Sim, K. and Kim, D., 2007, "Design of Flexure Pivot Tilting Pads Gas Bearings for High-Speed Oil-Free Microturbomachinery," Journal of Tribology, **129**, pp. 112-119.

[6] San Andrés, L., 2006, "Hybrid Flexure Pivot-Tilting Pad Gas Bearings: Analysis and Experimental Validation," Journal of Tribology, **128**, pp. 551-558.

[7] Childs, D., 1993, *Turbomachinery Rotordynamics: Phenomena, Modeling, & Analysis*, John Wiley & Sons, Inc., New York.

[8] Lund, J.W., 1964, "Spring and Damping Coefficients for the Tilting-Pad Journal Bearing," ASLE Transactions, **7**, pp. 342-352.

[9] "Descriptions of Flexure Pivot Journal Bearings," [June 24, 2008], http://www.bearingsplus.com/products/fp_journal_brg.htm

[10] "Descriptions of Flexure Pivot Gas Journal Bearings," [June 24, 2008], http://www.kmcbearings.com/products/journal_bearings/fp_gas_brg.htm

[11] Agrawal, G.L., 1997, "Foil Air/Gas Bearing Technology -- An Overview," International Gas Turbine & Aeroengine Congress & Exhibition, Orlando, FL, ASME Paper No. 97-GT-347.

[12] Sim, K. and Kim, D., 2007, "Thermohydrodynamic Analysis of Compliant Flexure Pivot Tilting Pad Gas Bearings," Accepted to Journal of Engineering for Gas Turbines and Power.

[13] "Tilting Pad Journal Bearings," [June 24, 2008], http://www.rotechconsulting .com/bearings_sub2.htm

[14] Ku, C.-P.R. and Heshmat, H., 1992, "Compliant Foil Bearing Structural Stiffness Analysis: Part I -- Theoretical Model Including Strip and Variable Bump Foil Geometry," Journal of Tribology, **114**, pp. 394-400.

[15] Heshmat, H. and Ku, C.-P.R., 1994, "Structural Damping of Self-Acting Compliant Foil Journal Bearings," Journal of Tribology, **116**, pp. 76-82.

[16] Salehi, M., Heshmat, H., and Walton, J.F., 2003, "On the Frictional Damping Characterization of Compliant Bump Foils," Journal of Tribology, **125**, pp. 804-813.

[17] Dykas, B. and Howard, S.A., 2004, "Journal Design Considerations for Turbomachine Shafts Supported on Foil Air Bearings," Tribology Transactions, **47**, pp. 508-516.

[18] Rubio, D. and San Andrés, L., 2006, "Bump-Type Foil Bearing Structural Stiffness: Experiments and Predictions," Journal of Engineering for Gas Turbines and Power, **128**, pp. 653-660.

[19] Rubio, D. and San Andrés, L., 2007, "Structural Stiffness, Dry Friction Coefficient, and Equivalent Viscous Damping in a Bump-Type Foil Gas Bearing," Journal of Engineering for Gas Turbines and Power, **129**, pp. 494-502.

[20] Song, J.-H. and Kim, D., 2007, "Foil Gas Bearing with Compression Springs: Analyses and Experiments," Journal of Tribology, **129**, pp. 628-639.

[21] Swanson, E.E. and Heshmat, H., 2002, "Oil-Free Foil Bearings as a Reliable, High Performance Backup Bearing for Active Magnetic Bearings," ASME Turbo Expo 2002, Amsterdam, The Netherlands, ASME Paper No. GT-2002-30291.

[22] Sim, K. and Kim, D., 2006, "Stability Analyses on Flexure Pivot Tilting Pad Gas Bearings for Microturbomachinery," STLE/ASME International Joint Tribology Conference, San Antonio, TX, Paper No. IJTC 2006-12158.

[23] Nicholas, J.C., 2003, "Lund's Tilting Pad Journal Bearing Pad Assembly Method," Journal of Vibration and Acoustics, **125**, pp. 448-454.

[24] Lund, J.W., 1968, "Calculation of Stiffness and Damping Properties of Gas Bearings," Journal of Lubrication Technology, **90** (4), pp. 793-803.

[25] Delgado, A., San Andrés, L., and Justak, J.F., 2004, "Analysis of Performance and Rotordynamic Force Coefficients of Brush Seals with Reverse Rotation Ability," ASME Turbo Expo 2004, Vienna, Austria, ASME Paper No. GT2004-53614.

[26] Kim, D., 2007, "Parametric Studies on Static and Dynamic Performance of Air Foil Bearings with Different Top Foil Geometries and Bump Stiffness Distributions," Journal of Tribology, **129**, pp. 354-364.

[27] Kim, D., et al., 2007, "Design and Manufacturing of Meso Scale Tilting Pad Gas Bearings for 100-200W Class PowerMEMS Applications," Submitted to Journal of Engineering for Gas Turbines and Power.

[28] Zhu, X. and San Andrés, L., 2004, "Rotordynamic Performance of Flexure Pivot Hydrostatic Gas Bearings for Oil-Free Turbomachinery," ASME Turbo Expo 2004, Vienna, Austria, ASME Paper No. GT2004-53621.

[29] San Andrés, L. and De Santiago, O., 2003, "Imbalance Response of a Rotor Supported on Flexure Pivot Tilting Pad Journal Bearings in Series with Integral Squeeze Film Dampers," Journal of Engineering for Gas Turbines and Power, **125**, pp. 1026-1032.

[30] "National Instruments LabVIEW Measurement and Automation Software," [2008, June 24], http://www.ni.com/labview/

[31] "LabVIEW Order Analysis Toolkit User Manual," Edition date: July 2005, http://www.ni.com/pdf/manuals/372879c.pdf

[32] "ADRE for Windows / DAIU: Bently Nevada Asset Condition Monitoring," Rev. F (06/07), http://www.gepower.com/prod_serv/products/oc/en/downloads/141577.pdf

[33] Timoshenko, S.P. and Goodier, J.N., 1970, *Theory of Elasticity*, McGraw-Hill, New York, pp. 90-92.

[34] Hamrock, B.J., Schmid, S.R., and Jacobson, B.O., 2004, *Fundamentals of Fluid Film Lubrication*, Marcel Dekker, Inc., New York.

[35] Kim, D., 2004, "Design and Fabrication of Sub-Millimeter Scale Gas Bearings with Tungsten-Containing Diamond Like Carbon Coatings," Ph.D. thesis, The University of Texas at Austin, Austin, TX.

[36] "Data Table of Typical Airborn Particle Sizes," [June 24, 2008], http://www.engineeringtoolbox.com/particle-sizes-d_934.html

[37] "3M Viscoelastic Damping Polymer 110 Technical Data," [June 24, 2008], http://multimedia.mmm.com/mws/mediawebserver.dyn?6666660Zjcf6lVs6EVs666y0GCOrrrrQ-

[38] Kim, T.H. and San Andrés, L., 2007, "Analysis of Advanced Gas Foil Bearings with Piecewise Linear Elastic Supports," Tribology International, **40**, pp. 1239-1245.

[39] "3300 5mm Transducer Specifications," [June 24, 2008], http://www.bently.com/prod/products/datasheets/172036.pdf

[40] "Monarch Instrument Tachometer and Stroboscope Catalog," [June 24, 2008], http://www.monarchserver.com/TSCAT2007.pdf

[41] "NI PCI-4472 Datasheet," [June 24, 2008], http://www.ni.com/pdf/products/us/3sv414-416.pdf

[42] "PCB Piezotronics Model 352C23 ICP Accelerometer Specifications," [June 24, 2008], http://www.pcb.com/spec_sheet.asp?model=352C23&item_id=4708

APPENDIX A

A MANUAL FOR THE SETUP AND OPERATION OF THE FLEXURE PIVOT TILTING PAD GAS BEARING TEST RIG

This manual outlines the setup procedures and instructions for the operation of the test rig. Included are procedures for hardware assembly and alignment, instrumentation specifications, connections, and setup. Also included is a detailed description on the function/use of the developed data acquisition program, a calibration procedure for the eddy current proximity probes, and calibration results used for the experimental analyses.

Bearing Setup and Alignment

Bearing setup is difficult due to tight clearances and low tolerance to misalignments. However, a method of fixing the bearings to "ground" with good alignment but without adjustability is used with noted success. A perfectly aligned rotor-bearing system has the center-lines of the rotor and both bearings in a collinear arrangement, and the centered rotor would have a uniform clearance to the pivot of each pad (i.e. uniform set bore clearance). Therefore, the bearings may be aligned *with respect to the rotor* if a material with the same thickness as the set bore clearance is wrapped around the rotor within the bearings. In the case of the current bearings, the set bore clearance is calculated to be approximately 0.0008" (ref. Table B-2); thus, metal foil shims with a total thickness of 0.001" were wrapped around the rotor within the

bearings to align the three components (Figure A-1). Once the bearings are oriented properly (i.e. proper angular orientation using alignment dowels) and secured to the rotor, the assembly may be fixed to ground by cementing the bottom halves of the bearings to the lower bearing housings using epoxy. The lower bearing housings should be fixed to the test table at the appropriate spacing beforehand, and it should be noted that with the shims in place, the rotor-bearing "assembly" should be fairly rigid (i.e. bearings should not be able to move freely on the rotor). Once the epoxy is fully cured, the rotor and shims may be removed, and the lower halves of the bearings will maintain the original alignment. *Note: Experience shows that this alignment procedure is not without its flaws. Although great care is taken to place the bearings, final alignment is certain to be "off" due to various factors including tilting/radial deflection of the pads while using shims, non-uniform bearing clearances, etc.*

Summary of bearing setup and alignment procedure:

1. Orient and secure bearings to rotor using shims that completely consume the set bore clearance.
2. Fix the bottom halves of the bearings (rotor and bearings still assembled as in Step 1) to the lower bearing housings using epoxy.
3. Wait for epoxy to fully cure, then bearing alignment is complete and rotor and shims may be removed.

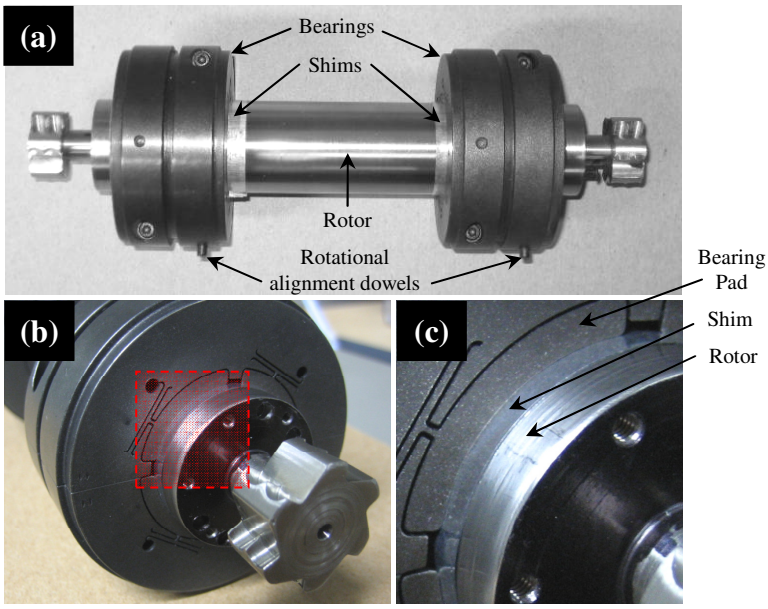

Figure A-1: **Rotor-bearing relative alignment – (a) rotor wrapped with shims within bearings to consume set bore clearance; (b) end view of aligned bearing at "Front" of rotor; (c) magnification of end view showing the shim between the rotor and the bearing pad.**

Turbine Shroud and Thrust Bearing Alignment

After the bearings are aligned and fixed to the bearing housings, the turbine shrouds and thrust bearings are installed. The turbine shroud and thrust nozzle assembly has various adjustments as shown in Figure A-2. The base plate (A) has slots that allow horizontal adjustment (X-direction), and four set screws may be adjusted to set the proper height and level of the base plate. The turbine shroud block (B) has axial adjustability (Z-direction) to properly align the turbine shroud air feed holes with the turbine on the rotor, and the thrust nozzle base (C) has also has axial adjustability to set the gap of the thrust bearing. The thrust nozzle itself (D) is attached to the thrust nozzle base and has no designed adjustability.

The alignment procedure for the turbine shroud and thrust nozzle assemblies is as follows (all of the alignment should be done without the air lines connected for convenience):

1. Begin turbine shroud alignment procedure on one side of the test rig (i.e. “Front” or “Rear”), making sure that the rotor is in the desired axial position.

2. Loosely attach the turbine shroud block (B) to the base plate (A) and set into position such that the turbine on the rotor is inside the turbine shroud and the base plate mounting slots are positioned over test table mounting holes.

3. Adjust set screws in base plate until proper height and level are achieved to center the turbine shroud on the turbine.

4. Tighten the base plate mounting bolts so that the base plate is fixed to the test table.

5. Adjust the axial location of the turbine shroud block to position the turbine shroud air feed holes properly on the turbine and tighten in place (make sure that turbine shroud does not directly contact the turbine).

6. Check alignment of the turbine inside the turbine shroud. Use a feeler gage or shims to verify sufficient clearance exists between the turbine and turbine shroud.

7. If any further adjustments need to be made, repeat Steps 3-6 until alignment is satisfactory.

8. Repeat Steps 2-7 to align the turbine shroud on the other side of the test rig.

9. Begin thrust nozzle alignment procedure on one side of the test rig (i.e. “Front” or “Rear”), making sure that the rotor is still in the desired axial position.

10. Attach the thrust nozzle (D) to the thrust nozzle base (C).

11. Apply permanent marker to the face of the thrust nozzle. Place the thrust nozzle base on the turbine shroud block with the thrust nozzle face against the end of the turbine (within the turbine shroud). Slide the thrust nozzle face against the end of the turbine to wear off the marker where contact is made.

12. Remove the thrust nozzle and base to check the wear of the marker on the thrust nozzle face.

13. If the thrust nozzle face does not have equal wear on the top and bottom (indicating misalignment), reattach the thrust nozzle to the thrust nozzle base with shims inserted to re-align the thrust nozzle face to be "flat" with the end of the turbine.

14. Repeat Steps 11-13 until proper orientation of the thrust nozzle face is achieved.

15. Repeat Steps 10-14 to align the thrust nozzle on the other side of the test rig.

16. Bolt the thrust nozzle bases to the turbine shroud blocks such that an even gap exists between the thrust nozzle faces and the ends of both turbines.

17. The gap between the thrust nozzles and the ends of the turbines may be checked by measuring the amount of travel the rotor has in the axial direction using a dial indicator.

18. If the gap is too large/small, repeat Steps 16-17 with the proper adjustments until a satisfactory gap is achieved. Experience shows that a gap of ~0.005" is a good starting point of reference. *Note: This may also need to be considered after running an initial test. For example, while running a test, the operator observes axial instability (air-hammering effect) in the thrust bearing; this is likely due to low stiffness in the thrust air caused by too large of a gap and/or misalignment of the thrust nozzle face and the end of the turbines.*

The alignment procedure for the turbine shroud and thrust nozzle assemblies can be time consuming. In the event that the rotor needs to be removed, one of the turbine shrouds must first be removed. Then, the turbine shroud must be realigned as in Step 8, above. To avoid this, an alignment block (E) is used which is fixed to the test table and positioned along two edges of the base plate. Thus, the entire turbine shroud and thrust nozzle assembly on one side of the test rig may be removed and replaced using the alignment block to reposition the base plate (and the entire turbine shroud and thrust nozzle assembly) according to the previous alignment. *Caveat: The use of the alignment block to realign the turbine shroud and thrust nozzle assembly should be done very carefully. If the re-positioning is not done precisely (e.g. tightening bolts in the*

exact reverse manner that they were originally removed, etc.), alignment will off, and rotor performance could suffer. Experience has shown that the alignment block is better used as a guide, and verifications of proper alignment should still be employed (i.e. Steps 6 and 18, above).

An alternative to performing tedious re-alignment on one of the turbine shrouds every time the rotor is removed is to simply operate the test rig by driving only one turbine. In this case, rotor removal only requires that the one thrust nozzle be taken out and replaced. Experience has shown that this test rig configuration yields satisfactory operation and simpler, more repeatable re-alignment in the case where the rotor needs to be removed between tests.

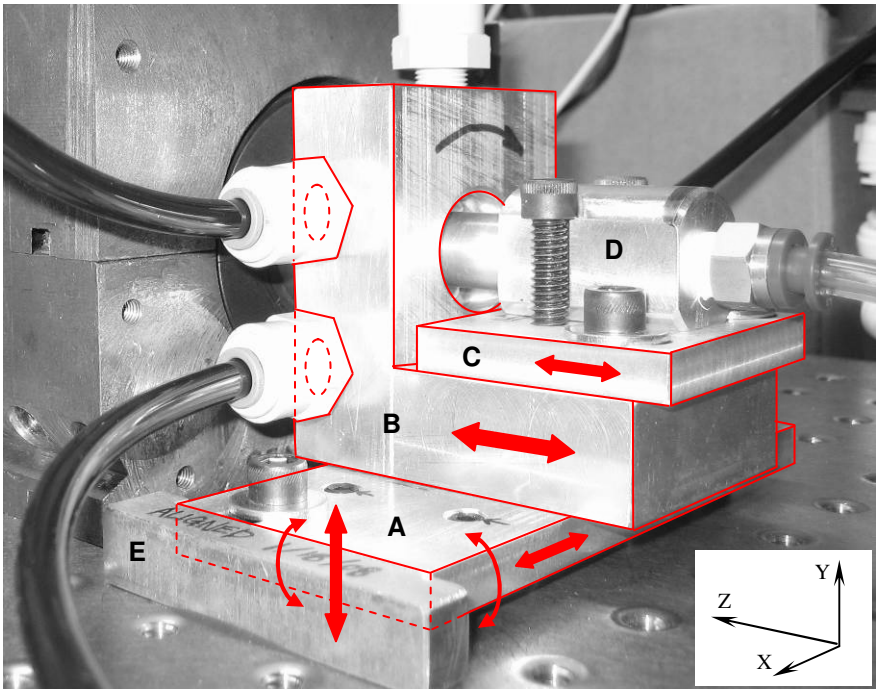

Figure A-2: Turbine shroud and thrust nozzle assembly adjustments.

Instrumentation Specifications

Figure A-3 shows the schematic of the data acquisition system setup, and Table A-1 lists the corresponding descriptions and specifications. Further descriptions are also included in the following sections.

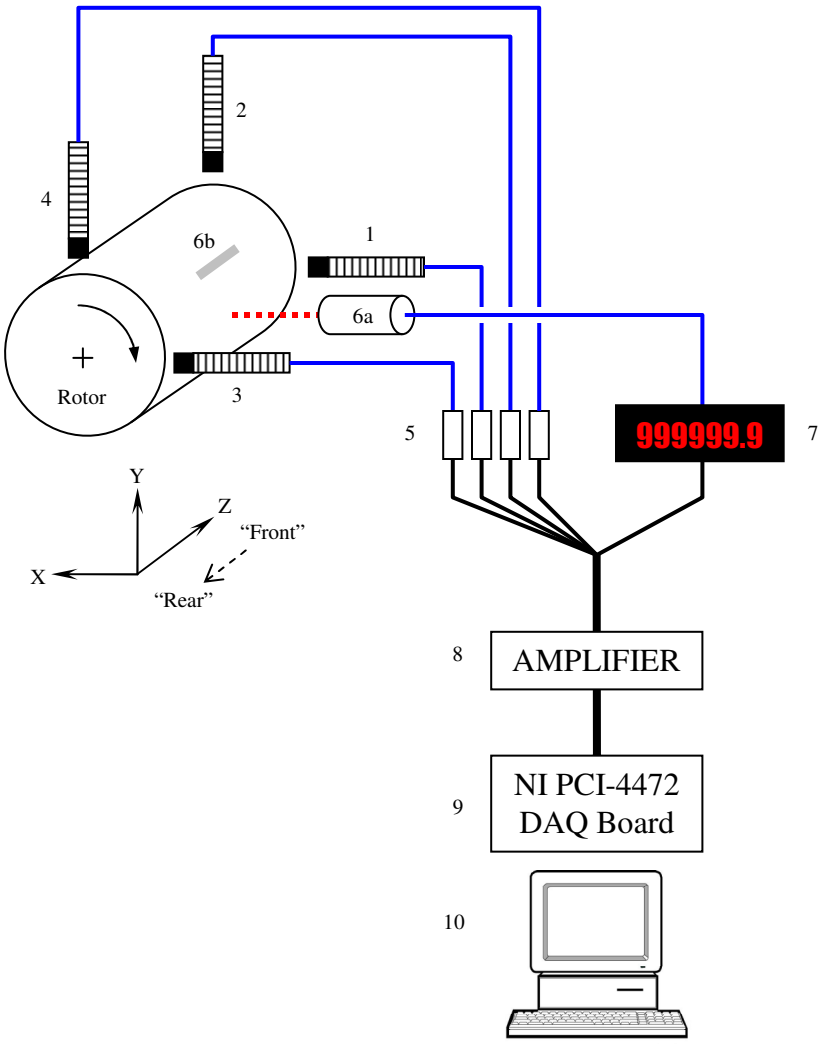

Figure A-3: Data acquisition schematic – numbers refer to Table A-1.

Table A-1: Data acquisition components.

#	Component	Description
1	Prox. probe: 'Front-Horizontal'	Bently Nevada 3300 5mm eddy current proximity probes P/N 330171 (1/4-28 UNF threads, without armor). Used with 3300 XL extension cables. Ref. [39].
2	Prox. probe: 'Front-Vertical'	
3	Prox. probe: 'Rear-Horizontal'	
4	Prox. probe: 'Rear-Vertical'	
5	Proximitor sensors (oscillator demodulators)	Part of 3300 5mm Proximity Transducer System; uses -24 Vdc input. Ref. [39].
6a	Optical or infrared tachometer	Monarch Instrument ROS (Remote Optical Sensor, 1-250.00 krpm range) or IRS (Infrared Sensor, 1-999.99 krpm range). Ref. [40].
6b	Tachometer target	ROS requires reflective tape; IRS requires contrasting color (e.g. marker on surface). Ref. [40].
7	Tachometer power supply / digital readout	Monarch Instrument ACT-3 Panel Tachometer/Ratemeter/ Totalizer; uses 115 Vac input and supplies 5-8 Vdc to sensors. Ref. [40].
8	Amplifier	Encore model 517-001 amplifier.
9	Data acquisition (DAQ) board (in PC tower)	National Instruments PCI-4472 dynamic signal board (8-channel, 24-bit resolution, 102.4 kHz sample rate, input ± 10 V, etc.). Ref. [41].
10	PC equipped with *LabVIEW* software	National Instruments *LabVIEW 8.2* – Ref. [30].

Data Acquisition System Connections and Settings

Proximity Transducer System

Proximity probes are placed in the bearing housings with an appropriate initial gap within the transducer's linear range (≈ 0.1-0.9 mm useable linear range with data acquisition system; refer to proximity probe calibration results in the next section). Initial gaps are set at approximately one-half revolution of the probe threads (i.e. allow probe tip to contact rotor, then apply one-half turn counterclockwise) yielding an approximate gap of:

$$\text{½ revolution} = 0.5 \times 1/28 \text{ in.} = 0.018 \text{ in.} = 0.45 \text{ mm}$$

NOTE: The initial gap should be adjusted for better performance. It was observed that pseudo-frequencies were produced by the proximity probes depending on proximity probe gaps when the rotor was stationary. The errant frequencies from the probes were reduced to a satisfactory level by increasing/decreasing the gaps of the probes in a trial-and-error manner. The phenomenon observed is suspected to be signal "cross-talk" between adjacent eddy current proximity probes.

Proximity probe leads are connected with extension cables to the oscillator demodulators, which are wired according to the schematic shown in Figure A-4. Power is supplied to the oscillator demodulators by a DC power source, with supply leads connected as shown in Figure A-5. Note that the negative terminal of the power supply

is connected to "V-IN", and the positive terminal of the power supply is connected to "COM" in order to supply the required -24 Vdc power.

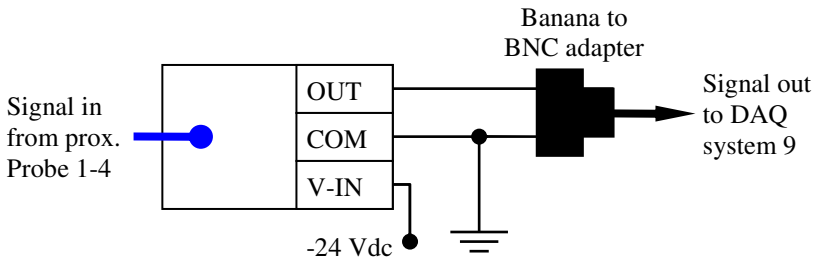

Figure A-4: Oscillator demodulator wiring schematic.

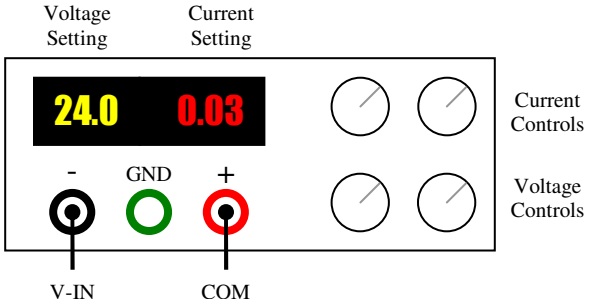

Figure A-5: DC regulated power supply (BK Precision Model 1627A); connection diagram for supplying -24 Vdc to oscillator demodulators.

Tachometer System

The tachometers are set up according to manufacturer specifications (target type, distance to target, etc.). The ACT-3 Panel Tachometer/Ratemeter/Totalizer is connected (hard-wired) according to the instruction manual and was operated in RPM Mode.

NOTE: Using the IRS tachometer, a black permanent marker target with ~15% duty cycle (span approximately 60˚ on rotor surface) was used successfully with the LabVIEW DAQ system to read rotor spin speed. Targets with a duty cycle less than 5%

were observed to occasionally give false readings by the LabVIEW DAQ system (readings compared to display of ACT-3 Panel Tachometer/Ratemeter/Totalizer).

Amplifier

The amplifier uses BNC-male connectors on the back panel for input and output. Input connections are labeled “X.1 1 MEG Z” and “X1 100K Z”. The X.1 and X1 connections multiply the input signal’s amplitude by 0.1 and 1, respectively. For all experiments, the X.1 input port was used along with the “Gain” setting of 10 on the front panel; thus the net gain of the input signal to the output is $0.1 \times 10 = 1$. Other front panel settings and their descriptions are listed in Table A-2. Note that the “Phase” setting is “NOR” (normal) or “INV” (inverted) – the vertical proximity probes require the “NOR” setting since they are mounted in the same direction as the Y-axis, while the horizontal proximity probes require the “INV” setting since they are mounted in the opposite direction as the X-axis (see Figure A-3). In this manner, the signals from the proximity probes correctly represent the positive-X and positive-Y positions of the rotor center.

Table A-2: Amplifier front panel settings.

Name	Description	Control Type	Setting
Phase	Changes sign of input signal	Toggle switch	NOR or INV depending on proximity probe direction
Mode	-	Toggle switch	DC
Range	-	Toggle switch	20
Polarity	-	Toggle switch	+
DC Null	Adjustable DC offset	Rotary dial	0
Gain	Multiply input signal amplitude	Rotary switch	10
Vernier	-	Rotary dial	Off

LabVIEW DAQ System (Hardware)

The NI PCI-4472 dynamic signal acquisition board has nine inputs: eight signal input channels and an external trigger channel. Connection of signals to the PCI board using BNC cables requires the use of SMB to BNC adapter cables (National Instruments SMB 100, # 763389-01). Connection of the various input signals to the PCI input channels are shown in Table A-3.

Table A-3: PCI board connections.

PCI-4472 Channel No.	Signal Input
0	Prox. probe 1: 'Front-Horizontal'
1	Prox. probe 2: 'Front-Vertical'
2	Prox. probe 3: 'Rear-Horizontal'
3	Prox. probe 4: 'Rear-Vertical'
4	Tachometer
5	*- Not used -*
6	*- Not used -*
7	*- Not used -*
Ext.Trigger	*- Not used -*

LabVIEW DAQ System (Software)

A data acquisition (DAQ) program was created in *LabVIEW* – the program is referred to as a virtual instrument, or VI. The basic functions of the VI are to **(a)** read incoming voltage signals from the NI PCI-4472 board and convert voltage to the appropriate physical units represented by the various sensors, **(b)** display the signals in various formats (e.g. time trace and XY plots, FFT, etc.), and **(c)** save test data to be kept as a record and/or used by other programs for post-processing tasks. Descriptions of the VI's front panel components are outlined below; primary outline numbers correspond to labeling of Figure A-6.

LabVIEW VI front panel components:

1. Device and VI settings

   a. 'DAQ Settings' tab: User controls DAQ sample rate and number of samples to read.

      i. Sample rate should be sufficient to capture the maximum desired frequency component at the maximum operating speed. For example, if it is desired to obtain the nX frequency component at a maximum operating speed of N rpm, Nyquist's theorem requires that the sampling frequency be $F_s \geq nN/30$ Hz.

      ii. The number of samples to read should be sufficient for the processing and saving of the data – typical default setting is $F_s \times (0.1\text{ s})$ samples.

   b. 'Amplifier Settings' tab: User records gain settings of amplifier. Gain settings are used to properly convert proximity probe voltages to units of length.

   c. 'Probe Settings' tab: User controls proximity probe gains and gap offsets.

      i. Proximity probe gains (mV/mm) are found by calibration procedures. Values of proximity probe voltages (post-amplifier voltages) are displayed along with the calculated probe gap (considering net amplifier and proximity probe gains). The displayed proximity probe voltages are necessary to verify that the voltages are not being saturated by the PCI board (recall input voltage limits are ± 10 V).

      ii. The gaps may be offset by the user control of 'DC Offset' to set the relative position display to the desired value. Relative position is calculated (with the appropriate unit conversions) by:

$$\text{Rel. pos.} = V_{\text{in}} \frac{1}{G_{\text{probe}}} \frac{1}{G_{\text{amp.}}} + \Delta_{\substack{\text{DC} \\ \text{offset}}}$$

   d. 'Tachometer' tab: User controls tachometer signal processing parameters.

      i. 'Offset' is the voltage that shifts the raw tachometer signal such that non-triggered events are approximately 0 V.

      ii. 'Threshold' is the voltage above which triggering occurs.

iii. 'Scale' corresponds to the amplitude of the recreated tachometer pulse train (should be ≥ 2).

iv. Tachometer signal "filter" indicator LED

- OFF when rotor speed is less than 20 Hz. Rotor speed is calculated as the frequency of the largest-amplitude component of the tachometer time signal using the "Tone Measurements" sub-VI.

- ON when rotor speed is greater than 20 Hz. Rotor speed is calculated by the inverse of the period of the tachometer time signal pulses using the "Pulse Measurements" sub-VI. This method for determining rotor speed is more accurate than using the "Tone Measurements" sub-VI; however, at near-infinite pulsewidth (i.e. near-zero frequency), this method will return an error and cause the program to terminate.

v. *Example using tachometer controls:* The following diagram shows an example of the evolution of the raw tachometer signal to the recreated pulse train. The notation inside the [ ] indicates the signal value for triggered events (upper value) and non-triggered events (lower value). Note that the output of the threshold comparison is a digital Boolean output (1 = true, 0 = false), which have no units.

$$\begin{bmatrix} 0.0\ \text{V} \\ -4.78\ \text{V} \end{bmatrix} \xrightarrow[+4.8\ \text{V}]{\text{Offset}} \begin{bmatrix} 4.8\ \text{V} \\ 0.02\ \text{V} \end{bmatrix} \xrightarrow[+1.5\ \text{V}]{\text{Threshold}} \begin{bmatrix} 1 \\ 0 \end{bmatrix} \xrightarrow[5]{\text{Scale}} \begin{bmatrix} 5 \\ 0 \end{bmatrix}$$

e. 'Checklist' tab: This tab contains no user controls or displays other than a practical checklist for proper testing procedures using the VI.

2. Tachometer frequency display

a. Digital readout displays rotor speed in Hertz (Hz) and thousands of revolutions per minute (krpm).

b. Fill bar indicates current speed relative to maximum target speed (i.e. 120 krpm).

3. Data saving controls

a. User specifies the complete saved data filepath (location of saved data files) in the appropriate boxes. Time signal data and FFT data are saved as text files (**.txt*) with separate filename prefixes (*TSIG_data* and *FFT_data*, respectively). Multiple files are distinguished by sequential numbering of *_0001*, *_0002*, etc., added to the end of each file name prefix. Each file number corresponds to a "snapshot" at a single rotor speed. The format of the saved data is shown in Table A-4 and Table A-5.

b. Data may be saved manually (by pressing the ‘MANUAL SAVE’ button) or according to a timer (by toggling the ‘TIME SAVE “ON/OFF”’ button to the “ON” position). The timer is specified by “wait time” (time between save events) and “duration” (length of time that intermittent save control is activated). Minimum duration should be 0.1 s.

c. Green LEDs indicate when data is being saved by the VI.

4. Fast Fourier Transform (FFT) plots. Displays FFT amplitudes vs. frequency spectrum for proximity probe signals; amplitudes in microns.

5. Time trace plots (relative position vs. time) for proximity probes and tachometer pulse train. Probe displacements in microns; tachometer signal is dimensionless.

   a. ‘Sampled Signals’ tab presents live display of sampled signals, updated every number of samples read (refer to ‘DAQ Settings’).

   b. ‘Triggered Signals’ tab presents sampled signals triggered at the rising edge of the tachometer pulse.

6. XY plots (or orbit plots) of vertical vs. horizontal relative displacements in microns.

   a. ‘Sampled Signals’ tab presents live display of sampled signals, updated every number of samples read (refer to ‘DAQ Settings’).

   b. ‘Triggered Signals’ tab presents the orbit trace for one revolution of the rotor, including markers for the X-Y position of the rotor when the trigger occurs and markers that show the direction of the trace.

7. ‘Front’ location graphic displays – color matches color-coding on test rig.

8. ‘Rear’ location graphic displays – color matches color-coding on test rig.

Data Processing

A data processing program was written using MATLAB language. The program reads the saved data files created by the *LabVIEW* DAQ program and performs various tasks depending on the file's data as shown in the flow diagram (Figure A-7). Processing the FFT data is relatively straight-forward since it is only necessary to plot the FFT spectra versus rotor speed, which is accomplished using MATLAB's built-in 'waterfall' plotting command. The methodology for processing the time-signal data is more involved and requires further description.

1. Average rotor position
    a. Each set of time signal data (e.g. all 20,000 data points taken during 0.2 second time period) is assumed to be at a quasi-steady speed during coastdown tests.
    b. Average rotor position at a given quasi-steady speed is taken as the mean of the time signals for the corresponding set of data points (both X- and Y-directions). In general, the average rotor position is relative to the rotor-bearing system coordinate origin (i.e. zero position as displayed by the proximity probes), such that the mean values may not represent the actual displacements from the bearing origin.
    c. The average rotor positions are normalized (i.e. shifted) such that the positions of the rotor at the maximum speed become (0,0). *NOTE: Often when taking data, the first data point is recorded before the turbine drive air supply is turned off. However, the average rotor position is strongly influenced by this air pressure, therefore this first point is not considered in the normalization step since we are most interested in the rotor position due to bearing forces.*
2. Amplitude and phase angles of synchronous response
    a. Bandpass filtering
        i. Raw rotor vibration data (i.e. time signals) are processed by a digital bandpass filter, which is a Butterworth-type filter that utilizes MATLAB's built-in 'butter' command and a pass band of ±3% of the synchronous frequency.

ii. The filtered signals represent the synchronous response of the rotor; however, due to the nature of the filtering of a digital signal, the resulting signal is only accurate after a sufficient number of data points has been processed. A study of the accuracy the bandpass filtering process is presented in Appendix C. The main conclusion is that accurate results may be obtained for all rotor speeds above 6 krpm (100 Hz).

b. Compute amplitude and phase angle

i. A synchronous filtered signal has an amplitude A and phase angle ϕ and is represented by $a(t) = A\cos(\omega t + \phi)$.

ii. Vibration amplitude is calculated as half of the maximum value minus the minimum value, or:

$$A = \frac{1}{2}\left[\max(a(t)) - \min(a(t))\right] \tag{A-1}$$

iii. Phase lag is calculated by the synchronous frequency multiplied by the time difference from the rising edge of the tachometer signal to the peak of the response, i.e. $\phi_{LAG} = \omega \Delta t_{LAG}$. Phase angle represented in $a(t) = A\cos(\omega t + \phi)$ is the negative of the phase lag, or:

$$\phi = -\phi_{LAG} = -\omega \Delta t_{LAG} \tag{A-2}$$

iv. Resolution of the phase angle measurement is determined by the sample rate and rotor speed: resolution increases with sample rate and decreases with rotor speed. For the 100 kHz sample rate and a rotor speed of 120 krpm, the resolution of the phase angle is 7.2˚, which makes the maximum error of the phase angle measurement ± 3.6˚.

3. Major amplitude of ellipse

a. Magnitude and phase angle of the synchronous filtered signals of a horizontal/vertical proximity probe pair are computed to represent the rotor position as $x(t) = X\cos(\omega t + \phi_x)$ and $y(t) = Y\cos(\omega t + \phi_y)$.

b. Childs [7] lists the derivation of the major amplitude of the ellipse formed by $x(t) = x_c\cos(\omega t) + x_s\sin(\omega t)$ and $y(t) = y_c\cos(\omega t) + y_s\sin(\omega t)$.

i. The major amplitude is computed as

$$a = [A + (B^2 + C^2)^{1/2}]^{1/2} \tag{A-3}$$

with

$$\begin{aligned} A &= (x_c^2 + y_c^2 + x_s^2 + y_s^2)/2 \\ B &= (x_c^2 + y_c^2 - x_s^2 - y_s^2)/2 \\ C &= x_c x_s + y_c y_s \end{aligned} \tag{A-4}$$

ii. From (a) and (b),

$$\begin{aligned} x_c &= X\cos(\phi_x); \quad x_s = -X\sin(\phi_x) \\ y_c &= Y\cos(\phi_y); \quad y_s = -Y\sin(\phi_y) \end{aligned} \tag{A-5}$$

c. Summarizing: The magnitudes and phase angles (X, Y and ϕ_x, ϕ_y) of an orthogonal pair of proximity probe signal are measured first. Then, using Equations (A-4) and (A-5), the major amplitude of the ellipse is computed by Equation (A-3).

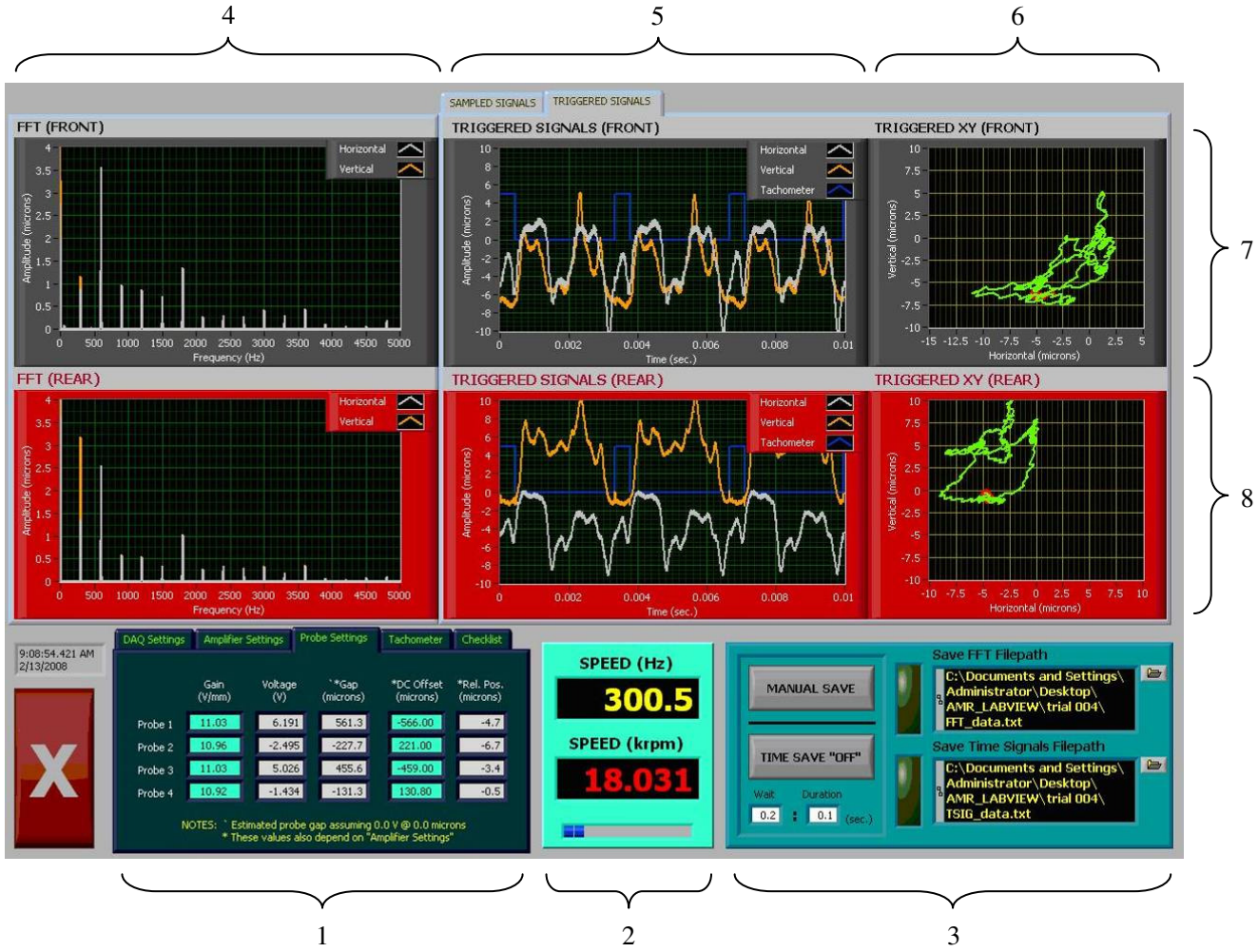

Figure A-6: ***LabVIEW*** **VI front panel.**

Table A-4: Format of saved data for *TSIG_data_####.txt*.

Headers are column numbers of file; numbers in parentheses are indices of time;
Sync = tachometer frequency [Hz], t = time [s], Tach = tachometer signal [no units],
Probe signals (F/R = Front/Rear, H/V = Horizontal/Vertical) [microns]

1	**2**	**3**	**4**	**5**	**6**
0	Sync	t(1)	Tach(1)	t(1)	FH(1)
0	0	t(2)	Tach(2)	t(2)	FH(2)
0	0	t(3)	Tach(3)	t(3)	FH(3)
:	:	:	:	:	:
7	**8**	**9**	**10**	**11**	**12**
t(1)	FV(1)	t(1)	RH(1)	t(1)	RV(1)
t(2)	FV(2)	t(2)	RH(2)	t(2)	RV(2)
t(3)	FV(3)	t(3)	RH(3)	t(3)	RV(3)
:	:	:	:	:	:

Table A-5: Format of saved data for *FFT_data_####.txt.*

Headers are column numbers of file; numbers in parentheses are indices of frequency;
Sync = tachometer frequency [Hz], f = FFT frequency spectrum [Hz],
Probe signal FFT amplitudes (F/R = Front/Rear, H/V = Horizontal/Vertical) [microns]

1	**2**	**3**	**4**	**5**	**6**
0	Sync	f(1)	FH(1)	f(1)	FV(1)
0	0	f(2)	FH(2)	f(2)	FV(2)
0	0	f(3)	FH(3)	f(3)	FV(3)
:	:	:	:	:	:
	7	**8**	**9**	**10**	
	f(1)	RH(1)	f(1)	RV(1)	
	f(2)	RH(2)	f(2)	RV(2)	
	f(3)	RH(3)	f(3)	RV(3)	
	:	:	:	:	

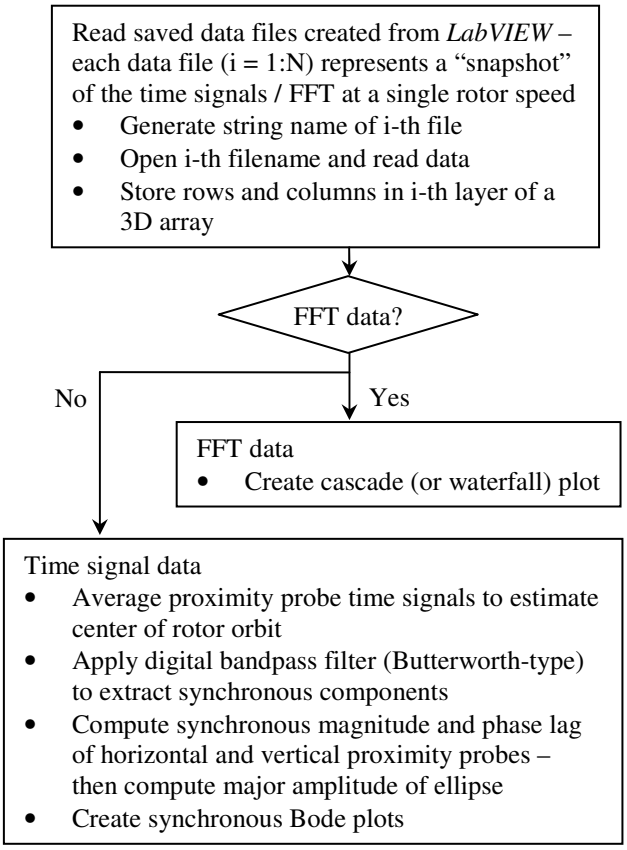

Figure A-7: Flow diagram for automated data processing program.

Eddy Current Proximity Probe Calibration Procedure and Results

The eddy current proximity probes were calibrated to the test rig before performing any experiments. This section presents the setup and procedure used to obtain calibration data as well as the actual data collected by two measurement methods: (1) record voltages with digital multimeter and (2) record voltages with the computer data acquisition system. The steps of the calibration procedure are listed below, which refer to the setup is illustrated in Figure A-8. Note that the setup uses the rotor as it is installed in the test rig, i.e. the probes are calibrated in an environment that is nearly identical to actual test conditions.

Calibration Procedure

1. Fix linear stage to base near test rig (approximately 3.5" from rotor centerline, centered between bearings).
2. Attach proximity probe to be tested to 90˚ angle bracket with two 1/4-28 UNF jam nuts. Note that bracket must hold probe at proper height equal to the height of the rotor center.
3. Attach angle bracket to linear stage such that orientation of proximity probe is perpendicular to the rotor axis.
4. Set the initial proximity probe gap near zero for a starting point of calibration.
    a. Decrease the gap between the probe and the rotor using the linear stage's micrometer adjustment.
    b. Use a shim (or feeler gage) to set the initial gap as the thickness of the shim, i.e. when shim is no longer free to move between probe tip and rotor surfaces.
    c. NOTE: For proximity probe calibration, it is not critical that the absolute gap of the proximity probe is known – only the linear behavior (ΔVoltage / Δgap) is critical. Thus, the probe may be set arbitrarily close to the rotor for a starting

point; however, precise measurement of the actual gap may be used to verify saturation points (i.e. useful to determine linear range) of the transducer.

5. Record the initial gap and the corresponding micrometer reading (linear stage adjustment) and voltage (1st data point).

6. Increase the proximity probe gap a desired amount for the 2nd data point. It is preferable that the 2nd data point be at a gap that corresponds with a *nominal* reading on the linear stage's micrometer adjustment – this will simplify subsequent data collection. Record the micrometer reading and the voltage and calculate the gap as: $\text{gap}_n = \text{gap}_{n-1} + \Delta(\text{micrometer reading})$.

7. Repeat Step 6 for a prescribed gap increment (preferably nominal on the linear stage's micrometer adjustment) until a sufficient number of data points is collected – e.g. capture both lower and upper saturation points of the proximity transducer system.

8. Plot results and determine linear curve-fitting coefficients for the linear ranges of the data.

9. Reject any probes if calibration data does not exhibit linear behavior.

Calibration Data and Results

Initial calibration was performed to identify four satisfactory probes. The initial calibration (CAL-1) used a digital multimeter to record voltages. The calibration data of four passing probes (Table A-6) and two unsatisfactory probes (Table A-7) is presented, along with the corresponding plots (Figure A-9) and least-squares curve fitting parameters (Table A-8). Passing probes used in the test rig are numbered 1-4 (corresponding with the numbering followed in Figure A-3 and Table A-1), while failing probes are numbered 4-a and 4-b (based on order in which probes were evaluateded: 1, 2, 3, 4-a, 4-b, 4). Initial gap was estimated using a 0.0005" (0.013 mm) shim. The final summary of the proximity probe calibration CAL-1 is shown in Table A-9.

A second calibration (CAL-2) was performed following the same procedure as previous, except using the computer data acquisition (DAQ) system to measure voltages. It should be noted that since the DAQ system records all measurements during tests, this calibration method should be considered more accurate. However, a minor drawback of the method is in the voltage limit of the NI PCI-4472 DAQ board (input less than ± 10 V), resulting in a limited "view" of the overall performance of the instrument being calibrated (saturation limits, linearity, etc.). For example, the most noticeable nonlinearity of the failed probes 4-a and 4-b is exhibited from 10-19 V (Figure A-9), and may have been more difficult to detect if readings did not exceed 10 V[11]. In light of these points, re-calibration of the passing proximity probes 1-4 was performed to obtain more accurate gain values.

Table A-10 shows the calibration data from CAL-2; Figure A-10 presents the corresponding plot. Note that all voltages are below the 10 V limit – incidentally, the tenth data point for probe 3 was greater than 10 V and is not included. The least-squares fit of the CAL-2 data (Table A-11) shows good correlation, but different calibration results than with CAL-1 (Table A-8). The differences in the measurements may be attributed to losses within the amplifier, since voltage readings using the multimeter were taken directly after the oscillator demodulators, or the multimeter may be in need of recalibration. In summary, the results of this test are taken to be more accurate since

[11] It is recognized that another "fail" criterion would be an insufficient correlation coefficient from a least-squares linear fit of the data. The data from probes 4-a and 4-b would likely have relatively low correlation coefficients compared to the passing probes, even if data less than 10 V were considered; however, this should not detract from the intended point of a possible drawback of the method as presented.

calibration was performed with the same equipment that is used in subsequent experiments; however the prior method may still be acceptable if necessary since errors in the measured gains were less than 3.5% as shown in Table A-12.

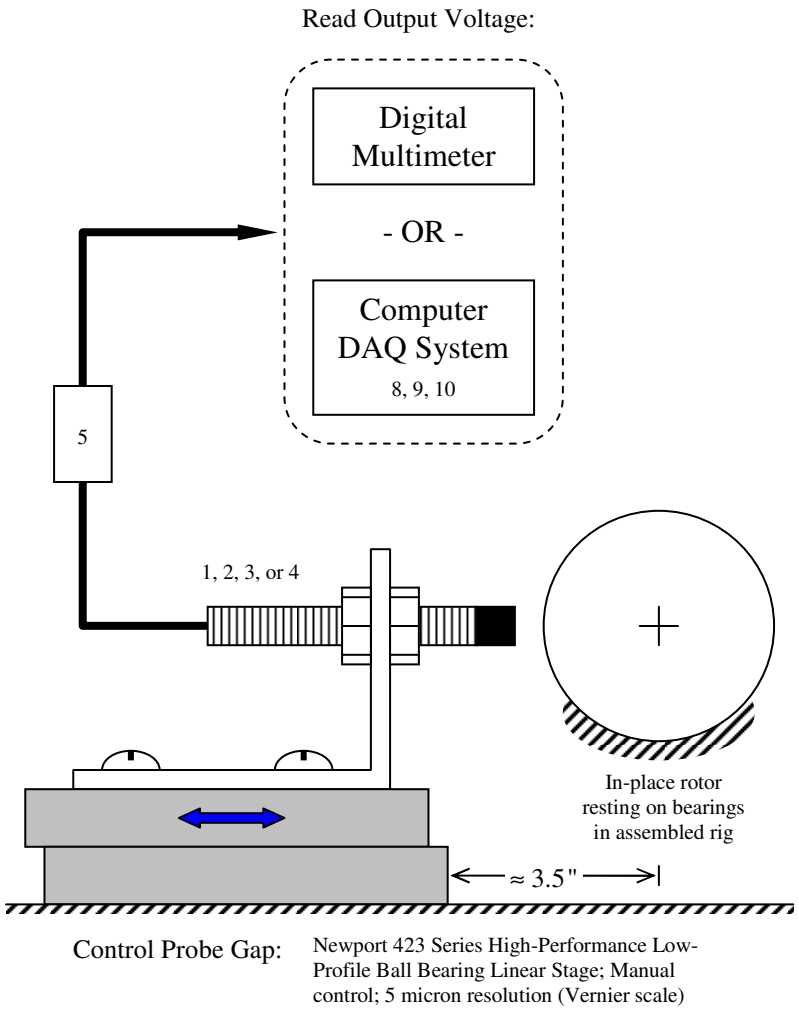

Figure A-8: Proximity transducer system calibration schematic. Numbers refer to components in Figure A-3 and Table A-1.

Table A-6: Calibration data for passing proximity probes (CAL-1).

*V = voltage reading; **mic** = micrometer reading (mm); **gap** = proximity probe gap (mm)*

	1			2			3			4		
	V	**mic**	**gap**	**V**	**mic**	**gap**	**V**	**mic**	**gap**	**V**	**mic**	**gap**
1	0.655	6.465	0.013	0.630	7.135	0.013	0.657	8.715	0.013	0.645	8.855	0.013
2	0.671	6.450	0.028	0.654	7.100	0.048	0.674	8.700	0.028	0.842	8.800	0.068
3	1.631	6.350	0.128	1.480	7.000	0.148	1.644	8.600	0.128	1.963	8.700	0.168
4	2.731	6.250	0.228	2.608	6.900	0.248	2.766	8.500	0.228	3.086	8.600	0.268
5	3.293	6.200	0.278	3.726	6.800	0.348	3.920	8.400	0.328	4.172	8.500	0.368
6	4.417	6.100	0.378	4.830	6.700	0.448	5.025	8.300	0.428	5.313	8.400	0.468
7	5.532	6.000	0.478	5.939	6.600	0.548	6.147	8.200	0.528	6.396	8.300	0.568
8	6.64	5.900	0.578	7.02	6.500	0.648	7.26	8.100	0.628	7.50	8.200	0.668
9	7.74	5.800	0.678	8.11	6.400	0.748	8.32	8.000	0.728	8.58	8.100	0.768
10	8.80	5.700	0.778	9.17	6.300	0.848	9.42	7.900	0.828	9.65	8.000	0.868
11	9.89	5.600	0.878	10.24	6.200	0.948	10.48	7.800	0.928	10.73	7.900	0.968
12	10.95	5.500	0.978	11.31	6.100	1.048	11.56	7.700	1.028	11.77	7.800	1.068
13	12.02	5.400	1.078	12.35	6.000	1.148	12.65	7.600	1.128	12.82	7.700	1.168
14	13.09	5.300	1.178	13.41	5.900	1.248	13.70	7.500	1.228	13.87	7.600	1.268
15	14.16	5.200	1.278	14.45	5.800	1.348	14.76	7.400	1.328	14.89	7.500	1.368
16	15.21	5.100	1.378	15.48	5.700	1.448	15.82	7.300	1.428	15.94	7.400	1.468
17	16.27	5.000	1.478	16.52	5.600	1.548	16.89	7.200	1.528	16.98	7.300	1.568
18	17.35	4.900	1.578	17.56	5.500	1.648	17.97	7.100	1.628	18.02	7.200	1.668
19	18.42	4.800	1.678	18.60	5.400	1.748	19.04	7.000	1.728	19.07	7.100	1.768
20	19.50	4.700	1.778	19.66	5.300	1.848	20.14	6.900	1.828	20.11	7.000	1.868
21	20.61	4.600	1.878	20.73	5.200	1.948	21.25	6.800	1.928	21.19	6.900	1.968
22	21.72	4.500	1.978	21.81	5.100	2.048	22.40	6.700	2.028	22.27	6.800	2.068
23	22.90	4.400	2.078	22.90	5.000	2.148	23.08	6.600	2.128	23.08	6.700	2.168
24	23.07	4.300	2.178	23.07	4.900	2.248	23.07	6.500	2.228	23.06	6.600	2.268

Table A-7: Calibration data for failing proximity probes (CAL-1).

***V** = voltage reading; **mic** = micrometer reading (mm); **gap** = proximity probe gap (mm)*

	4-a (fail)			4-b (fail)		
	V	**mic**	**gap**	**V**	**mic**	**gap**
1	0.646	8.575	0.013	0.643	5.270	0.013
2	1.004	8.500	0.088	0.961	5.200	0.083
3	2.072	8.400	0.188	2.018	5.100	0.183
4	3.095	8.300	0.288	3.040	5.000	0.283
5	4.102	8.200	0.388	4.082	4.900	0.383
6	5.122	8.100	0.488	5.089	4.800	0.483
7	6.090	8.000	0.588	6.094	4.700	0.583
8	7.07	7.900	0.688	7.08	4.600	0.683
9	8.02	7.800	0.788	8.02	4.500	0.783
10	8.94	7.700	0.888	8.96	4.400	0.883
11	9.86	7.600	0.988	9.87	4.300	0.983
12	10.72	7.500	1.088	10.76	4.200	1.083
13	11.58	7.400	1.188	11.61	4.100	1.183
14	12.40	7.300	1.288	12.41	4.000	1.283
15	13.19	7.200	1.388	13.22	3.900	1.383
16	13.97	7.100	1.488	13.99	3.800	1.483
17	14.70	7.000	1.588	14.73	3.700	1.583
18	15.43	6.900	1.688	15.44	3.600	1.683
19	16.12	6.800	1.788	16.12	3.500	1.783
20	16.77	6.700	1.888	16.79	3.400	1.883
21	17.40	6.600	1.988	17.42	3.300	1.983
22	18.01	6.500	2.088	18.02	3.200	2.083
23	18.60	6.400	2.188	18.60	3.100	2.183
24	19.15	6.300	2.288	19.15	3.000	2.283

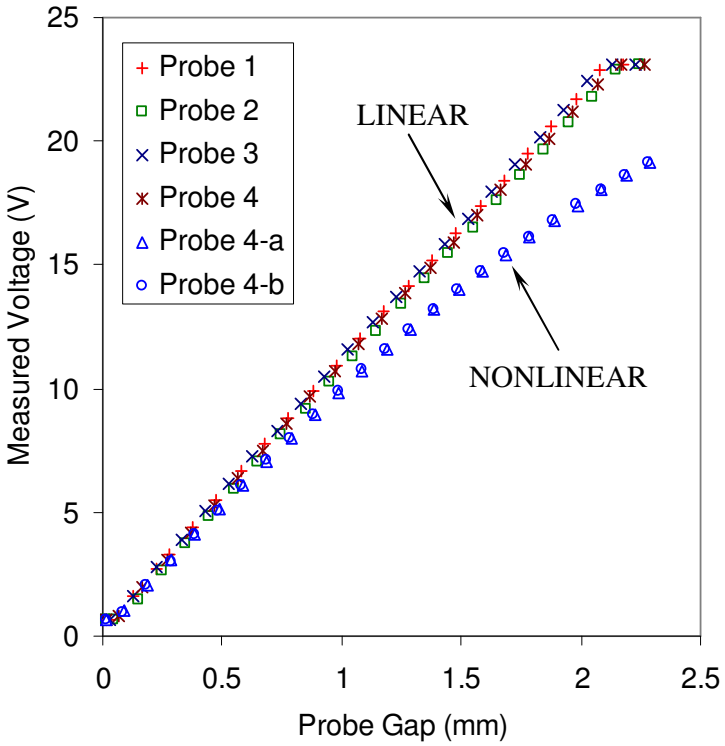

Figure A-9: **Proximity probe output voltage vs. probe gap (CAL-1).**

Table A-8: **Least-squares curve fit parameters for linear regions (CAL-1).**

Probe	Slope (V/mm)	Intercept (V)	R^2
1	10.801	0.3449	0.9999
2	10.633	0.0779	0.9999
3	10.833	0.3836	0.9999
4	10.623	0.3424	0.9999

Table A-9: **Summary of proximity probe calibration (CAL-1).**

Probe	Gain (V/mm)	Linear Range (mm)
1	10.80	0.1 – 2
2	10.63	
3	10.83	
4	10.62	

Table A-10: Calibration data for passing proximity probes (CAL-2).

*V = voltage reading; **mic** = micrometer reading (mm); **gap** = proximity probe gap (mm)*

	1			2			3			4		
	V	**mic**	**gap**	**V**	**mic**	**gap**	**V**	**mic**	**gap**	**V**	**mic**	**gap**
1	0.636	8.035	0.013	0.508	9.390	0.013	0.646	8.590	0.013	0.577	6.550	0.013
2	0.834	8.000	0.048	1.735	9.250	0.153	1.434	8.500	0.103	0.952	6.500	0.063
3	1.973	7.900	0.148	2.302	9.200	0.203	2.581	8.400	0.203	2.084	6.400	0.163
4	3.085	7.800	0.248	3.442	9.100	0.303	3.686	8.300	0.303	3.172	6.300	0.263
5	4.193	7.700	0.348	4.531	9.000	0.403	4.804	8.200	0.403	4.288	6.200	0.363
6	5.327	7.600	0.448	5.659	8.900	0.503	5.930	8.100	0.503	5.398	6.100	0.463
7	6.408	7.500	0.548	6.736	8.800	0.603	7.008	8.000	0.603	6.484	6.000	0.563
8	7.524	7.400	0.648	7.832	8.700	0.703	8.113	7.900	0.703	7.572	5.900	0.663
9	8.603	7.300	0.748	8.920	8.600	0.803	9.189	7.800	0.803	8.656	5.800	0.763
10	9.681	7.200	0.848	9.971	8.500	0.903	-	-	-	9.705	5.700	0.863

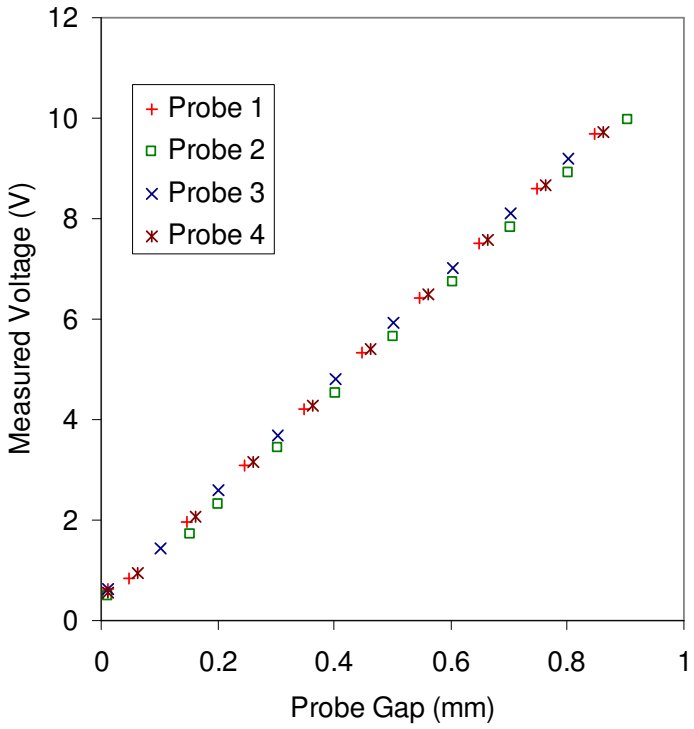

Figure A-10: Proximity probe output voltage vs. probe gap (CAL-2).

Table A-11: Least-squares curve fit parameters for linear regions (CAL-2).

Probe	Slope (V/mm)	Intercept (V)	R^2
1	11.026	0.3615	1.0000
2	10.959	0.1173	0.9999
3	11.029	0.3571	1.0000
4	10.917	0.3226	0.9999

Table A-12: Summary and comparison of proximity probe calibrations.

Probe	Gain (V/mm)		Error w.r.t. CAL-2
	CAL-2	CAL-1	
1	11.0	10.80	1.8 %
2	11.0	10.63	3.4 %
3	11.0	10.83	1.5 %
4	10.9	10.62	2.6 %

APPENDIX B

TEST BEARING PARAMETER IDENTIFICATION

This appendix contains data obtained from the measurement of pad tilting and radial stiffnesses and a detailed description for the method used to estimate the nominal clearance of a flexure pivot tilting pad bearing. The stiffness values for the pads are calculated from the measured natural frequencies that are present when the pads are excited in their various vibration modes. The stiffnesses of the upper and lower pads are different by design; however the exact values have not been previously verified. Likewise, the geometry of the bearings was specified by the design, but it was necessary to measure and verify the dimensions since the bearings had undergone extensive testing and cases of recoating.

Pad Radial and Tilting Stiffness Calculations

The previous[12] bearing design calculations used simple beam theory that predicted radial stiffnesses to be 1.0×10^7 and 0.5×10^7 N/m for the lower and upper pads, respectively, and a tilting stiffness of 34 N-m/rad for all pads. The simplified degrees of freedom of the pads are (1) radial motion, (2) tilting motion, and (3) axial pitching motion as shown in Figure B-1. Transverse pad motion is neglected due to the short length of the flexure pivot. An accelerometer is placed on the pad surface to capture the largest pad motions for the desired pad modes. As shown in Figure B-1, the

[12] "Previous" is used in this appendix to describe the work done prior to the author's current experience with the test bearings.

accelerometer is placed at the location of the pivot and the axial center of the pad (point 1) for measuring radial motion, at the location of the pivot and the axial edge of the pad (point 2) for measuring axial pitching motion, and at the circumferential leading edge of the pad along the axial center of the pad (point 3) for measuring tilting motion.

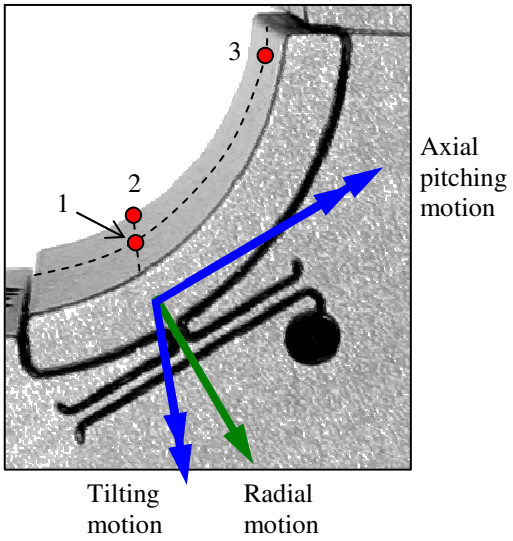

Figure B-1: **Tilting pad simplified degrees of freedom. Numbers indicate the respective locations of the accelerometer for measuring radial, axial pitching, and tilting motion natural frequencies.**

Figure B-2 shows the FFT amplitudes for the measured accelerations of the excited modes. The amplitudes are normalized by the maximum amplitude for the given mode, and the maximum peaks represent the respective measured natural frequencies. Note that the lower pads (a) have higher natural frequencies than the upper pads (b) due to the thicker construction of the compliant beam as specified by the initial design. Stiffnesses can be calculated from the measured natural frequencies if the inertia

properties are known, e.g. $\omega_n = 2\pi f_n = \sqrt{k/m}$. In the bearing model, rotor motion is considered cylindrical; thus only radial and tilting stiffness are required and axial pitching may be ignored.

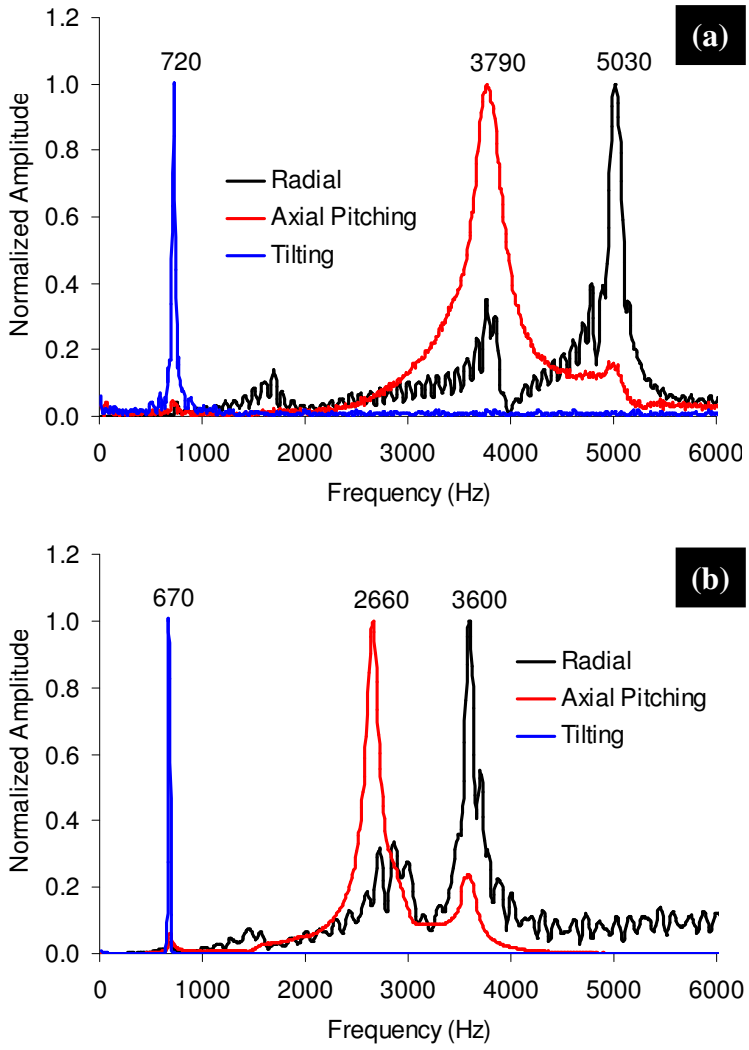

Figure B-2: **Normalized FFT amplitudes of accelerometer signals measuring exited modes of pad vibration for (a) lower and (b) upper pads. From highest to lowest frequency: Radial, axial pitching, and tilting motion.**

The pad mass and tilting moment of inertia for the test bearings were previously estimated to be 0.016 kg and 1.0×10^{-6} kg-m^2, respectively. The accelerometer used was a PCB Piezotronics Model #352C23 [42] which has a mass of 0.2 g, two orders of magnitude smaller than the pad's mass. The relatively small mass of the accelerometer allows the calculation of the radial and tilting stiffnesses to be done ignoring accelerometer mass effects. Assuming the mass and tilting moment of inertia values are accurate with 10% uncertainty and the natural frequencies shown in Figure B-2 are ±10 Hz, the radial and tilting stiffnesses may be computed from Equations (B-1) and (B-2) to give the values shown in Table B-1. Note that the measured radial stiffnesses are 60% larger than the previous design values, and the tilting stiffnesses are approximately 40% lower than estimated due to the coupled (i.e. series spring) effect of the compliant beam rotational stiffness. For simplicity, the model will consider rotational stiffness of 20 N-m/rad for all pads and radial stiffnesses of 1.5×10^7 and 0.8×10^7 N/m for lower and upper pads, respectively, which are all within the reported ranges in Table B-1.

$$k_\delta = \omega_{n,\delta}^2 m_p = 4\pi^2 f_{n,\delta}^2 m_p \tag{B-1}$$

$$k_\phi = \omega_{n,\phi}^2 i_p = 4\pi^2 f_{n,\phi}^2 i_p \tag{B-2}$$

Table B-1: Calculated/measured pad radial and tilting stiffness values.

Pads	k_δ ($\times10^7$ N/m)	k_ϕ (N-m/rad)
Lower	1.60 ± 0.17	20.5 ± 2.6
Upper	0.819 ± 0.086	17.7 ± 2.3

Estimation of Bearing Clearances

The nominal clearance is not a directly measureable quantity; rather, it is a derived quantity that is a function of the size of the rotor, the set bore of the bearing, and the preload radius of the bearing. The rotor's journal diameter and the set bore of the bearing are the only physically possible measurements that can be made with conventional machine tools (e.g. micrometer). Preload radius (recall, this is the difference between pad center and bearing center) would only be measureable with the use of a CMM, since the pad is only a small arc that cannot be measured with precision using conventional machine tools. However, preload radius is defined by the bearing design and is made by a single wire-EDM process; therefore, it can be assumed that the preload radius of the pads is accurate to within the uncertainty of the wire-EDM machine without needing to make measurements. From personal communication with Dr. Jongsoo Kim (KMC, Inc. [10], the bearing manufacturer), the accuracy of the wire-EDM machine used to make the test bearings is 0.5 micron.

In the case of the current test bearings, de-coating (via media blasting) and re-coating with Teflon® had been performed on two occasions, and the bearing set bores were measured after the re-coating (no measurements were recorded before the re-coating processes). The re-coating was performed by the original company that coated the bearings, and thickness was specified to be the same as the original coating thickness. Upon receiving the re-coated bearings, it was noticed that the bearing set bores varied in the axial direction, with the tendency to be larger in the center of the bearings than near the edges. One possible explanation for this could be an

accumulation of coating near the corners at the front/rear edges of the pads; however, this has not been quantified. Due to the axial variation of the set bores, the nominal clearance estimation includes the average set bore measured at three axial locations.

Estimation Method for Bearing Clearances

The following analysis was used to estimate the clearances of the bearings. The deviations from nominal values from the calculations are intended to reflect the level of uncertainty that exists in the true value of the clearances. The measured set bores (diagonal distances between pivots of opposing pads in a four pad bearing, see Figure B-3) are

$$A_i = \overline{A}_i \pm u_{Ai} \quad \text{and} \quad B_i = \overline{B}_i \pm u_{Bi}, \tag{B-3}$$

where $i = 1,2,3$ denotes the axial position along the bearing from which the measurements are taken (i.e. *Front, Middle, Rear*). Considering both diagonals, the minimum circle (set bore) at the i^{th} position is calculated by

$$sb_i = \min(\overline{A}_i, \overline{B}_i) \pm \left\{ \max(u_{Ai}, u_{Bi}) + \alpha \left| \overline{A}_i - \overline{B}_i \right| \right\} = \overline{sb}_i \pm u_{sb,i}. \tag{B-4}$$

Here, the uncertainty is taken as the maximum uncertainty of the two diagonals plus an additional term that is proportional to the difference in the two nominal diagonal measurements. The calculation of the uncertainty in this manner is somewhat arbitrary, but it is intended to account for the error in defining the nominal set bore circle by the

minimum diagonal when it is actually elliptical (i.e. $\overline{A}_i \neq \overline{B}_i$). The value of the proportionality constant used in the calculations was $\alpha = 0.2$. The averaged set bore for the bearing is calculated to be

$$SB = \frac{1}{3}\sum_{i=1}^{3} sb_i = \frac{1}{3}\sum_{i=1}^{3} \overline{sb}_i \pm \frac{1}{3}\sum_{i=1}^{3} u_{sb,i} = \overline{SB} \pm u_{SB}\,. \tag{B-5}$$

Estimated clearance at the pivot (or set bore clearance) considering rotor diameter measurements ($D = \overline{D} \pm u_D$) becomes

$$C_{SB} = \frac{1}{2}(SB - D) = \frac{1}{2}(\overline{SB} - \overline{D}) \pm \frac{1}{2}(u_{SB} + u_D) = \overline{C}_{SB} \pm u_{Csb}\,. \tag{B-6}$$

Finally, the nominal clearance is simply

$$C = C_{SB} + r_p = (\overline{C}_{SB} + \overline{r}_p) \pm (u_{Csb} + u_{rp}) = \overline{C} \pm u_C\,. \tag{B-7}$$

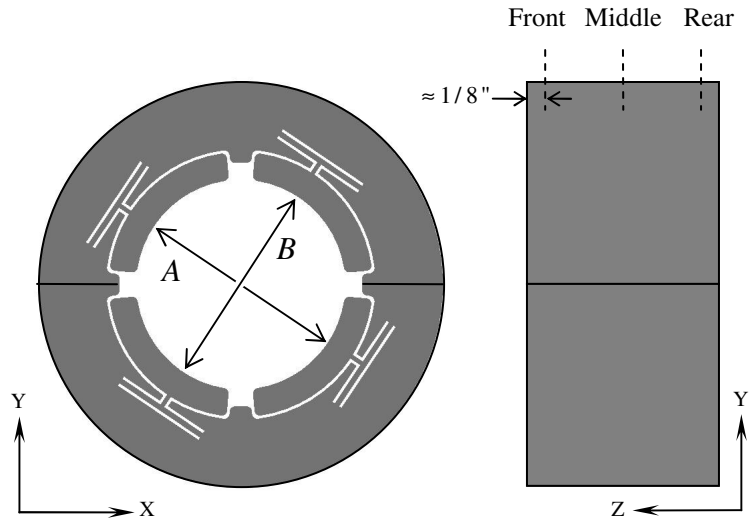

Figure B-3: Schematic for bearing set bore measurement locations.

Clearance Measurement Data and Results

The measurement data for the three bearings and the rotor, along with the results of the respective calculations from Equations (B-4)-(B-7), are shown in Table B-2. The bearing diameter measurements are made with an ID micrometer, and the variation represents 2σ from multiple measurements. The rotor diameter measurements were made with a micrometer, and the variation was taken as half of the smallest division of the readout. Preload radius variation is assumed as the manufacturing uncertainty of the wire-EDM machine. As described in the text (Chapter VI), two setups were required: Setup #1 used Bearings 1 and 3, and Setup #2 used Bearings 2 and 3. Table B-2 is organized to show the bearing combinations used in each setup and the location where the bearings were used in the test rig (i.e. “Front” or “Rear”). The data of Table B-2 are displayed graphically in Figure B-4.

Table B-2: **Bearing measurement data and nominal clearance estimation. Units are inches unless otherwise noted.**

Parameter		Bearing 1	Bearing 2	Bearing 3
$\left\{\begin{matrix} A_i \\ B_i \\ sb_i \end{matrix}\right\}$	$i=1$	1.1291 ± 0.0001 1.1290 ± 0.0003 1.1290 ± 0.0003	1.1288 ± 0.0002 1.1308 ± 0.0002 1.1288 ± 0.0006	1.1311 ± 0.0002 1.1310 ± 0.0003 1.1310 ± 0.0003
	$i=2$	1.1295 ± 0.0003 1.1297 ± 0.0003 1.1295 ± 0.0003	1.1296 ± 0.0004 1.1308 ± 0.0002 1.1296 ± 0.0006	1.1314 ± 0.0002 1.1318 ± 0.0003 1.1314 ± 0.0004
	$i=3$	1.1289 ± 0.0001 1.1290 ± 0.0002 1.1289 ± 0.0002	1.1294 ± 0.0002 1.1285 ± 0.0003 1.1285 ± 0.0005	1.1303 ± 0.0001 1.1310 ± 0.0002 1.1303 ± 0.0003
SB		1.1291 ± 0.0003 (28.679 ± 0.008 mm)	1.1290 ± 0.006 (28.677 ± 0.015 mm)	1.1309 ± 0.0003 (28.725 ± 0.008 mm)
r_p		0.00059 ± 0.00002 (15.0 ± 0.5 μm)	0.00059 ± 0.00002 (15.0 ± 0.5 μm)	0.00059 ± 0.00002 (15.0 ± 0.5 μm)
Setup #1		*Rotor "Front"*	-	*Rotor "Rear"*
Rotor dia.		1.1277 ± 0.00005 (28.644 ± 0.001 mm)	-	1.1294 ± 0.00005 (28.687 ± 0.001 mm)
C_{SB}		0.0007 ± 0.0002 (18.2 ± 4.4 μm)	-	0.0008 ± 0.0002 (19.1 ± 5.0 μm)
C		0.0013 ± 0.0002 (33.2 ± 4.9 μm)	-	0.0013 ± 0.0002 (34.1 ± 5.5 μm)
Setup #2		-	*Rotor "Front"*	*Rotor "Rear"*
Rotor dia.		-	1.1274 ± 0.00005 (28.636 ± 0.001 mm)	1.1293 ± 0.00005 (28.684 ± 0.001 mm)
C_{SB}		-	0.0008 ± 0.0003 (19.9 ± 7.9 μm)	0.0008 ± 0.0002 (20.3 ± 5.0 μm)
C		-	0.0014 ± 0.0003 (34.9 ± 8.4 μm)	0.0014 ± 0.0002 (35.3 ± 5.5 μm)

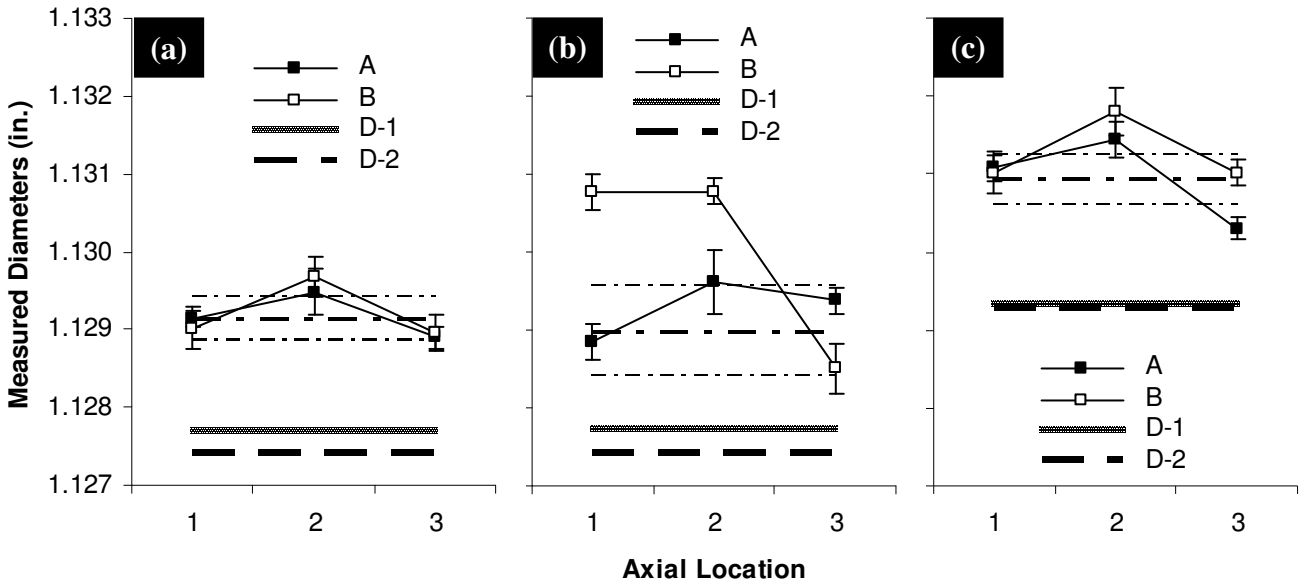

Figure B-4: **Measured set bore diameters (A and B) and rotor journal diameters for Setup #1 and Setup #2 (D-1 and D-2, respectively) plotted vs. axial position of bearings – (a) Bearing 1; (b) Bearing 2; (c) Bearing 3. Error bars on individual set bore measurements represent two standard deviations from measurements. Phantom lines represent final estimated set bore clearance (center line) and estimated deviation representing the level of uncertainty in the values (upper/lower lines).**

APPENDIX C

STUDY ON THE ACCURACY OF DIGITAL BANDPASS FILTERING USED TO DETERMINE SYNCHRONOUS RESPONSE

The study presented in this appendix details the algorithm used to filter a multi-frequency, digitally-sampled signal and reconstruct a signal that contains the desired frequency component. To test this, several artificially created signals of known frequencies, amplitudes, and phase angles are combined, and the algorithm is applied to extract a single component of this signal. Accuracy is evaluated based on the ability of the algorithm to recreate the signal, quantified by the measurement of the amplitude and phase angle.

Initial evaluation of the algorithm during development showed that performance was best for large numbers of cycles in the sample signals (i.e. high frequencies), while performance was poor when the number of cycles was insufficient to yield a steady reconstructed signal (i.e. frequency too low). Thus, the study presented focuses on the performance of the algorithm at low-to-medium frequencies. The test signals are created to represent actual test signals with 100 kHz sample rate for 0.2 second duration (20,000 samples) and synchronous frequencies from 20-1000 Hz (1.2-60 krpm). Two tests were conducted to observe the effect of varying synchronous component (1) amplitudes and (2) phase angles. The motivation for the two tests was to evaluate the performance of the algorithm as actual synchronous vibration amplitudes and phase angles are expected to change (i.e. imbalance response). Table C-1 shows the properties of the various

frequency components used to make up the combined test signals. The frequency components range from 0.5-4X, including random noise.

Table C-1: Prescribed components of combined test signal used for digital bandpass filtering algorithm performance evaluation.

Freq. × Sync.	Test 1		Test 2	
	Amp.	Phase (deg.)	Amp.	Phase (deg.)
0.5	0.5	-180	0.5	-180
1	0.2 to 1.8	-90	1.0	-5 to -355
2	1.0	-45	1.0	-45
3	1.0	-135	1.0	-135
4	0.5	-90	0.5	-90
Noise	0 to 0.25	--	0 to 0.25	--

Figure C-1 shows the amplitudes and phase angles measured from the filtered synchronous signal for Test 1, which varies synchronous component amplitude from 0.2-1.8. It is clear to see that both measured amplitudes and phase angles have good agreement for high frequencies, but there is large error for very low frequencies. The respective errors are quantified in Figure C-2. The average error in measured amplitude is less than 5% above 100 Hz and is less than 1% above 200 Hz. Average phase angle error is less than 3˚ above 80 Hz (considering error bar: 2σ). Analogous plots for Test 2 are shown in Figure C-3 and Figure C-4, and similar conclusions are made based on the errors presented. The general conclusion can be made on the performance of the bandpass filtering algorithm: The filtered synchronous signal component extracted from a mixed signal using the developed bandpass filtering algorithm may be considered

accurate for synchronous frequencies above 100 Hz (6 krpm). The expected maximum error in amplitude is less than 5%, and the expected maximum error in phase angle is less than 3˚, regardless of actual amplitude or phase angle.

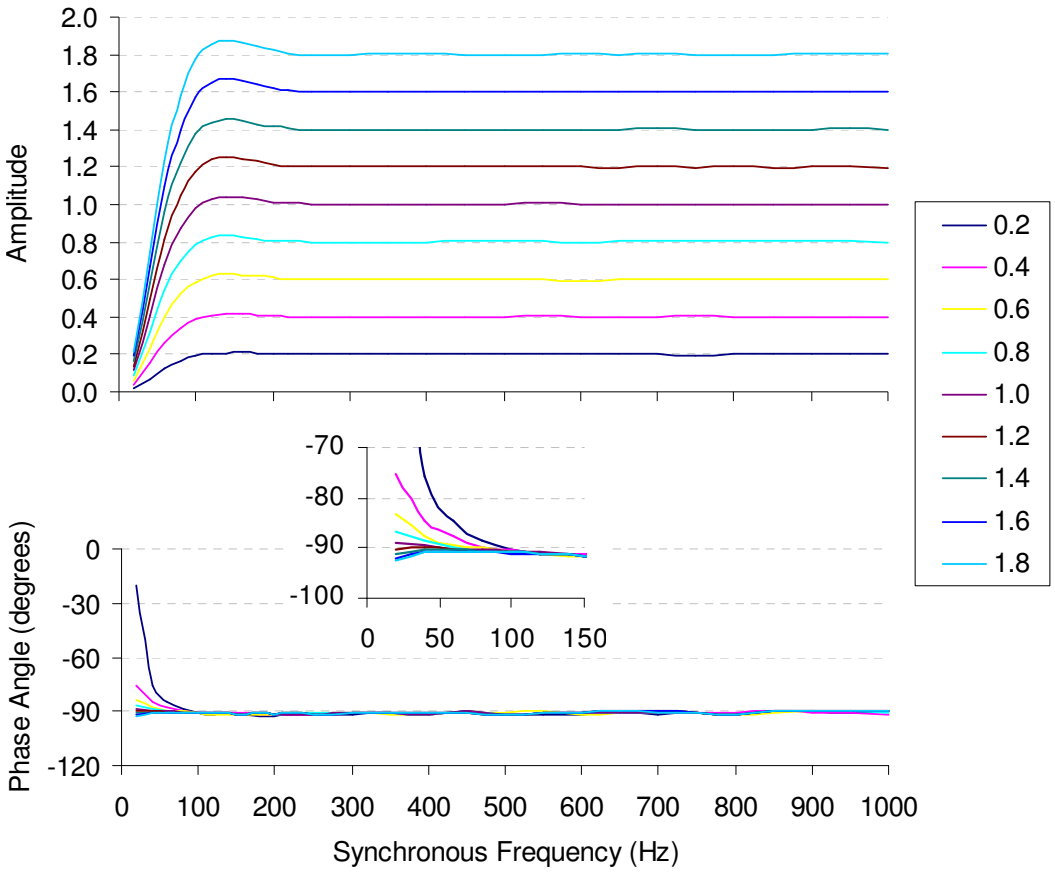

Figure C-1: **Measured amplitudes (top) and phase angles (bottom and inset) vs. synchronous frequency for multiple synchronous component amplitudes (Test 1).**

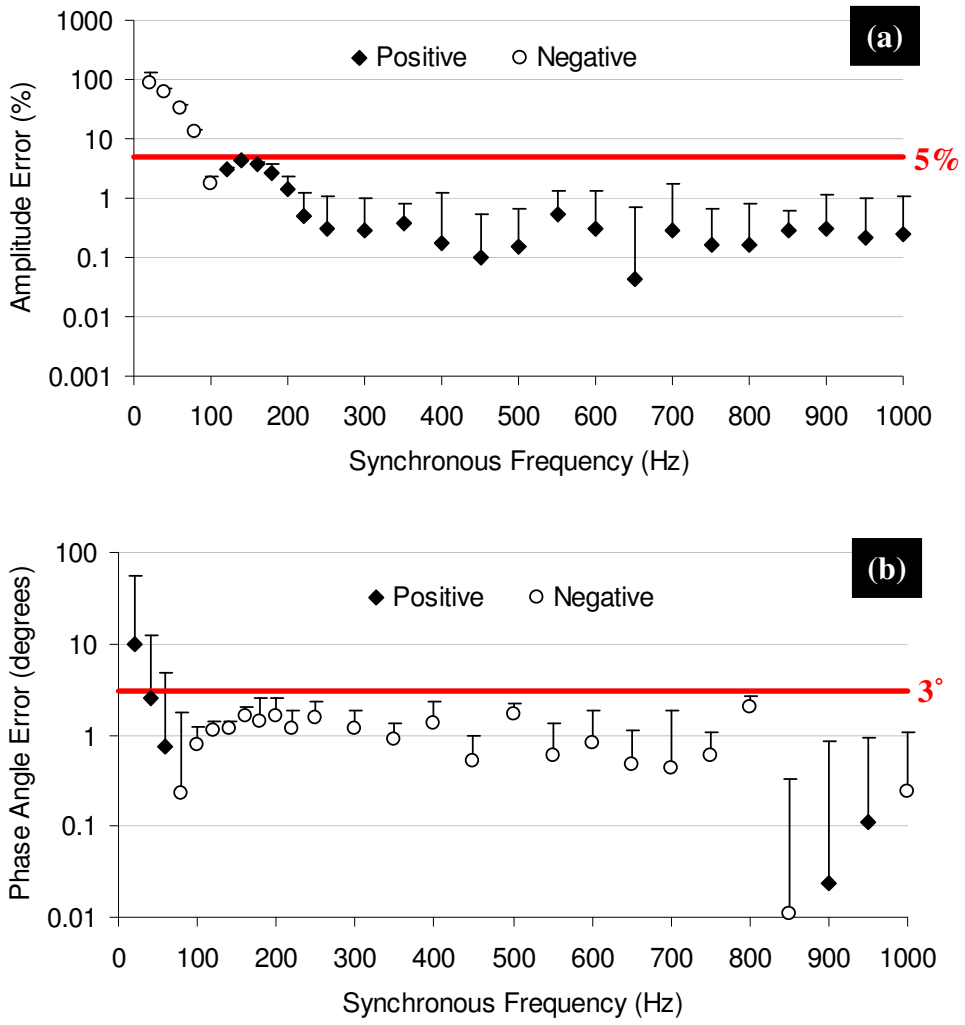

Figure C-2: **Normalized average error of amplitude and phase angle for Test 1. Percent error of amplitudes (a) is presented and compared with 5% error, and phase angle error (b) is presented and compared with a 3 degree error. Error bars in both cases represent two standard deviations of the data at a given frequency.**

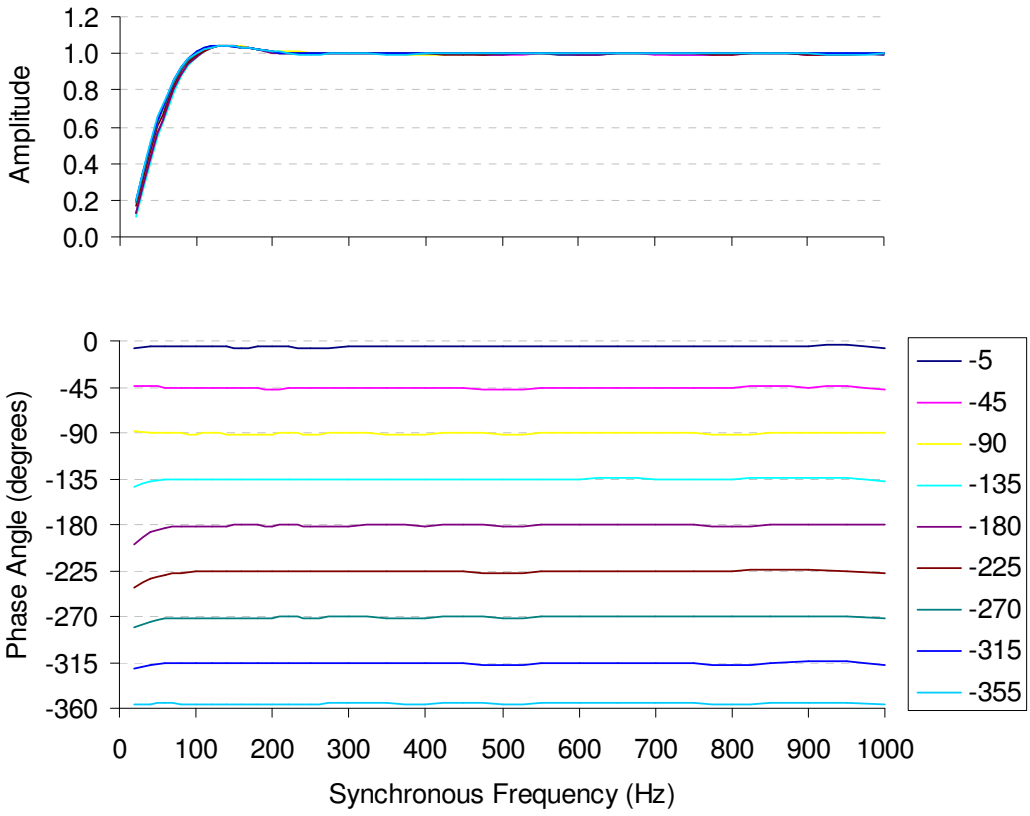

Figure C-3: **Measured amplitudes (top) and phase angles (bottom) vs. synchronous frequency for multiple synchronous component phase angles (Test 2).**

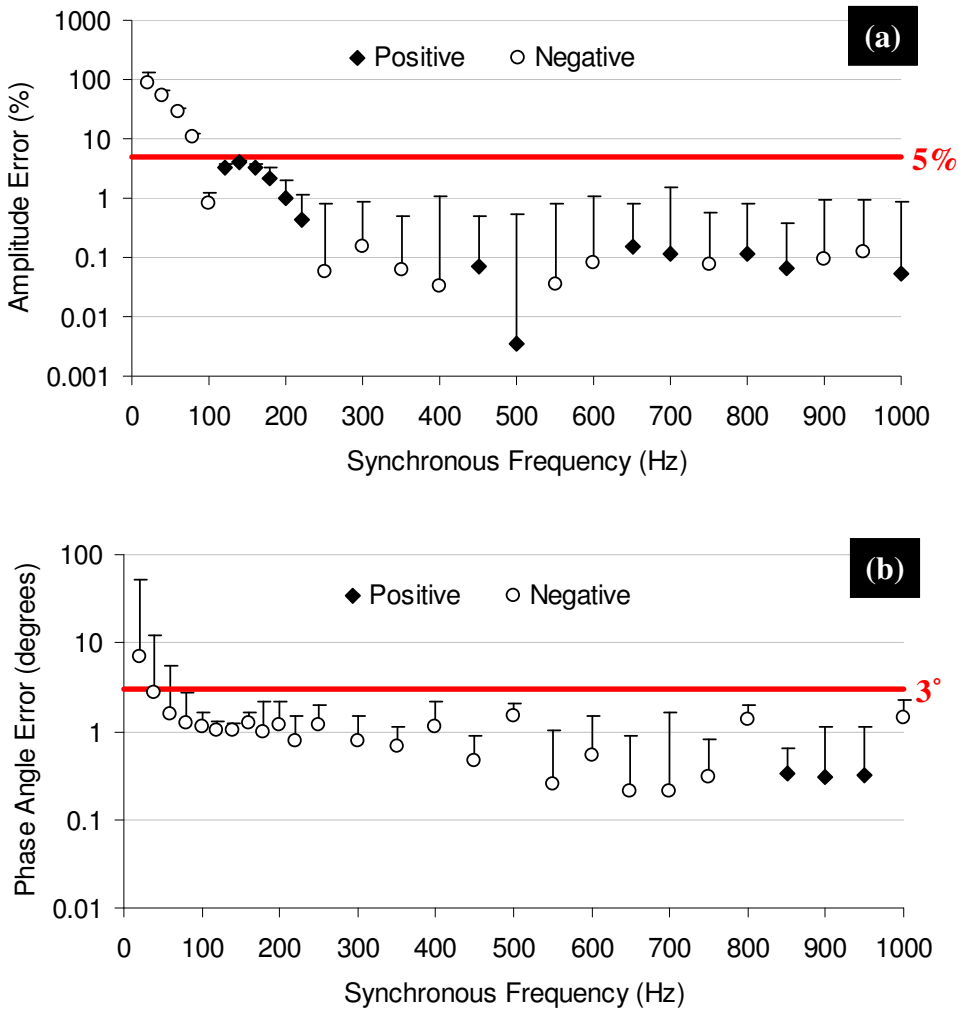

Figure C-4: **Normalized average error of amplitude and phase angle for Test 2. Percent error of amplitudes (a) is presented and compared with 5% error, and phase angle error (b) is presented and compared with a 3 degree error. Error bars in both cases represent two standard deviations of the data at a given frequency.**

APPENDIX D

CORRELATION OF DIFFERENT PHASE ANGLE DEFINITIONS

Phase angle of a measured response is considered as the lag angle from the occurrence of the keyphasor/tachometer trigger to the peak of the response (Figure D-1(a)). However, phase angle is often considered as the angle of the rotor position vector with respect to the imbalance mass (Figure D-1(b)), such that the phase angle of the rotor is $0°$ at well below the critical speed and $-180°$ at well above the critical speed. Hereon, the former definition will be denoted as the measured phase lag angle, while the latter will be referred to as the response lag angle. These two definitions may be related by

$$\phi = \psi + \zeta - \phi_{corr}\,, \tag{D-1}$$

where ϕ is the response lag angle, ψ is the measured phase lag angle from the keyphasor/tachometer trigger, and ζ is the angle of the keyphasor/tachometer sensor with respect to the orientation of the measurement sensor's positive direction. The phase angle correction is defined as:

$$\phi_{corr} = \begin{cases} 0° & \text{for} \quad \psi + \zeta < 360° \\ 360° & \text{for} \quad \psi + \zeta \geq 360° \end{cases} \tag{D-2}$$

For the test rig setup, the tachometer/keyphasor sensor is oriented in the negative X-direction, thus $\zeta_X = 180°$ and $\zeta_Y = 90°$ as shown in Figure D-2. Figure D-3 and Table D-1 illustrate how the measured phase lag angles are related to the response lag angle.

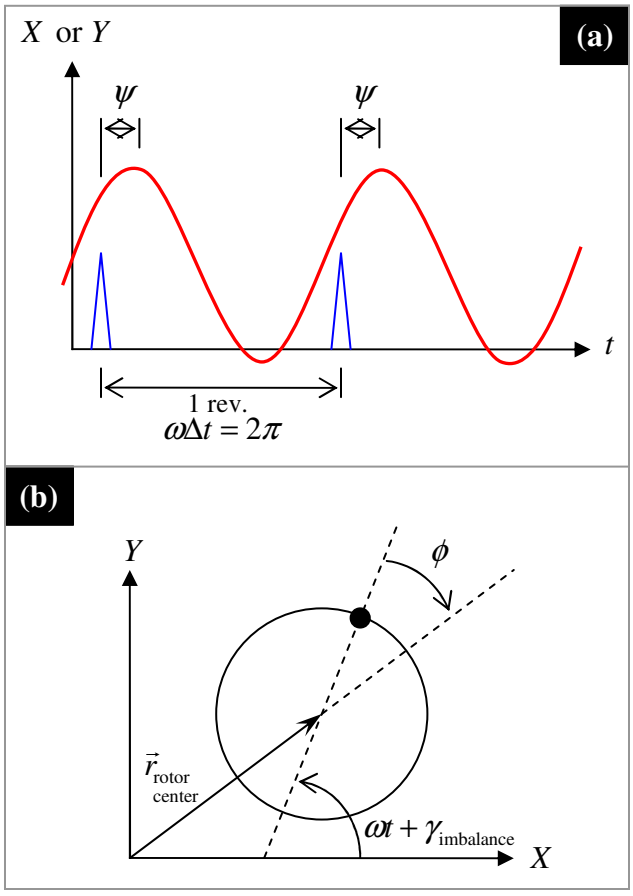

Figure D-1: **Different phase angle definitions – (a) phase lag of measured response from trigger signal; (b) phase lag of rotor position vector from location of imbalance.**

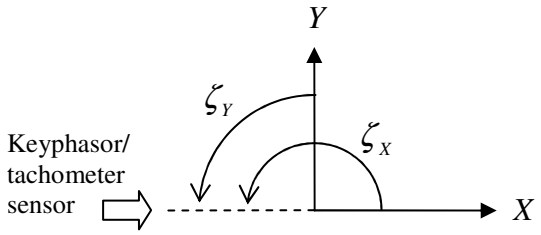

Figure D-2: **Orientation of keyphasor/tachometer sensor for relating phase angle definitions.**

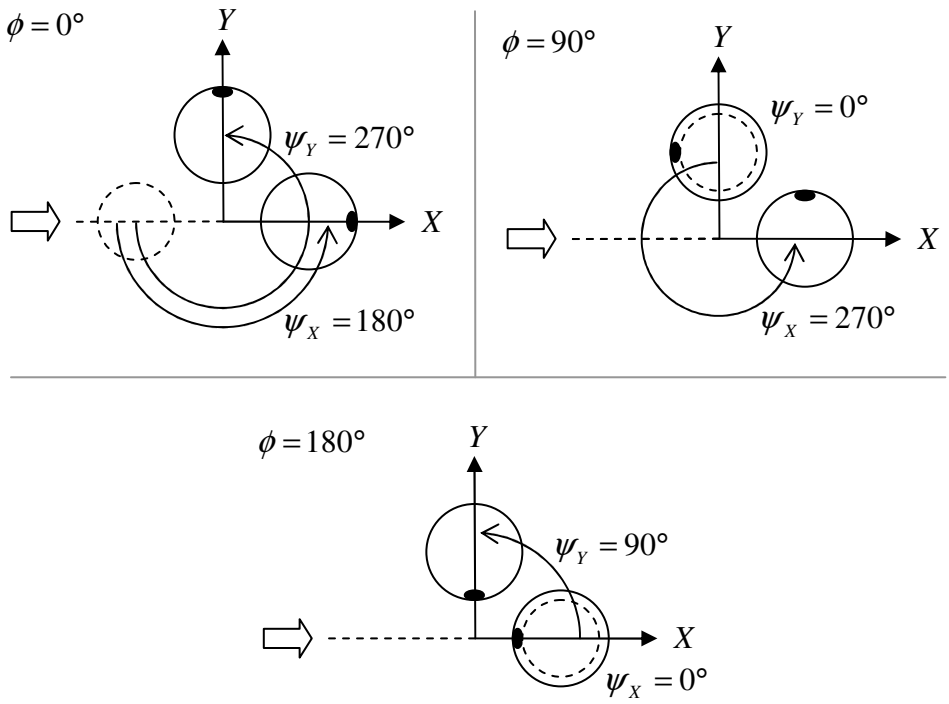

Figure D-3: **Measured phase lag angles for response lag angles of 0, 90, and 180˚. Key: solid circles represent rotor positions at peak X & Y response amplitudes, the dot on the solid circle is the location of the imbalance and keyphasor/tachometer target, and the dashed circle is rotor position when tachometer target is viewed by the keyphasor/tachometer sensor (block arrow)**

Table D-1: Response lag angles (in degrees) calculated from measured phase lag angles and Equations (D-1) and (D-2).

ϕ from Figure D-3:	0	90	180
ψ_X	180	270	0
ψ_Y	270	0	90
$\psi_X + \zeta_X$	360	450	180
$\psi_Y + \zeta_Y$	360	90	180
$\phi_{corr,X}$	360	360	0
$\phi_{corr,Y}$	360	0	0
$\psi_X + \zeta_X - \phi_{corr,X}$	0	90	180
$\psi_Y + \zeta_Y - \phi_{corr,Y}$	0	90	180

VITA

Name:	Aaron Michael Rimpel
Address:	Department of Mechanical Engineering, 3123, TAMU, College Station, Texas, USA.
Email Address:	amrimpel@yahoo.com
Education:	B.S., Mechanical Engineering, Western Michigan University, 2005 M.S., Mechanical Engineering, Texas A&M University, 2008